University of Alberta

The Axisymmetric Collapse of a Mixed Region and Internal Wave Generation in Stratified and Rotating Fluids

by

Amber Marie Holdsworth ©

A thesis submitted to the Faculty of Graduate Studies and Research in partial fulfillment of the requirements for the degree of

Doctor of Philosophy.

Department of Earth & Atmospheric Sciences

Your file Votre référence
ISBN: 978-0-494-96415-6

Our file Notre référence
ISBN: 978-0-494-96415-6

Abstract

This thesis examines the axisymmetric collapse of a mixed region in stratified fluid with and without rotation. At its depth of neutral buoyancy, the mixed region intrudes into the ambient. At the same time, the collapse excites internal waves in the underlying fluid and at the level of the propagating intrusion. The purpose of this thesis is twofold: to examine the evolution of axisymmetric intrusions in stratified fluid and to analyze the properties of downward propagating internal waves excited during the collapse. This is done through three interrelated studies.

First we present a series of axisymmetric partial-depth lock-release experiments in uniformly stratified fluid. We show that the collapse excites internal waves in the underlying fluid and measure the resulting conical wavefield using a non-intrusive analysis technique called synthetic Schlieren. We also estimate the energy transported due to the waves relative to the initial available potential energy.

The second study investigates the dynamics of the evolving intrusion for both two-layer and uniformly stratified ambient. Experiments were performed with the fluid in solid body rotation and in the absence of rotation. In the non-rotating experiments, we show that the intruding fluid is significantly influenced by interactions with internal waves launched by the return flow of the ambient into the lock. We describe how the evolution of the collapse changes under the influence of rotation and find that, for low Rossby numbers, rotation inhibits the radial propagation of the current.

The third study examines the influence of rotation on downward propagating internal waves generated by the collapse of a mixed region in uniformly stratified fluid. Experiments are used to calibrate a numerical model which

we then use to explore a wider range of parameters than the geometric constraints of the experimental apparatus would allow. In particular, we explore the influence of the aspect ratio of the lock and the Rossby number on the properties of the canonical wavefield and associated energy transport.

These results are then extrapolated to predict the energy transport of downward propagating internal waves generated by the collapse of a mixed region left in the wake of a tropical cyclone.

Acknowledgements

Without the support and love of my family and friends this dissertation would not have been possible. Thank you all for supporting me. I am especially appreciative of Michael Nelles who has been a constant source of love and encouragement throughout my graduate studies.

I am grateful to my fellow graduate students Emily, Colin, James, Jelle, Joseph, Justine, Kai, Heather, Hayley, Kate, and Lauren who shared their knowledge and made many useful suggestions. For helping with the cylindrical tank experiments, Branwen Price, a student I worked with as part of the WISEST summer program, deserves special recognition.

Thanks to all of my committee members Andrew Bush, Morris Flynn, Paul Myers, Gordon Swaters and John Wilson, and to my external examiner, Gregory Lawrence. Their attention to detail improved the overall quality of my thesis. Additional thanks go to my masters supervisor Nicholas Kevlahan who sparked my interest in fluid dynamics and introduced me to my Ph.D. supervisor.

I cannot overstate my gratitude to Bruce Sutherland, my Ph.D. advisor. His contributions to this thesis in terms of guidance and mentorship are immeasurable and his passion for fluid dynamics is inspiring.

Contents

List of Tables

List of Figures

Chapter 1

Introduction

1.1 Motivation

1.1.1 Ocean Mixing

The ocean is stably stratified consisting of a surface mixed region, a strongly stratified pycnocline layer and a weakly stratified abyss. Incoming solar radiation is absorbed by the surface mixed region and wind driven mixing redistributes the heat throughout this layer. The depth varies (50 200 m) as a result of heating and cooling at the ocean surface and turbulent mixing with the underlying fluid. In the layer below, the temperature decreases rapidly with increasing depth as it transitions from the relatively warm near-surface water to the cold abyss, which is why this pycnocline region is known as the thermocline. The high specific heat capacity of water makes the ocean the largest heat reservoir on the planet. Yet most ocean water is contained within abyssal waters that are maintained by the influx of cold dense currents formed at high-latitudes. Heat exchanges between the abyss and the ocean surface occur through diapycnal mixing of the pycnocline layer. It follows that an accurate parameterization of ocean mixing, a key aspect of climate modelling, requires an understanding of how the cool, dense water flowing into the deep abyss returns to the surface.

The meridional overturning circulation (MOC) is the process by which cold dense water formed in the Northern Atlantic and Antarctic oceans is redistributed throughout the ocean interior up-welling at mid-latitudes. Sandström argued that the relative pressures at locations of heating and cooling govern a buoyancy driven circulation and that, furthermore, a steady circulation can be maintained against the retarding effects of friction only if the ocean is heated at a higher pressure than it is cooled (Sandström, 1908, 1916;

Wunsch & Ferrari, 2004). While this type of buoyancy forcing takes place in the upper ocean, since it is heated to the depth of the photic zone ($\simeq 200\,\mathrm{m}$) at mid-latitudes and cooled at the surface near the poles. Sandstrom's effect implies homogeneous density in the abyssal ocean. In other words, a circulation manifests between the thermocline layer at mid-latitudes and the surface at higher latitudes with no circulation evident in the abyss. However, the ocean abyss is weakly stratified and since buoyancy forcing alone cannot explain the observed density profile, sources of mechanical energy are sought to explain the dissimilitude (Ferrari & Wunsch, 2009).

Assuming a global upwelling throughout the ocean abyss, an average vertical eddy diffusivity of $10^{-4}\,\mathrm{m}^2/\mathrm{s}$ is required to maintain the observed structure, but observations indicate a uniform background diffusivity on the order of $10^{-5}\,\mathrm{m}^2/\mathrm{s}$ (Munk & Wunsch, 1998). Highly localized mixing is a plausible explanation for the large discrepancy.

Dye release experiments indicate the presence of highly localized turbulence in the ocean, even above the thermocline layer (Grant *et al.*, 1968; Woods & Wiley, 1972). These observations are corroborated by microstructure measurements taken during the Coastal Mixing and Optics Experiment (CMO) (Oakey & Greenan, 2004; Sundermeyer *et al.*, 2005) and support the conjecture that highly localized mixing is a major contributor to the upwelling branch of the meridional overturning circulation, but the sources of mechanical energy that contribute to localized mixing, especially in the ocean abyss, remain unquantified.

Stratified fluids support internal waves which move due to buoyancy forces, transporting both energy and momentum. When these waves are confined to an interface, as is the case in a two-layer fluid, they are called interfacial waves. More complex stratifications allow for internal waves that propagate vertically as well as horizontally.

Where these waves break they form turbulent patches that cause irreversible diapycnal mixing in the stratified fluid. If a turbulent mixing event occurs over the vertical extent of the pycnocline, the collapse of the mixed patch can lead to the formation of an intrusion and an associated interfacial wave that propagate along the pycnocline (Maderich *et al.*, 2001). This thesis will show that the collapse can also act as a mechanism for the generation of downward propagating internal waves which have the potential for causing diapycnal mixing in the abyss. Wave breaking generates turbulence which mixes a region of fluid and since the collapse of the mixed region, in turn, generates

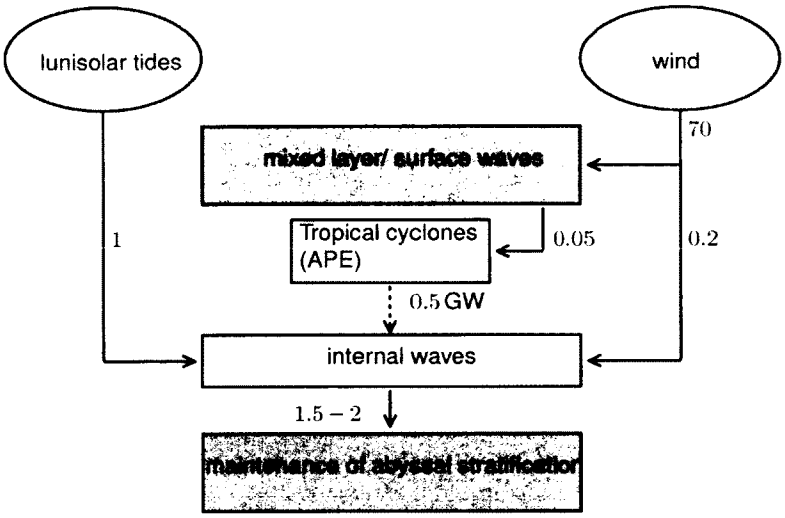

Figure 1.1: Energy pathways, sources (circles) and reservoir (shaded rectangles). Units are in TW if not stated explicitly. The dotted line represents the amount of power input to the internal wave field from the collapse of a mixed region resulting from a moving hurricane discussed in Chapter 4.

internal waves, internal waves facilitate the cascade energy from large to small scales in the ocean interior.

Turbulent patches generated by breaking of the ocean internal wave field are primarily responsible for the estimated $1.5 - 2\,\mathrm{TW}$ required to maintain the observed stratification (Ferrari & Wunsch, 2009). Internal wave breaking tends to occur near boundaries, in regions of rough topography such as the continental shelf, or due to wave-wave interactions in the ocean interior, but the mechanisms by which internal waves are generated have not yet been completely catalogued.

Munk & Wunsch (1998) constructed an "impressionistic" ocean energy budget which outlined the major energy reservoirs, their sources and the interchanges between them. This order of magnitude estimate of the energy budget has been debated and corrected yet it remains incomplete (Ferrari & Wunsch, 2009, 2010). The baroclinic conversion of tidal energy into the internal wave field was estimated to account for as much as $1\,\mathrm{TW}$, with another $0.2\,\mathrm{TW}$ attributed to the direct forcing of the wind (Ferrari & Wunsch, 2009, 2010).

Figure 1.1 summarizes these contributions in a simplified and modified version of their energy budget focusing upon the contribution of internal waves. The incongruency between the power required to maintain the stable stratification against global deep water formation and the amount of energy input to the internal wave-field that is available for diapycnal mixing are ascribed to the mechanical generation of internal waves through interactions with bottom topography or to local instabilities. But the pathway that the energy takes from the sources, shown as circles on the diagram, to the reservoir, shown by shaded squares, is not well understood. This thesis investigates a hitherto unexplored pathway through which energy from the surface wind field is transported to the abyssal ocean internal wave field; through the collapse of a mixed region generated by a large-scale ocean mixing event resulting, for example, from a tropical cyclone.

Tropical cyclones are transient events that occur sporadically, but recent studies show they may be an important source of energetics for ocean mixing (Boos *et al.*, 2003; Sriver & Huber, 2007; Emanuel, 2001) and nutrient transport (Lin *et al.*, 2003). Tropical storms can mix the ocean beneath them to depths of several 100 metres (Gregg, 1976) leaving cold water wakes (Price, 1981) that return to near pre-storm conditions over a period lasting weeks to months through the process of restratification (Emanuel, 2001).

Hurricanes typically lower the sea surface temperature (SST) (D'Asaro *et al.*, 2011) by 1–3 °C while slow moving typhoons have been observed to lower the SST by up to 9 °C. Emanuel (2001) demonstrated that a substantial amount of the ocean heating required to drive the poleward heat flux may be accounted for by localized mixing due to tropical cyclones. These storms are responsible for as much as 15% of peak ocean heat transport (Sriver & Huber, 2007) and are one plausible mechanism for generating the diapycnal mixing necessary to drive the Meridional Overturning Circulation (Boos *et al.*, 2003).

Recent studies have attempted to quantify the power that is imparted to surface waves, near-inertial interfacial waves and geostrophic currents by the passage of a hurricane (Nilsson, 1995). Liu *et al.* (2008) estimated that, on average, tropical cyclones cause an increase of potential energy of about 0.05 TW (this value was added to the budget in Figure 1.1). These studies focused on the dynamics of the upper-ocean response to a hurricane. Little is known about the physical collapse of a mixed region as a mechanism for the excitation of internal waves. These dynamics will be explored in this thesis through a combination of laboratory experiments and numerical simulations.

1.2 Gravity Currents and Intrusions

The study of density driven flows in laboratory experiments was motivated by environmental flows in the atmosphere and ocean including sea breezes, thunderstorm outflows, river outflows, lava, estuarine and pollution flows as well as numerous industrial phenomena.

Driven by horizontal differences in pressure, a gravity current forms when fluid of uniform density flows horizontally into fluid of a different density or into density stratified fluid. In the latter case, the current can propagate within the interior of the fluid and is referred to as an intrusive gravity current or, simply, an intrusion.

Most studies of gravity currents and intrusions were performed in rectilinear geometries in which the current propagated along the length of a long rectangular tank. There have been relatively few studies in axisymmetric geometries in which the current spread radially from a cylindrical lock. Of those experiments, very few examined partial-depth lock release and even fewer involved rotation. This section will review the relevant theory and experiments and show how the work presented in subsequent chapters bridges appreciable gaps in the literature.

1.2.1 Rectilinear Geometry

Experimental studies of gravity currents were first reported by Schmidt (1911) who examined cold currents flowing into relatively warm ambient fluid. He found that the shape of the current head changed with temperature so that mixing above the current head increased with increasing Reynolds number (as reported by Simpson (1972)). Keulegan (1957) performed a series of lock-release experiments in which salty lock-fluid was released in fresh-water ambient exploring the speed and shape of the propagating current. Benjamin (1968) theoretically considered the more general case in which fluid of one density, ρ_l, was separated by a gate from ambient fluid of lower density, ρ_a. When the lock was extracted the lock-fluid flowed as a gravity current into the ambient along the rigid bottom boundary. Meanwhile the ambient fluid flowed over the gravity current into the lock replenishing the lock-fluid. Shortly after release, the front of the current was observed to travel at a near-constant speed. During the so-called "slumping phase" the front speed was predicted

to be

$$U = \mathrm{Fr}_b \sqrt{g' H} \tag{1.1}$$

where the Froude number Fr_b is the ratio of inertia to gravitational forces, H is the total depth of the fluid and $g' = g(\rho_l - \rho_a)/\rho_a$ is the reduced gravity. According to Benjamin (1968)

$$\mathrm{Fr}_b(\tilde{h}) = \sqrt{\frac{\tilde{h}(1-\tilde{h})(2-\tilde{h})}{(1+\tilde{h})}} \tag{1.2}$$

where $\tilde{h} = h/H$, the relative depth of the current head. Additionally, by applying conservation of energy he found that a uniform gravity current progresses steadily only if it occupies half the space originally occupied by the lighter fluid ($h = H/2$). In this case, the Froude number is given by $\mathrm{Fr}_b = \mathrm{Fr}_0 = 1/2$.

Most theoretical and experimental studies of gravity currents have assumed a constant volume is released from a lock in a rectilinear geometry (Simpson & Britter, 1979; Huppert & Simpson, 1980; Maxworthy *et al.*, 2002). In this case, gravity currents are known to propagate at near-constant speed, as predicted by Benjamin (1968) for 6–10 lock lengths .

Huppert & Simpson (1980) examined the evolution after the slumping phase. Using a 'box model', which assumed that the current evolved as a series of equal-area rectangles, they described the collapse in terms of a Froude number as it depended on the fractional depth of the current head relative to the total depth of the ambient. After the slumping phase, in what is called the self-similar regime, the speed was predicted to decrease as the head-height of the current decreased. Using shallow water theory, the self-similar regime was found to begin abruptly when a wave (a "rear bore") launched by the return flow into the lock caught up with the intrusion head (Rottman & Simpson, 1983).

Theoretical predictions of the initial speed of an intrusion in a stratified ambient were established for both two-layer (Cheong, Kuenen & Linden, 2006; Flynn & Linden, 2006) and uniformly stratified (Bolster *et al.*, 2008) fluids. In linearly stratified fluid, bottom propagating gravity currents were first studied in experiments by Maxworthy *et al.* (2002) who characterized the speed of the current in terms of the buoyancy frequency N, which is a measure of the strength of the stratification, and the total depth of the fluid H so that

$$U = \mathrm{Fr} N H. \tag{1.3}$$

Here again, Fr is the Froude number. They found that Fr $\simeq 0.266$ when the density of the current was equal to the density at the bottom of the ambient. When the speed of the current was less than the speed of a linear mode-1 wave (Fr < 0.3) a rhythmic coupling between the current and the internal waves was observed. The interaction with successive wave fronts caused the current to accelerate and decelerate. For faster currents, the wave and current propagated out for $\simeq$ 16 lock-lengths before the wave separated from the current and moved ahead of it.

Experiments have shown that the evolution of rectilinear intrusions in stratified ambient is significantly altered by generating and interacting with internal waves (Wu, 1969; Amen & Maxworthy, 1980; Holyer & Huppert, 1980; Sutherland *et al.*, 2004*a*; Munroe *et al.*, 2009; Tan *et al.*, 2011). Wu (1969) performed the first experiments investigating internal waves generated by the collapse of a localized patch of fluid. The cylindrical lock was situated at mid-depth at one side of a rectangular tank filled with uniformly stratified fluid. He was able to observe the generation of internal waves through the displacement of dyed isopycnal surfaces and inferred that the initial collapse was entirely responsible for the generation of internal waves. He also noted that the peak spectral energy density was associated with waves having frequency around 0.8 of the buoyancy frequency.

If the density of the intrusion is the average density of the uniformly stratified ambient, then the intrusion is called symmetric. For symmetric intrusions propagating in a two-layer fluid, the intrusion density is the average ambient density and the upper and lower layer depths of the ambient are equal. In a two-layer ambient, symmetric intrusions were observed to propagate at near-constant speed well beyond 10 lock lengths (Sutherland *et al.*, 2004*b*; Sutherland & Nault, 2007) without entering the self-similar regime. They found that the intrusion excited a mode-2 solitary wave that depressed and elevated the interface surrounding the intrusion head. This wave carried the intrusion forward despite a continuous decrease in the intrusion head height.

An intrusion is said to be asymmetric if its density differs from the density of the ambient fluid. In a two-layer ambient, Sutherland *et al.* (2004*b*) found that large amplitude interfacial waves were excited. Munroe *et al.* (2009) found that in uniformly stratified fluid, asymmetric intrusions were entirely halted when mode 1 internal waves, which were launched by the return-flow that reflected off the lock end of the tank, caught up to the head of the intrusion.

Atmospheric and oceanic gravity currents have head heights much smaller

than the ambient depth, and so are better represented by partial-depth lock release experiments. However, only a handful of such experimental studies exist.

A tank filled with a homogeneous fluid overlying a linearly stratified bottom layer serves as a simple model of the ocean and thermocline or the troposphere underlying the stratosphere. This set-up has been used to study partial-depth intrusions and the waves they generate (Flynn & Sutherland, 2004; Sutherland *et al.*, 2004*a*). Downward propagating internal waves excited by the interaction of the intrusion with ambient were measured using a non-intrusive analysis technique called synthetic Schlieren (Sutherland *et al.*, 1999). The intrusion advanced at constant speed exhibiting no resonant interactions with internal waves. By comparing experiments with simulations, which had a significantly deeper lower boundary, they found that long wavelength disturbances were excited by the return flow. These filtered downward propagating waves while also transporting energy over long distances (Sutherland *et al.*, 2004*a*).

Sutherland *et al.* (2007) examined the collapse of a mixed region into uniformly stratified ambient. In this case they found the intrusion excited vertically propagating waves. They were able to measure wave characteristics and their associated energy transport using synthetic Schlieren (Sutherland *et al.*, 1999). The experiments presented in Chapter 2 will explore how these wave characteristics change in an axisymmetric geometry.

1.2.2 Axisymmetric Geometry

There have been relatively few studies examining the speed of radially spreading gravity currents released from a cylinder. Geometry and mass conservation dictates that the head height must decrease as the radius increases. This implies that the front should decelerate shortly after release.

In their study of bottom propagating gravity currents released from a cylindrical lock into a uniform density ambient, Huppert & Simpson (1980) used a box model to predict that the front position of axisymmetric gravity currents changes with time t proportionally to $t^{1/2}$ during the self-similar regime. In experiments this regime was observed to establish itself after propagating approximately 3 lock-radii.

In contrast to Huppert & Simpson (1980), McMillan & Sutherland (2010) used a combination of laboratory experiments and numerical modelling to show that vertically symmetric axisymmetric intrusions in two-layer ambient

propagated at constant speed beyond 8 lock radii even though their head height decreased with radial distance. Numerical simulations confirmed that the non-zero thickness of the interface resulted in a mode-2 solitary wave that surrounded the intrusion head and carried it radially outwards. This caused the current to move at near-constant speed even as the wave amplitude decreased with radial distance as $r^{-1/2}$.

In cylindrical lock release experiments examining asymmetric intrusions in two-layer fluids, a mode-1 internal wave was excited by the return flow into the lock which caught up with the intrusion head and inhibited, or sometimes halted, its forward advance (Holdsworth *et al.*, 2012*a*). The experimental results are presented in Chapter 3.

Most laboratory experiments investigating intrusions in an uniformly stratified fluid have examined intrusions resulting from continuous forcing of a turbulent patch (Manins, 1976; Maxworthy & Monismith, 1988; Silva & Fernando, 1998). The constant volume lock-release experiments presented in Chapter 3 examine the collapse of the mixed patch after turbulence has dissipated. Holdsworth *et al.* (2012*a*) found that asymmetric intrusions in uniformly stratified fluid behaved similarly to two-layer currents; halting due to interactions with mode-1 internal waves generated by the asymmetric return flow in to the lock. In the symmetric case a mode-2 wave was excited and caught up with the intrusion head. Because the intrusion was moving slowly relative to the two-layer case, instead of carrying the intrusion forward it inhibited or even halted the intrusion's radial advance.

1.2.3 Rotational Effects

The rotation of the Earth can influence fluid motion for flows that have large horizontal scales and evolve over long time-scales. Through the Coriolis effect, rotation changes the direction of flow by deflecting fluid to the right in the northern hemisphere and to the left in the southern hemisphere. Localized mixing increases the systems' potential energy (PE) by creating a density perturbation which undergoes a gravitational adjustment forming into a current and releasing kinetic energy (KE) in the form of interfacial waves.

The horizontal scale above which rotation is non-negligible is given by the (internal) Rossby deformation radius,

$$L_D = U/f. \tag{1.4}$$

Here U is the characteristic speed, which for intrusions is related to buoyancy through expressions like equation (1.1). If the collapse of the mixed patch takes place over scales on the order of L_D then rotation dominates and inhibits the forward motion of the current. The Rossby number $\mathrm{Ro} = U/fL$ describes the relative importance of inertial and Coriolis terms where U is the characteristic velocity, L is the length scale over which the velocity varies and f is the Coriolis parameter. For $\mathrm{Ro} \ll 1$, the steady state, known as geostrophic balance, is reached when the outward radial pressure gradient force is balanced by the Coriolis force.

A combination of laboratory experiments and numerical modelling have been used to investigate the axisymmetric spreading of rotating bottom-propagating gravity currents in a uniform density ambient (Ungarish & Huppert, 1998; Hallworth *et al.*, 2001; Ungarish & Zemach, 2003). In experiments with Ro of order unity, Hallworth, Huppert & Ungarish (2001) found that rotation reduced the maximal distance, $R_{\max}$, to which the current propagated. They determined $R_{\max}$ depended on L_D so that the ratio of $R_{\max}/L_D$ ranged from $3.7L_D$ - $5.1L_D$ for Rossby numbers between 0.6 and 1.5. Once $R_{\max}$ was reached the flow reversed direction and the majority of the lock-fluid returned inward, accumulating near the tank centre. This mass of fluid then exhibited a second outward pulse which propagated out radially and often exceeded $R_{\max}$ by a short distance. The frequency of the pulsations, ω_p, increased with the rotation rate of the fluid, Ω, according to $\omega_p = 2.10\Omega$. This result was independent of the initial conditions indicating that the pulsations were a result of inertial oscillations.

Ungarish & Huppert (2004) used a one-layer shallow water approximation to analyze axisymmetric gravity currents at the base of a stratified ambient in the presence of a uniform background rotation. Gravity currents propagating beneath uniformly stratified ambient have a lower initial speed and shorter $R_{\max}$ relative to the homogeneous case. They found good agreement between their approximation and the initial speed of the current, but admitted that the model breaks down over larger time scales because it does not incorporate the influence of internal waves. The intrusions formed into lens-shaped vortices in the steady state. These studies of axisymmetric gravity currents in solid body rotation have focused on cases where $\mathrm{Ro} > 1$ because if the Rossby deformation radius, L_D, is less than the initial radius of the patch, R, then only a small deviation from geostrophic balance is possible.

Lelong & Sundermeyer (2005) numerically studied the gravitational ad-

justment of an isolated lens in a continuously stratified ambient and its dependence on the Rossby number $\mathrm{Ro} = Nh/fR$, where h is the initial height of the anomaly. The adjustment of the patch evolves in two phases consisting of a slumping phase, during which internal waves are emitted, followed by a geostrophically balanced phase. High frequency waves were emitted first, at the start of the slumping phase, followed by low frequency waves released just before entering the balanced phase. They found that balanced vortical motions were most efficiently generated when $\mathrm{Ro} = 1$, rotation dominated so that very little kinetic energy was converted to potential energy when $\mathrm{Ro} < 1$, and much of the initial potential energy was converted to kinetic energy during the initial adjustment resulting in a weak vortex when $\mathrm{Ro} > 1$.

Lelong & Sundermeyer (2005) varied Ro by changing the horizontal length scale of the patch. Chapter 4 will show that changing the aspect ratio of the patch can change the dynamics of the slumping phase, thereby altering the generated waves even in the absence of rotation. The dynamics of the evolving patch during the slumping phase are found to be dictated both by the aspect ratio of the mixed region and by the associated Rossby number.

The geostrophic adjustment of an isolated axisymmetric lens was studied by Stuart *et al.* (2011) using a combination of experiments and numerical models. They focused on the dependence of the velocity and length-scale of the adjustment on the Burger number, $\mathrm{Bu} = \mathrm{Ro}^2$. Finding that the velocities scaled with the reduced gravity wave speed and the adjustment distance scaled with the Rossby deformation radius of the patch, Lelong & Sundermeyer (2005) characterized properties of the lens and its relationship with initial conditions. In the experiments presented in Chapter 3, Holdsworth *et al.* (2012*a*) focus, instead, on the speed of the intrusion and its interaction with interfacial waves immediately following its release from the lock, for the most part in experiments with Rossby number order unity and higher.

1.3 Thesis Overview

Table 1.1 summarizes the experimental contributions to this problem discussed in the previous sections. Prior to the work presented here (Holdsworth *et al.*, 2010, 2012*a*), little was known about the evolution of intrusions in an axisymmetric geometry beyond vertically symmetric cases. For the first time, downward propagating internal waves generated by the collapse of a mixed region in an axisymmetric geometry were measured and their associated en-

	Two-Layer	Uniform
non-rotating	Holdsworth *et al.* (2012*a*)(asymm.) Holdsworth *et al.* (2010)(igw) McMillan & Sutherland (2010)(symm.) Sutherland & Nault (2007)	Holdsworth *et al.* (2012*a*) Sutherland & Nault (2007)
rotating	Holdsworth *et al.* (2012*a*)	Holdsworth *et al.* (2012*a*) Holdsworth & Sutherland ((in preparation for submission to Phys. Fluids)

Table 1.1: This table summarizes the available literature examining axisymmetric intrusions and internal wave generation in stratified fluid with and without rotation in laboratory experiments.

ergy transport estimated for both non-rotating (Holdsworth *et al.*, 2010) and rotating cases (Holdsworth & Sutherland, (in preparation for submission to Phys. Fluids).

Laboratory experiments were performed with three goals in mind: examine the speed and evolution of the intrusion, investigate interactions between the propagating intrusion and the generated waves, and explore how the characteristics of the waves depend on the initial conditions.

Chapter 2 presents the first examination of internal waves generated by the axisymmetric collapse of a mixed region in a non-rotating uniformly stratified ambient (Holdsworth *et al.*, 2010). This is an idealized case which neglects the complicated dynamics of surface winds, turbulence and rotation. The study focuses on those high frequency waves which propagate over time scales short compared with the Earth's rotational period. With respect to storm-generated waves, the study is relevant to waves generated during the initial collapse phase.

Chapter 3 reports upon lock-release laboratory experiments that examine the collapse of a localized cylindrical mixed patch of fluid in both two-layer and uniformly stratified ambients (Holdsworth *et al.*, 2012*a*) the focus here is upon intrusions and not the internal waves they generate. The experiments were performed with and without rotation in a cylindrical tank. Unlike bottom propagating gravity currents, non-rotating intrusions typically propagated many lock radii at constant speed. In vertically asymmetric cases they stopped abruptly due to interactions with internal waves. Rotation had no impact on the intrusion's initial speed. However, it limited the maximum distance propagated by the intrusion and caused the patch to expand and contract as it approached equilibrium.

To explore the effect of rotation upon wave generation by intrusions, the non-rotating experiments of Holdsworth *et al.* (2010) were repeated on a rotating table. These results are presented in Chapter 4. Two distinct wave-packets were generated during the initial collapse. The first was generated immediately upon release and had a peak frequency near the buoyancy frequency; the second emerged after at least one buoyancy period with a peak frequency near the inertial frequency. The energy associated with the wave-packets was found to be much higher for $\mathrm{Ro} < 1$ when the undulation of the patch was sustained in the process of geostrophic adjustment.

The numerical model of the fully nonlinear equation in axisymmetric geometry allowed for the exploration of circumstances beyond the reach of the laboratory experiments. After testing its validity by comparing it with corresponding lab experiments, simulations were performed for mixed region collapse at much larger scales. From these results, the model is used to make a crude estimate of the amount of energy imparted to downward propagating internal waves which have the potential for diapycnal mixing in the ocean abyss.

Chapter 2

The Axisymmetric Collapse of a Mixed Patch and Internal Wave Generation in Uniformly Stratified Fluid

2.1 Introduction

This chapter presents the first examination of the axisymmetric collapse of a mixed region in a uniformly stratified ambient as a mechanism for the generation of downward propagating waves using a series of laboratory experiments. The extension to axisymmetric geometries is non-trivial because as the intrusion advances radially its height must decrease in vertical extent as a result of mass conservation. A visualization technique known as Synthetic Schlieren was applied to determine the frequency, radial wavenumber, and vertical displacement amplitude of the internal waves. These results were then used to estimate the amount of energy they transported to greater depth.

Details of the experimental set-up and image processing are described in Sec. 2.2. The methods used to compute wave frequency, radial wavenumber and vertical displacement amplitude are explained in Sec. 2.3 and the fraction of the system's available potential energy extracted by the waves is given in Sec. 2.4. In Sec. 2.5 the results are scaled so as to predict wave energetics on oceanic scales.

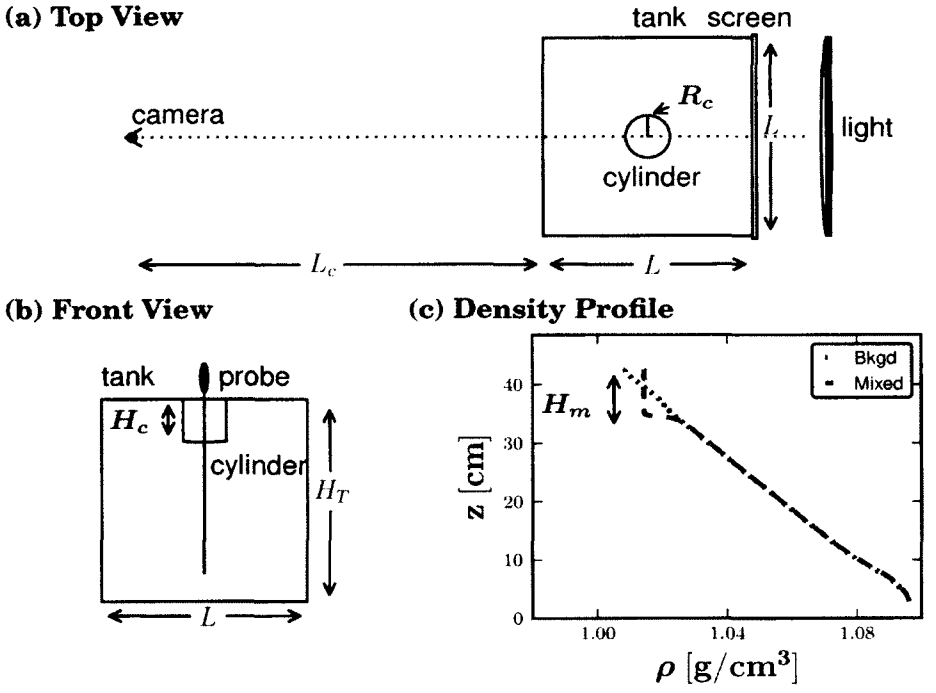

Figure 2.1: Schematic of experimental setup showing (a) Top view of the tank showing a hollow cylinder of radius R_c inserted at the centre of the tank. (b) Front view showing the partial depth, H_c, to which the cylinder was inserted. The conductivity probe traverses the fluid through the centre of the cylinder. (c) Density profile measurements before and after the fluid in the cylinder was mixed. The measured height of the mixed region, H_m, is indicated.

2.2 Experimental Setup

A schematic diagram of the laboratory set-up is shown in Figure 2.1(a). In order to take the best advantage of the Schlieren visualization method, the experiments were conducted in a rectangular tank that is $H_T = 48.5\,\text{cm}$ in height with a square base measuring $L = 47.5\,\text{cm}$ on each side. The "Double-Bucket" technique (Oster, 1965) was used to fill the tank with uniformly salt stratified fluid to a depth of approximately 45 cm.

To capture the small-scale motion of vertically propagating internal waves, a digital camera was situated in front of the tank and a screen of black and white lines was attached to the back. An array of fluorescent lights provided back illumination of the image screen from which light travelled through the tank. The Sony DCR-TRV6 CCD camera, situated $L_c \simeq 400\,\text{cm}$ from the

tank, was zoomed in so that the tank filled the field of view of the camera. The corresponding pixel resolution was 0.067 cm.

A hollow cylinder was inserted carefully (to avoid disturbing the stratification) into the centre of the tank to a partial depth, H_c. The set-up is illustrated in Figure 2.1(b). Two cylinders of radii $R_c = 3.85\,\mathrm{cm}$ and $5.05\,\mathrm{cm}$ were used in the experiments. The fluid within the transparent cylinder was thoroughly mixed to a depth H_m, moderately above H_c, with an oscillating mechanical stirrer. The fluid within the cylinder was then allowed to settle until turbulent motions subsided.

Traversing the fluid vertically, a conductivity probe (Precision Measurement Engineering Model II) measured the density as a function of depth. Two profiles were taken with the probe inserted through the centre of the cylinder. The first was taken before the fluid within the cylinder was mixed and provided a measure of the background density gradient. The second probe measurement was taken after the fluid in the cylinder was mixed and, from the density profile, the depth of the mixed region, H_m, was determined.

The total density is defined by where $\rho_{\mathrm{total}} = \rho_0 + \overline{\rho}(z) + \rho(x, y, z)$ where ρ_0 is the reference density at the top of the fluid, $\overline{\rho}$ is the background density and ρ is the perturbation density. An example of the density profiles for a particular experiment is shown in Figure 2.1(c). The background density profile shows that the fluid was uniformly stratified throughout the entire depth of the tank. The profile taken after the fluid in the cylinder was mixed shows that the density remained constant over the depth of the well-mixed region followed by a small transition region below which the fluid was uniformly stratified. The measured depth of the mixed region, H_m, was taken to be the distance between the surface and the top of the transition region.

The background density gradient was calculated by fitting a line to the ambient density profile, $\bar{\rho}(z)$, below the depth of the bottom of the cylinder. From this, we determined the frequency $N = \sqrt{(-g/\rho_0)(d\bar{\rho}/dz)}$, which ranged from $1.2\,\mathrm{s}^{-1}$ to $1.6\,\mathrm{s}^{-1}$.

The experiment proceeded by rapidly extracting the cylinder vertically. The mixed fluid collapsed under the force of buoyancy, moving upward and downward toward a level of neutral buoyancy. This motion caused the column of fluid beneath the cylinder to undulate up and down and internal waves immediately began to radiate from the undulating column. To examine the effect of varying the mixed region depth, three successive experiments were performed with $H_c \simeq 5\,\mathrm{cm}$, $10\,\mathrm{cm}$ and $15\,\mathrm{cm}$.

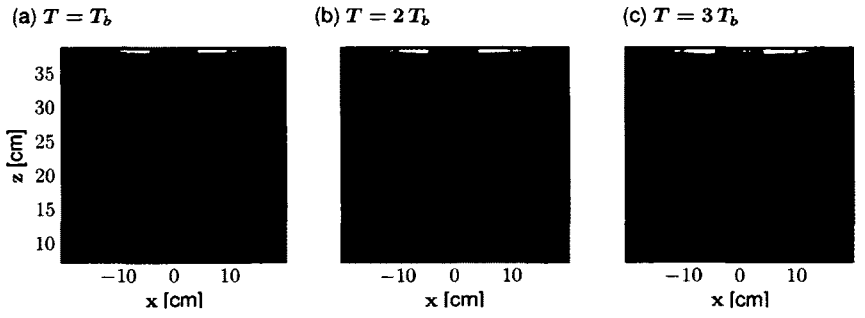

Figure 2.2: Snapshots of the experiment shown (a) one (b) two and (c) three buoyancy periods, $T_b = 2\pi/N$, after the cylinder was extracted. In this experiment dye was added to the mixed fluid to a depth $H_m \simeq 4.2\,\mathrm{cm}$ with an ambient stratification $N \simeq 1.4\,\mathrm{s}^{-1}$. The black and white lines on the back of the tank are used to measure fluctuations of the density gradient with Synthetic Schlieren.

Intruding into the stratified ambient, the mixed fluid flowed horizontally at the depth of neutral buoyancy approximately equal to half the depth of the mixed region, $H_m/2$. A top view of the experiment confirmed that the spreading of the intrusion was axisymmetric, and from the front view of the tank, we observed that the intrusion head thinned as it spread radially. It travelled at a near constant speed for the first two buoyancy periods then slowed over a duration of about one buoyancy period and stopped before reaching the edge of the tank.

In a few of the experiments dye was added to the mixed fluid to visualize the intrusion and to determine its speed. Figure 2.2 shows the evolution of the intrusion over three buoyancy periods in an experiment where $H_m \simeq 4.2\,\mathrm{cm}$, $N = 1.4\,\mathrm{s}^{-1}$ and $R_c = 5.05\,\mathrm{cm}$.

Isopycnal surfaces disturbed by internal waves caused the local density gradient to increase or decrease relative to the background density gradient. Synthetic Schlieren (Sutherland *et al.*, 1999; Flynn *et al.*, 2003) makes use of the optical principle that light rays bend more where the refractive index changes rapidly. By measuring vertical displacements of the image behind the tank of black and white lines having thickness (3 mm) and assuming the waves are axisymmetric, a simple matrix inversion is used to determine the vertical gradient of the fluctuation density field, $\partial_z \rho$.

This field is directly proportional to the change in the squared buoyancy frequency due to the waves $\Delta N^2(r, z, t) = -(g/\rho_0)\partial_z \rho$. The time rate of change

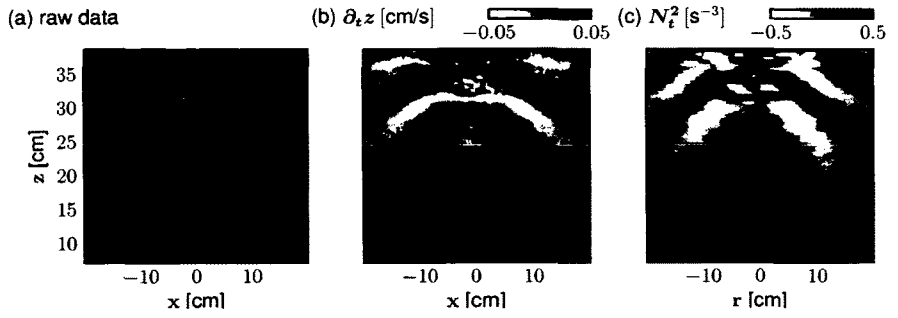

Figure 2.3: (a) A snapshot taken from the digital camera before the start of an experiment. The edges of the nearly transparent cylinder are visible. (b) The $\partial_t z$ field calculated using Synthetic Schlieren at $t = 2\,T_b$ (c) N_t^2 computed from $\partial_t z$ at the same t. Some asymmetry is observed between the left and right side of the image as each side was computed separately. For this experiment $N \simeq 1.5\,\mathrm{s}^{-1}$, $H_m \simeq 10\,\mathrm{cm}$ and $R_c = 5.05\,\mathrm{cm}$.

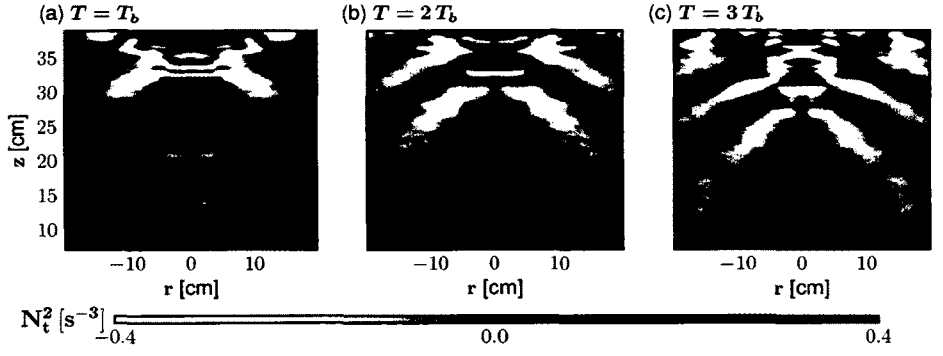

Figure 2.4: The N_t^2 field after (a) one (b) two and (c) three buoyancy periods. The parameters for this experiment are the same as those for the experiment in Figure 2.3. These images are symmetric as the left side is a reflection of the right.

of this field, N_t^2, is calculated by measuring differences in ΔN^2 between successive frames taken $\Delta t = 0.04\,\mathrm{s}$ apart and has the effect of filtering slowly evolving variations such as long hydrostatic waves at the level of the intrusion or ambient temperature and lighting changes in the laboratory. The N_t^2 field enhances changes due to internal waves which occur over relatively fast time-scales.

Figure 2.3 demonstrates the procedure used to calculate the N_t^2 field. The digital image shown in figure 2.3(a) was taken after the fluid in the transparent

cylinder was mixed and turbulent motions had ceased. It illustrates the thin horizontal lines that make up the Schlieren image screen. In this experiment $H_m \simeq 10\,\mathrm{cm}$, $N^2 \simeq 2.3\,\mathrm{s}^{-2}$ and $R_c = 5.05\,\mathrm{cm}$. Comparing an image taken two buoyancy periods after the extraction of the cylinder with an image taken Δt earlier we computed the vertical velocity of the apparent displacement, $\partial_t z$ shown in Figure 2.3(b).

Finally the $\partial_t z$ field is axisymmetrically inverted (Flynn *et al.*, 2003) to produce the N_t^2 field shown in Figure 2.3(c). Specifically, the image to the right of the centreline was inverted to determine the wavefield to the right. Separately, the left image of the $\partial_t z$ field was used to find the wavefield to the left. Figure 2.3(c) shows an example of the N_t^2 field which results from processing each side independently. If the processed images did not exhibit satisfactory reflection symmetry about the vertical centre line then the assumption of axisymmetry was shown to be incorrect (presumably because the cylinder was not well extracted vertically) and the experiment was excluded from analysis. For those experiments which did display the requisite symmetry, the entire N_t^2 field was determined from the right side of the image and used for subsequent analysis.

Figure 2.4 shows the evolution over three buoyancy periods of the N_t^2 field for the same experiment as that shown in Figure 2.3. The images show the downward propagation of wave cones emanating from the bottom of the collapsing mixed region. From this field the frequency, radial wavenumber, vertical displacement amplitude and integrated energy flux were computed.

Reynolds numbers were determined for the intrusive gravity current as well as for the vertically propagating internal waves. For the intrusion, $\mathrm{Re} = NH_m^2/\nu$ ranges from 4.3×10^3 to 3.8×10^4. Using a characteristic velocity of $U = \omega/k_r$ and a characteristic length scale of $L = k_r^{-1}$ the Reynolds number for the internal waves ranged from 2.1×10^2 to 8.3×10^2. These values were large enough that viscosity did not play a significant role in the evolution of the flow.

2.3 Theory and Analysis

The Navier-Stokes equations for small-amplitude, axisymmetric waves in a Boussinesq, incompressible and inviscid fluid are used to derive a differential equation describing the evolution of the streamfunction, $\psi(r, z, t)$, in polar coordinates (see appendix A for a description of coordinates). The stream-

Structure	Relation to A_ξ
$\xi = \frac{1}{2}A_\xi J_0(k_r r)e^{i(k_z z-\omega t)} + cc$	
$\psi = \frac{1}{2}A_\psi J_1(k_r r)e^{i(k_z z-\omega t)} + cc$	$A_\psi = -i\frac{\omega}{k_r}A_\xi$
$N_t^2 = \frac{1}{2}A_{N_t^2} J_0(k_r r)e^{i(k_z z-\omega t)} + cc$	$A_{N_t^2} = -k_z\omega N^2 A_\xi$
$w = \frac{1}{2}A_w J_0(k_r r)e^{i(k_z z-\omega t)} + cc$	$A_w = -i\omega A_\xi$
$u_r = \frac{1}{2}A_{u_r} J_1(k_r r)e^{i(k_z z-\omega t)} + cc$	$A_{u_r} = -\frac{k_z\omega}{k_r}A_\xi$
$p = \frac{1}{2}A_p J_0(k_r r)e^{i(k_z z-\omega t)} + cc$	$A_p = i\rho_0\frac{\omega^2 k_z}{k_r^2}A_\xi$

Table 2.1: Polarization relations for the vertical displacement (ξ), streamfunction (ψ), time change in the perturbed squared buoyancy field (N_t^2), vertical velocity (w), radial velocity (u_r), and pressure fields (p). The vertical wavenumber is given by $k_z = (k_r/\omega)\sqrt{N^2 - \omega^2}$.

function is defined so that $\mathbf{u} = \nabla \times (\psi\hat{\theta})$ and its structure may be represented by a superposition of Bessel and complex exponential functions.

The streamfunction and all other fields of interest are related to the vertical displacement, ξ, through the polarization relations (Ansong & Sutherland, 2009) listed in Table 2.1. Using the equations of motion, these relationships were derived by defining the vertical displacement such that $w = \partial\xi/\partial t$.

At a fixed vertical level z, the Fourier-Bessel transform is used to compute internal wave properties from radial time series of the N_t^2 field using

$$N_t^2(r,t) = \sum_{n=0}^{N}\sum_{m=0}^{M} A_{N_t^2}(k_n,\omega_m)J_0(k_n r)e^{-i\omega_m t}, \tag{2.1}$$

in which it is understood that the field is the real part of the sum. Here $k_n = \alpha_n/R$ is the radial wavenumber given in terms of the zeroes α_n of $J_0(r)$ where the radial extent $R = 20\,\text{cm}$ is just less than half of the width of the tank, $L/2$. We define $\omega_m = (2\pi/T)m$ where T is the duration of the time series. The vertical wavenumber can then be deduced from the dispersion relation $k_z = k_r\sqrt{(N/\omega)^2 - 1}$.

Figure 2.5 demonstrates the technique used to compute the peak values of frequency and wavenumber using the same experimental data that was used to produce Figure 2.3. First, the radial time series shown in 2.5(a) was transformed using the Fourier-Bessel series expansion given by equation (2.1)

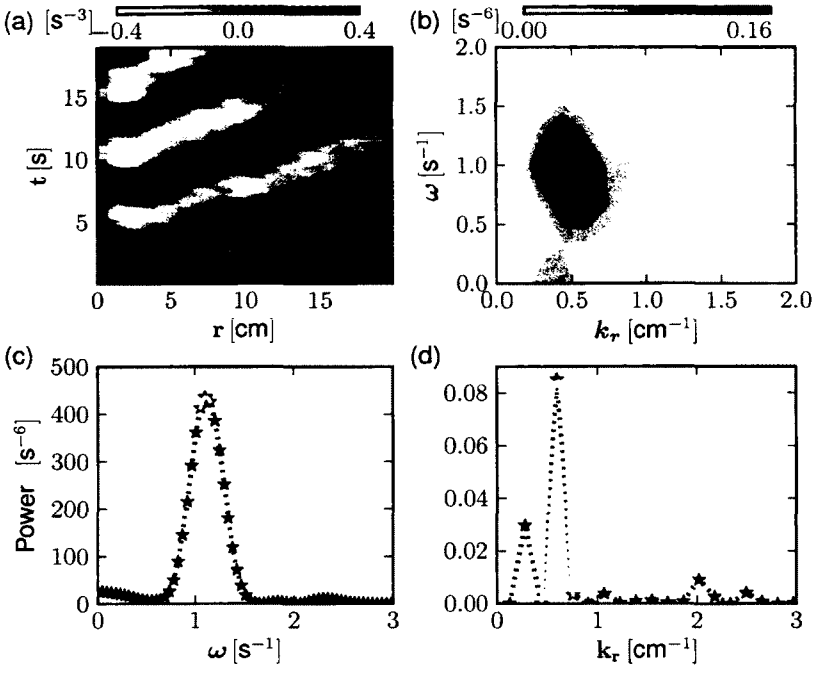

Figure 2.5: (a) A radial time series of the N_t^2 field taken 10 cm below the mixed region. (b) The corresponding frequency/wavenumber power spectrum $|A_{N_t^2}|$ computed from the time series. (c) Fourier Power spectrum for frequency, ω, fit with a parabola through three points about the maximum (gray line). (d) Bessel Power spectrum for radial wavenumber, k_r, fit with a parabola (gray line). The experimental parameters are the same as those given in Figure 2.3.

to find the amplitudes $A_{N_t^2}$. These were squared in magnitude to create the contour plot shown in Figure 2.5(b), which indicates the power associated with each discrete frequency and radial wavenumber. There is some spread in both frequency and wavenumber, yet most of the power is concentrated within a narrow range.

Isolating the dominant frequency involves Fourier transforming several vertical slices of the radial time series taken from the N_t^2 field. At fixed r, the squared Fourier coefficients are plotted as a function of frequency to create a Fourier power spectrum. The peak of this spectrum, ω_*, determines the central frequency of the wave-packet at each r (Fig. 2.5(c)). Similarly, the peak radial wavenumbers, k_*, were found for fixed times t from the power determined from successive Bessel transforms of N_t^2 (Fig. 2.5(d)).

Because of the finite domain size, Fourier-Bessel coefficients were determined at discrete values of k_n and ω_m. To increase precision in our determina-

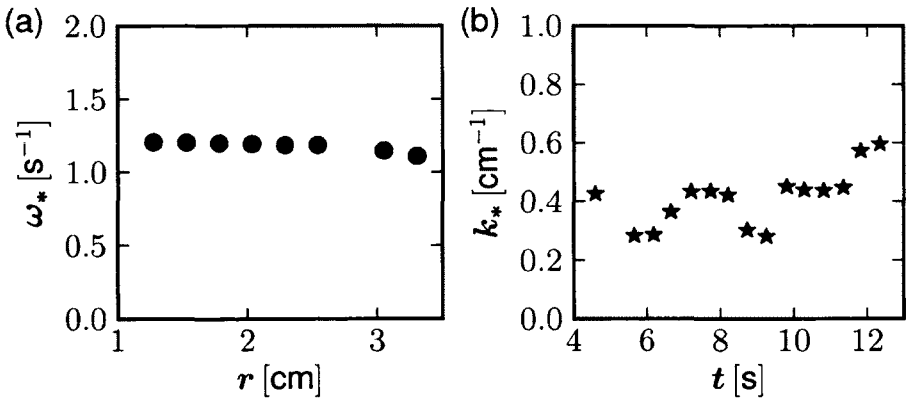

Figure 2.6: Peak values of (a) frequency and (b) radial wavenumber calculated from successive transforms of the radial time series shown in Figure 2.5.

tion of the dominant frequencies and wavenumbers a parabola was fit to three points about the maximum value in each power spectrum and the peak of that parabola was taken to be the peak of the spectrum.

Figure 2.6(a) shows the peak frequency, ω_*, for a range of r. The radial locations were chosen near the centre of the tank where the highest amplitude undulations of the fluid occurred and hence where the signal was strongest. Figure 2.6(b) shows k_* for several time steps chosen every eighth of a period over two buoyancy periods beginning one buoyancy period after the cylinder was extracted. These plots were averaged to obtain representative values of ω_* and k_* for waves at each vertical position z, along with their associated error estimates.

Finally, the peak frequencies and peak radial wavenumbers were averaged over a range of heights to arrive at a characteristic wavenumber, $\overline{k}_*$, and frequency, $\overline{\omega}_*$, for each experiment.

The amplitude of the vertical displacement field was derived from the N_t^2 field using the relationship between A_ξ and $A_{N_t^2}$ given by the polarization relations in Table 2.1 so that at a fixed level z

$$\xi(r,t) = \sum_{n=0}^{N}\sum_{m=0}^{M} \frac{-A_{N_t^2}(k_n,\omega_m)}{k_n N^2\sqrt{N^2-\omega_m^2}} J_0(k_n r)e^{-i\omega_m t}. \tag{2.2}$$

The maximum value of $|\xi|$ was found for several radial time series taken at different vertical locations to obtain the maximum vertical displacement of the waves near $r = 0$. A single characteristic vertical displacement amplitude was found for each experiment by averaging over $H_m - 11\,\text{cm} \leq z \leq H_m - 9\,\text{cm}$ and

the standard deviation of these values was used as a measure of uncertainty.

The range of heights used to evaluate $|\xi|$ were chosen as high as possible to maximize the amount of information that could be acquired before any waves reflected on the tank walls, while ensuring that any erroneous Schlieren measurements, due to turbulence in the mixed region, were avoided. For consistency amongst the experiments, the vertical slices used in the calculation of frequency and wavenumber, amplitude and energy were taken, in a 2 cm range, approximately 10 cm below the mixed region, H_m.

The flux of energy, $\mathcal{F}_E(z) = \int_0^{2\pi} \int_0^R wpr dr\, d\theta$, due to the internal waves crossing a fixed vertical level is transient during the process of collapse and re-stratification. Waves propagate downward and away from the mixed region eventually reaching the side of the tank and reflecting back towards the centre. However, experiments show that wave generation was most substantial during the first few buoyancy periods. To capture the majority of energy extracted by the waves while avoiding interference from reflecting waves at late times, $\mathcal{F}_E$ was integrated at a fixed height over two buoyancy periods to obtain the energy as

$$\begin{aligned} E &= \int_{T_1}^{T_2} \mathcal{F}_E \, dt \\ &= 2\pi^2 R^2 \rho_0 \sum_{n=0}^{N} \sum_{m=0}^{M} \frac{A^2_{N_t^2}(k_n, \omega_m) J_1(\alpha_n)}{k_n^3 \sqrt{|N^2 - \omega_m^2|} N^4}. \end{aligned} \tag{2.3}$$

In most experiments T_1 was taken to be one buoyancy period, $T_b = 2\pi/N$, after the start of the experiment. However, when H_m was small the waves took longer to propagate well below the mixed region so $T_1 = 2T_b$ was used for those experiments. In either case $T_2 = T_1 + 2T_b$.

To ensure that the energy estimate was as accurate as possible, the calculation involved summing over all frequencies and wavenumbers of the Fourier-Bessel spectrum. The integrated flux taken over two buoyancy periods decreased with increasing depth below the mixed region. For example, the profile for the experiment shown in Figure 2.3 is plotted in Figure 2.7. Large values immediately below the mixed region were a consequence of errors in the Schlieren measurement which gave unphysical results where the motion was turbulent. Further below, the energy decreased due to the transient nature of the waves that took a longer time to propagate a greater distance below the collapsing mixed patch.

A conservative estimate of the energy flux was therefore taken to be the

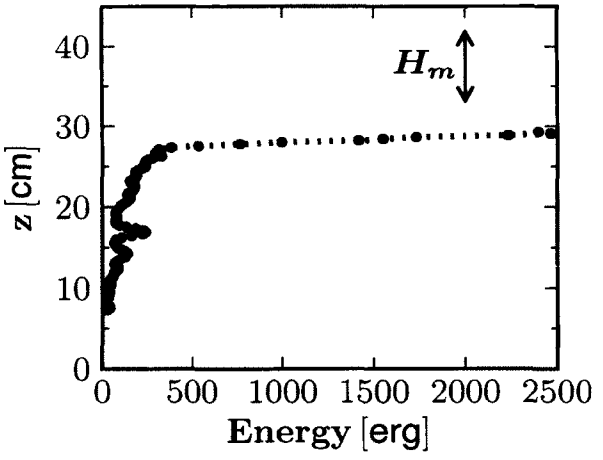

Figure 2.7: Typical energy profile. The time integrated flux given by equation (4.5) for the experiment shown in Figure 2.3.

average value of $\mathcal{F}_E(z)$ over a 2 cm range about a depth of 10 cm below the mixed region. Integration of the mean energy flux in time gives the energy through equation (4.5).

For analysis purposes, the energy (in Joules) is normalized by the initial available potential energy (APE). This is given by

$$APE = \int_0^{2\pi} \int_0^R \int_0^{H_m} (\bar{\rho}_i - \bar{\rho}_f) gz \; r dz dr d\theta, \tag{2.4}$$

in which $\bar{\rho}_i$ and $\bar{\rho}_f$ are initial and final density profiles, respectively, as determined by probe measurements shown, for example, in Figure 2.1. In the absence of mixing, the entire volume of fluid in the cylindrical lock would collapse to form a thin horizontal layer of uniform density (Sutherland, 2002). In our experimental set-up, the layer thickness is so small so that the final state is well approximated as a continuously stratified fluid. Thus, an estimate of the APE that ignores mixing may be expressed in terms of explicitly determined experimental parameters by

$$APE = \frac{\pi \rho_0 H_m^3 R_c^2 N^2}{12}. \tag{2.5}$$

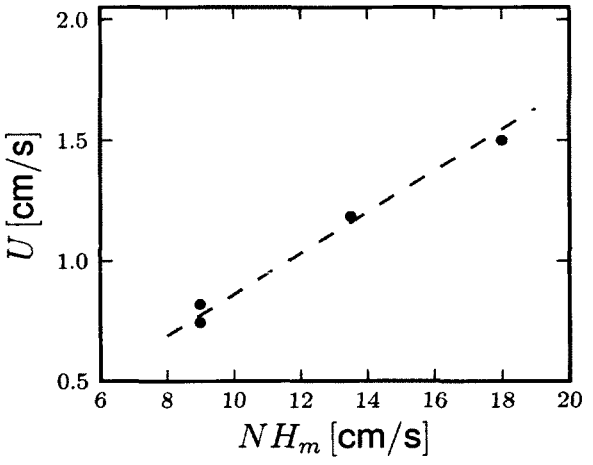

Figure 2.8: U is plotted against the characteristic velocity scale NH_m. The best fit line passing through the origin is shown as a dashed line.

2.4 Results

To determine if the waves were excited by the initial collapse as opposed to the propagating intrusion, intrusion speeds, U, were found by applying linear regression to radial time series that track the intrusion head at its level of neutral buoyancy. For a series of these experiments, U is plotted against the characteristic velocity scale NH_m in Figure 2.8. The slope of the best-fit line passing through the origin is the dimensionless Froude number $\mathrm{Fr} = U/NH_m = 0.085 \pm 0.001$. This is significantly smaller than the value $\mathrm{Fr} = 0.13 \pm 0.02$ measured for rectilinear intrusions (Sutherland *et al.*, 2007) generated by the collapse of a mixed region in stratified ambient and smaller than the value $\mathrm{Fr} = 0.125$ predicted by linear theory (Bolster *et al.*, 2008).

The axisymmetric geometry used in our experiments may act to slow the intrusion through lateral spreading and consequent reduction of head height. A detailed explanation for the lower and constant observed speed is being examined in research distinct from this study.

If internal waves are excited by the head of the intrusion then the speed of the intrusion should set the phase speed of the waves, $c_p = \omega/k_r$, and the plot of ω/N against $k_r H_m$ should exhibit the same linear relationship as U against NH_m. Figure 2.9 shows this is not the case. Instead, ω/N is relatively constant with respect to $k_r H_m$. Moreover, snapshot images show that lines of

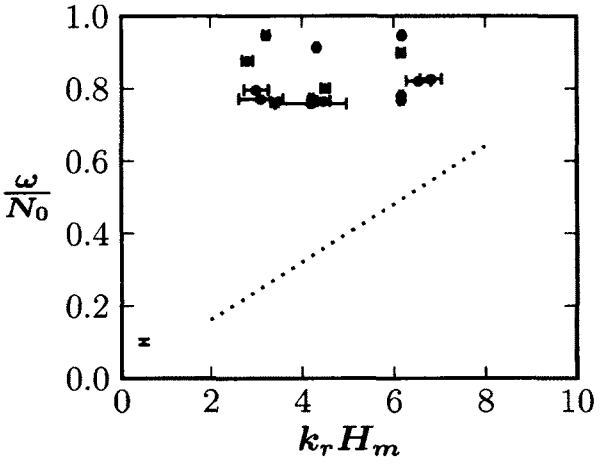

Figure 2.9: Non-dimensional plot of ω/N against $k_r H_m$. The dotted line has slope Fr $= 0.085 \pm 0.001$ which is the Froude number measured from the intrusion speeds. A characteristic vertical error bar is shown in the lower left hand corner.

constant phase emanate from below the mixed region and not the intrusion front. This further suggests that the oscillating fluid below the collapsing mixed region launches the waves.

The values of ω/N, which lie within a narrow range about 0.8, indicate that the frequency of the waves is set by the buoyancy frequency. A narrow range of relative internal wave frequencies was also observed in rectilinear studies of collapsing mixed regions in uniformly stratified fluid (Wu, 1969; Sutherland *et al.*, 2007; Munroe *et al.*, 2009) for which $0.6 \leq \omega/N \leq 0.8$. It is at a frequency of $0.8N$ that internal gravity waves most efficiently transport energy and hence exert the greatest feedback on the source that generates them (Dohan & Sutherland, 2003; Sutherland *et al.*, 2004*a*).

We expect that the radius of the cylinder sets the wavelength of the waves. Figure 2.10 shows that the value of k_r relative to the radius of the cylinder lies in a range of $k_r R_c$ between 1.5 and 3.5, with most values near 2. Using the relationship $k_r R_c \simeq 2$, we find the first zero crossing of $J_0(k_r r)$ is $\alpha_0 \simeq 1.2R_c$. Because this is approximately equal to the radius of the cylinder, it strongly supports the hypothesis that the radius of the cylinder sets the radial wavelength, λ_r. An asymptotic expansion of the Bessel function shows that the wavelength is $2\pi/k_r$ with amplitude decaying from the source as $r^{-\frac{1}{2}}$.

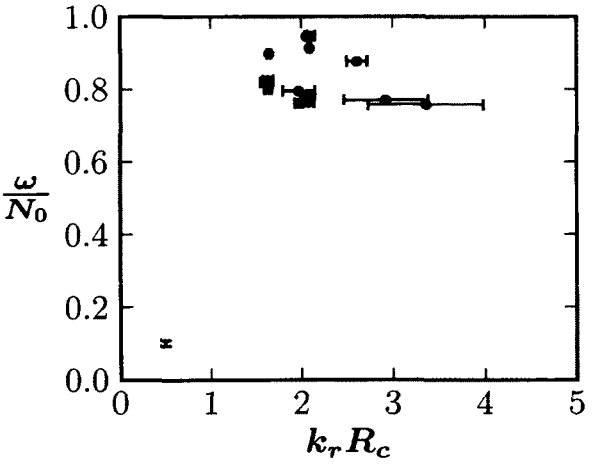

Figure 2.10: Relative frequency plotted with relative radial wavenumber for a range of experiments. A characteristic vertical error bar is shown in the lower left hand corner.

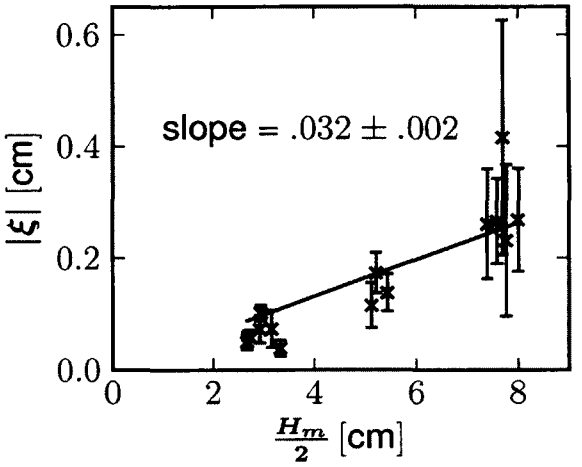

Figure 2.11: The maximum amplitude of the vertical displacement field plotted against half the height of the mixed region. A best fit line passes through the origin with given slope.

The maximum vertical displacement amplitude is plotted against the height of the mixed region in Figure 2.11. Although the amplitudes do not vary much from experiment to experiment, over a narrow range the amplitude is observed

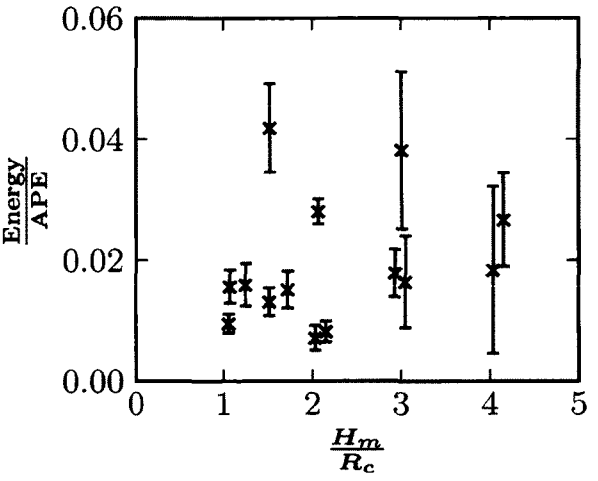

Figure 2.12: The integrated energy flux normalized by the available potential energy is plotted against the height of the mixed region normalized by the radius of the cylinder.

to increase linearly as a function of the depth of the mixed region. In the absence of a mixed region ($H_m = 0$) no internal waves are generated and so $|\xi| = 0$. A line passing through the origin is fit to the data resulting in a slope of $|\xi| / (H_m/2) = 0.032 \pm 0.002$. That is, the vertical displacement amplitude is 3.2% the half-depth of the mixed region. This small fraction indicates that most of the energy released by the collapse goes into the radial motion of the intrusion and return flows.

Figure 2.12 shows the potential energy carried away by downward propagating internal waves for each experiment over 2 buoyancy periods given as a percentage of the APE. Despite the scatter in Figure 2.12, the measurements give a useful order-of-magnitude estimate of the energy extracted by the waves. The average amount of potential energy imparted to the internal wavefield from the mixed region is found to be on the order of 2%. This fraction may be considered an underestimate because it measures only the energy associated with the transient waves occurring before they reflect from the boundaries of the tank.

This result is smaller than that found for rectilinear intrusions (Sutherland *et al.*, 2007) in which almost 10% of the APE was extracted by internal waves over two buoyancy periods. The fraction of energy extraction is consistent with a recent study examining internal waves generated by axisymmetric convective

plumes (Ansong & Sutherland, 2009) for which the energy associated with the internal waves at the level of neutral buoyancy was around 4% of the plume's kinetic energy.

An explanation for the relative decrease in internal wave energy is provided by examining the relationship between the collapsing fluid and the internal wavefield. This is mediated by the return flow that moves inward immediately above and below the intrusion in order to replace fluid lost to the outflow. The energy imparted to internal waves is governed by the kinetic energy and ultimately the speed in the return flow which, in turn, is governed by the intrusion's speed. Because mass conservation dictates that the nose of the intrusion decreases in height as it spreads laterally in an axisymmetric geometry, the return flow is not as fast as the rectilinear case.

2.5 Discussion and Conclusions

The axisymmetric collapse of a localized mixed region in a stratified ambient generates an intrusion and excites vertically propagating internal gravity waves in the underlying stratified fluid. Our analysis suggests that the frequency of these waves is set by the buoyancy frequency of the fluid and the wavelength is set by the radius of the mixed patch. Vertical displacement amplitudes are relatively small and increase as the depth of the patch increases according to the relation $|\xi| / (H_m/2) = 0.032 \pm 0.002$. We found the amount of energy transported by the waves over two buoyancy periods to be on the order of 2% of the system's available potential energy.

In the absence of rotational effects, turbulence, and wind induced currents, adapting our results directly to oceanic circumstances of storms generating internal waves is premature, but is the first step towards quantifying the fraction of energy available for deep ocean mixing from the collapsing mixed region following a moving hurricane. Since the waves scale with the collapsing mixed region, we can conclude that turbulence within the mixed patch does not contribute to the generation of the measured internal waves. Subsequent energy considerations are specifically associated with the collapse of the mixed region as a mechanism for the generation of internal waves which transport energy to the region underlying the mixed region.

Emanuel (2001) gives a simple example using parameters characteristic of Hurricane Edouard, which left a cold water wake with a temperature change of 3°C to a depth $H_m \simeq 50\,\mathrm{m}$, and along-track and cross-track lengths of 2000 km

and 400 km, respectively.

Using the established relationship between the height of the mixed region and the vertical displacement field, we predict the amplitude of the waves to be $|\xi| \simeq 0.8\,\mathrm{m}$. The area traversed by a hurricane is not radially symmetric, but for predictive purposes we assume that the radius of the mixed patch is at least as big as half the cross-track dimension, 200 km. Because we found $k_r \simeq 2/R_c$ we predict that the radial wavelength of the internal waves would be $\lambda \simeq 600$ km.

Buoyancy frequencies observed in the open ocean can vary from about $0.0008\,\mathrm{s}^{-1}$ (Pinkel & Anderson, 1997) to $0.009\,\mathrm{s}^{-1}$ (Ladd & Thompson, 2000) so that the buoyancy period, T_b, can range from 10 minutes to over 2 hours. Since $\omega = 0.8N$, corresponding wave frequencies range from $6 \times 10^{-4}\,\mathrm{s}^{-1}$ to $7.2 \times 10^{-3}\,\mathrm{s}^{-1}$.

Liu *et al.* (2008) estimate that the passing hurricane increases the system's available potential energy at a rate of 0.16 TW so we conservatively assume that 10^{17} J of APE contributes to the collapse of the mixed region during the 18 day lifespan of the storm. The amount of energy extracted by the internal waves in our experiments varied from about $1\% - 5\%$ of the system's available potential energy which amounts to $10^{15} - 5 \times 10^{15}$ J of wave energy over $2T_b$. This indicates that $6 \times 10^{10} - 4 \times 10^{12}$ W of power is input to the internal wavefield from a single moving hurricane over two buoyancy periods. These values are comparable to the steady and globally distributed power associated with the tides, but it must be emphasized that wave generation by a hurricane is a localized and transient event.

Hurricanes occur infrequently and over short time-scales. So a globally averaged annual estimate of the energy extracted by deep ocean internal waves provides a more conservative estimate of the influence of hurricane-generated internal waves relative to those generated by the tides.

There are about 80 tropical cyclones each year (Emanuel, 2001) of which about 50 develop into hurricane strength storms. Using an annual average, we find that the power input from tropical cyclones to the internal wavefield from the collapse of the mixed region ranges from 1×10^9 W to 8×10^9 W. This result is comparable to Nilsson (1995) 1 GW estimate of the power transported away, horizontally, by near inertial waves that manifest as undulations of the thermocline. Because the internal waves in our study propagate vertically, they would have a more significant impact upon mixing in the oceanic abyss.

By extrapolating the results of our laboratory experiments, we have shown

that internal waves left in the wake of a moving hurricane can transport a significant amount of energy through the stable stratification of the deep ocean abyss where they may contribute to deep ocean mixing. Because hurricanes and mixed region collapse evolve on time-scales comparable to the earth's rotational period, in the next stage of our research we will extend these experiments by performing them on a rotating table thus simulating the Coriolis effects.

Chapter 3

Intrusions in Stratified Fluid and the Influence of a Uniform Background Rotation

3.1 Introduction

In this chapter, we present a series of lock-release laboratory experiments that examine the collapse of a localized cylindrical mixed patch of fluid in both two-layer and uniformly stratified ambient. They were performed with and without rotation and focus on the evolution of the intrusion.

Unlike bottom propagating gravity currents, non-rotating intrusions typically propagated many lock radii at constant speed, sometimes stopping abruptly. The experiments performed here show that internal waves play a crucial role in the evolution of the intrusion. For asymmetric cases, the radial advance of the intrusion was slowed or even halted by interactions with mode-1 waves launched by the return flow.

Rotation can also limit the maximum distance propagated by the intrusion. In the two-layer case, rotation caused the patch to periodically release outward pulses as it approached equilibrium. Whereas, in uniformly stratified fluid, the oscillatory motion of the patch was relatively smooth.

The experimental set-up and the methods used to analyze the intrusion speeds are presented in Sec. 3.2 with the results shown in Sec. 3.3. Conclusions are given in Sec. 3.4.

3.2 Set-up and Analysis Methods

3.2.1 Experimental Setup

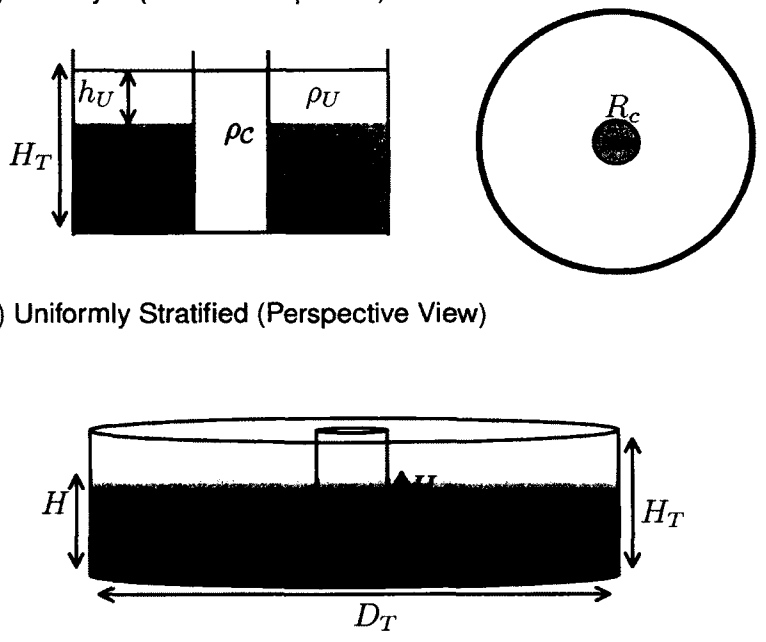

Figure 3.1: Experiments were performed in a cylindrical tank of height H_T and inner diameter $D_T = 90.7\,\mathrm{cm}$ with a hollow cylindrical lock of radius R_c. The tank was filled to a total depth H. (a) The two-layer experiments consisted of a lower (upper) layer depth h_L (h_U) with density ρ_L (ρ_U) and a full-depth lock, whereas in (b) the uniformly stratified experiments the inner cylinder was suspended to a partial-depth H_c.

Figure 3.1 illustrates the laboratory setup for (a) two-layer and (b) uniformly stratified experiments. All experiments were performed in a cylindrical acrylic tank of height $H_T = 30.0\,\mathrm{cm}$ and inner diameter of $D_T = 90.7\,\mathrm{cm}$. The tank was centred on a Geophysical Fluids Rotating Table (Australian Scientific Instruments) which can rotate at frequencies Ω between 0.020 and $15.00\,\mathrm{s}^{-1}$. A series of experiments were performed while the tank was stationary and another series were performed with the fluid rotating initially in solid body rotation.

A monochrome COHU CCD camera was situated on a metal frame 2 m directly above the centre of the tank to record a top view of the experiments. From these, time series were constructed showing the radially spreading flow.

As shown in Figure 3.1(a) the two-layer experiments consisted of a salty lower layer of density ρ_L and height h_L below a freshwater layer of depth h_U and density ρ_U. In all experiments $H = h_L + h_U = 10\,\text{cm}$ was the total depth of the fluid.

For the two-layer experiments, a small amount of dye was added along the density interface. Evenly spaced lines at the base of the tank were used to establish an accurate coordinate system.

The experiments were performed shortly after the two-layer stratification was established so as to minimize diffusion across the interface. However, some mixing did occur during the filling stage and resulted in a typical interface half-thickness of $h_\rho \simeq 0.5\,\text{cm}$.

A hollow acrylic cylinder of radius $R_c = 6\,\text{cm}$ was then carefully inserted in the centre of the tank and extended to the full-depth of the fluid. This formed a lock. The fluid within the lock was mixed so that the density of the fluid ρ_C was the depth-weighted average density of the background fluid. In some of the experiments this density was increased or decreased, respectively, by adding salt or displacing a quantity of fresh water within the cylinder.

A small amount of food colouring was then mixed into the lock to visualize the intrusion. Density measurements indicated that the dye did not significantly affect the density of the lock-fluid. After the turbulence from mixing the lock-fluid had dissipated the cylinder was rapidly extracted vertically using a string and pulley system that helped ensure a vertical extraction.

The Reynolds numbers, $\text{Re} = U_{2L}H/\nu$, ranged from 2×10^3 to 1×10^4. In the rotating two-layer experiments the rotation rates ranged from of $\Omega = 0.05\,\text{s}^{-1}$ to $\Omega = 0.2\,\text{s}^{-1}$.

Figure 3.1(b) shows the experimental setup for the continuously stratified fluid experiments. The tank was filled with salt stratified fluid to a depth H (between 17 cm and 19 cm) using the standard "Double-Bucket" technique (Oster, 1965). For experiments with rotation, the water in the buckets was allowed to reach room temperature before filling the tank to minimize the effects of double diffusion during the lengthy spin-up process. Measurements of the density were taken at several heights to verify that the background density increased linearly with increasing depth. Linear regression was then applied to the measurements of the ambient density profile, $\bar{\rho}(z)$, to find the density gradient. From this we determined the buoyancy frequency, which ranged from $N = 0.53\,\text{s}^{-1}$ to $2.27\,\text{s}^{-1}$.

For the uniformly stratified experiments, a grid of evenly spaced lines

placed at the top of the fluid was used to establish the coordinates at the level of the intrusion by making a simple adjustment for the index of refraction using Snell's law.

The value of ρ_C was not measured directly for all of the stationary experiments. So the measured value of H_m was used instead for the non-rotating cases.

Taking care not to disturb the ambient stratification, a hollow acrylic cylinder of radius $R_c = 5.3$ cm was inserted into the centre of the tank and suspended at depth H_c. The fluid within the transparent cylinder was then mixed with a torsionally oscillating mechanical stirrer to a depth H_m, moderately smaller than H_c. To examine the effect of varying the mixed-region depth we examined a range of experiments with H_m between 2 cm and the full-depth of the fluid, H.

The partial-depth mixed layer, H_m, could be measured visually from side views before the start of an experiment. To determine H_m more accurately, measurements were taken of the density of the lock-fluid, ρ_C. In combination with the measured density profile, ρ_C was used to compute the depth below the surface $z_C = H_m/2$, at which the intrusion propagated along its level of neutral buoyancy.

Like the two-layer fluid experiments, the lock-fluid was dyed, mixed and the cylinder was extracted once the residual turbulence had vanished. A metal cylinder and rod were used both to suspend and to guide the cylinder during extraction.

For the uniformly stratified fluid experiments the Reynolds number $\mathrm{Re} = NH_m^2/\nu$ ranged from 8.5×10^2 to 7.0×10^4. In the rotating experiments the tank was gradually rotated up to a frequency of $0.02 \leq \Omega \leq 0.3$. Dye lines ensured the entire volume of fluid was ultimately in solid body rotation. This spin-up process typically took over 12 hours. Measurements of the density profile $\bar{\rho}(z)$ taken before and after spin-up indicated that the stratification was not changed during the spin-up process.

In all of the experiments the intrusion moved at near-constant speed, U, shortly after being released from the lock. Only those experiments in which the intrusion propagated axisymmetrically were analyzed.

3.2.2 Theory and Analysis

Lock exchange experiments have been used to study intrusions of uniform density, ρ_C, in a two-layer ambient fluid with an upper (lower) layer density ρ_U (ρ_L) of depth h_U (h_L). The speed of the intrusions may be characterized by two independent non-dimensional parameters, ϵ and Δ. The relative density difference between the intrusion and the average density of the ambient is represented by

$$\epsilon \equiv \frac{\rho_C - \langle\rho\rangle}{\rho_L - \rho_U}, \tag{3.1}$$

where

$$\langle\rho\rangle \equiv \frac{h_U\rho_U - h_L\rho_L}{H} \tag{3.2}$$

is the depth-weighted average ambient density.

The relative difference between the upper and lower layer depths is represented by

$$\Delta \equiv \frac{(h_U - h_L)}{H} \tag{3.3}$$

in which $H = h_U + h_L$. We explored a range of density configurations characterized by the experimental parameters $|\Delta| \leq 0.667$ and $-0.237 \leq \epsilon \leq 0.675$.

When $\epsilon = 0$ and $\Delta = 0$ the intrusion is vertically symmetric and equal masses of lock-fluid are transported in each layer. This circumstance has been studied extensively in laboratory experiments (Holyer & Huppert, 1980; Britter & Simpson, 1981; Lowe *et al.*, 2002). Following the approach of Benjamin (1968), Holyer & Huppert (1980) made the first prediction of intrusion speeds in vertically symmetric cases with ϵ and/or Δ non-zero. However, Sutherland *et al.* (2004*b*) found that the theory was in agreement with their experiments for intrusions only if $\epsilon = 0$. If ϵ differed moderately from zero, the theory significantly underpredicted the speeds.

When $\epsilon \neq 0$ the interface ahead of the intrusion was depressed or elevated by the intrusion. This generated a long interfacial wave that propagated ahead of the intrusion. Cheong *et al.* (2006) made a prediction of the front speed in the case where $\epsilon = 0$ by considering the energy associated with each layer. Observing that an internal wave moving ahead of the intrusion modified the front condition for the intrusion, Flynn & Linden (2006) independently derived a prediction of the speed in the more general case of arbitrary ϵ. Recasting

the formula for the speed in terms of ϵ and Δ gives

$$U_{2L} = \frac{1}{4}\sqrt{g'H}\sqrt{1 - \Delta^2 + 4\Delta\epsilon} \tag{3.4}$$

where $g' \equiv (\rho_L - \rho_U)/\rho_0$.

Ungarish (2006) used shallow water theory to predict the speed of gravity currents beneath uniformly stratified ambient. However, by requiring the flow to be hydrostatic, the theory could not be extended to intrusions which excite non-hydrostatic internal waves Munroe *et al.* (2009).

Following the approach of Cheong *et al.* (2006), Bolster *et al.* (2008) predicted the speed of intrusions in uniformly stratified fluid with buoyancy frequency $N = \sqrt{(-g/\rho_0)(d\bar{\rho}/dz)}$ where $\bar{\rho}$ is the background density profile. Their formula was recast in terms of ϵ by Munroe *et al.* (2009) to give

$$U_N = \frac{1}{4}NH\sqrt{3\epsilon^2 + \frac{1}{4}}. \tag{3.5}$$

Here ϵ is given by equation (3.1) where ρ_L corresponds to the density at the bottom and ρ_U corresponds to the density at the fluid surface and $\langle\rho\rangle$ is the average of the two densities.

In partial-depth lock-release experiments (Sutherland *et al.*, 2007) in uniformly stratified fluid the intrusion was found to evolve as if released from a full-depth lock in a tank of depth H_m in which H_m is height of the mixed lock-fluid. Taking $\epsilon = 0$ and $H = H_m$ in equation (3.5), the speed is given by

$$U_{NP} = \frac{1}{8}NH_m. \tag{3.6}$$

This result agrees with the experimentally determined Froude number (Sutherland *et al.*, 2007) of $U/NH_m = (0.13 \pm 0.02)$.

An example of a vertically symmetric intrusion moving along a sharp interface in a two-layer fluid ($\epsilon = 0$, $\Delta = 0$) is shown in Figure 3.2. The top view in (a) shows that the radially spreading intrusion shortly after release from the lock remains nearly axisymmetric. The time series in (b) is constructed across the diameter in the x-direction. This clearly shows the advance of the intrusion head at near-constant speed for at least 6 lock radii.

Figure 3.2(b) also illustrates how the position of the intrusion head was tracked as it advanced in time. Linear regression was used to obtain a measure of the near-constant speed as the slope of the line shown. Slopes were computed on both sides of the time series. These slopes were then averaged with slopes measured from another time series taken across the diameter in

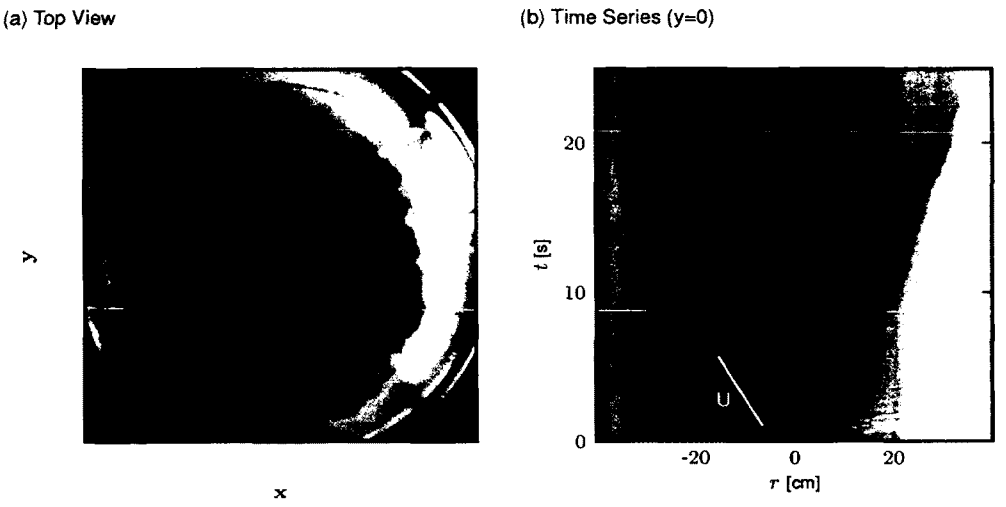

Figure 3.2: Two-layer experiment with $\Delta = 0$, $\epsilon = 0$, $\rho_L = 1.0504\,\mathrm{g/cm^3}$, $\rho_C = 1.0248\,\mathrm{g/cm^3}$ shown from (a) the top view taken when $t \simeq 10\,\mathrm{s}$ and (b) as a time series constructed across the diameter in the x-direction. The slope of the white line shown gives the speed, U, of the current.

the y-direction. The standard deviation amongst these values was used as an estimate of the error in measurement.

The Rossby number describes the relative importance of inertia and rotation and is given by

$$\mathrm{Ro} = L_D/R_c \tag{3.7}$$

where R_c is the radius of the cylindrical lock. L_D is defined by equation (1.4) and the characteristic velocity, U_c, used for the two-layer and uniformly stratified cases was taken from equations (3.4) and (3.5) respectively, with equation (3.6) being used for partial-depth lock-release experiments. Accordingly, Ro is defined a priori, in terms of the independent experimental parameters, rather than from measured quantities. For $\mathrm{Ro} \gg 1$ inertial forces dominate and the adjustment of the patch is expected to behave similarly to the non-rotating case. However, for small values of the Rossby number, $\mathrm{Ro} \ll 1$, the current is expected to be influenced by rotation during the slumping phase and then rapidly adjust to geostrophic balance.

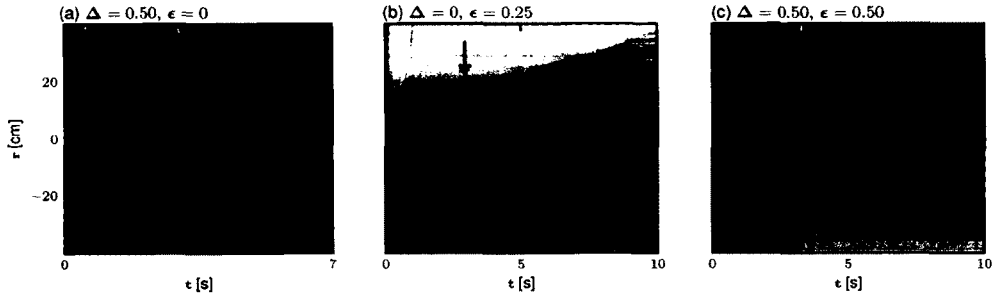

Figure 3.3: Time series taken from non-rotating experiments in a two-layer fluid with $H = 10\,\text{cm}$, $R_c = 6\,\text{cm}$, and (a) $h_L = 2.5\,\text{cm}$, $\rho_L = 1.1047\,\text{g/cm}^3$, $\rho_C = 1.0248\,\text{g/cm}^3$, (b) $h_L = 5\,\text{cm}$, $\rho_L = 1.051\,\text{g/cm}^3$, $\rho_C = 1.0375\,\text{g/cm}^3$, (c) $h_L = 2.5\,\text{cm}$, $\rho_L = 1.1047\,\text{g/cm}^3$, $\rho_C = 1.0781\,\text{g/cm}^3$.

3.3 Results

3.3.1 Non-rotating Experiments

For all the non-rotating experiments, the cylindrical gate was extracted and the lock-fluid collapsed spreading radially outward. Simultaneously return flows above and below the intrusion's head moved inward to replace the lock-fluid. The intrusion propagated outward at near-constant speed for a distance of at least 1.5 lock radii and, for the vertically symmetric two-layer experiments, often exceeded 7 lock radii. In the two-layer experiments the duration of the constant speed regime depended on the parameters ϵ and Δ.

Time series for distinct ϵ and Δ cases are shown in Figure 3.3. As in the vertically symmetric case shown in Figure 3.2 when $\epsilon = 0$ and $\Delta \neq 0$ (Figure 3.3(a)) the intrusion propagated radially at near-constant speed until impacting the side wall of the tank.

When $\epsilon \neq 0$, $\Delta = 0$ the intrusion stalled after propagating a short distance from the lock, slowing to the point of almost stopping. Then it accelerated once more and propagated outward until it impacted the tank wall. This stalling behaviour is indicated by the black arrow in the time series in Figure 3.3(b).

When $\epsilon \neq 0$ and $\Delta \neq 0$ the intrusion's behaviour was remarkably different, as shown in Figure 3.3(c). The intrusion propagated at near-constant speed a relatively short distance from the lock and then rapidly came to a halt. In some experiments, the intrusion stalled temporarily after propagating some distance from the lock, but then accelerated again moving a short distance

again before stopping.

As in the corresponding rectilinear intrusion study (Sutherland *et al.*, 2004*b*), the qualitative features that distinguish the various cases are explained by considering interactions of the intrusion with interfacial waves. When $\epsilon = 0$, a mode-1 interfacial wave is not efficiently excited ahead or behind the intrusion. Instead, a mode-2 interfacial wave surrounds the intrusion head and carries it forward at constant speed even as the head height decreases (McMillan & Sutherland, 2010). The stalling and stopping of the intrusion in cases where $\epsilon \neq 0$ is attributed to interactions of the intrusion with a mode-1 interfacial wave launched by the return flow that enters the lock at different speeds above and below the interface. This vertically asymmetric forcing of the interface launches a large amplitude mode-1 wave that catches up with the intrusion head and stops it.

Figure 3.4 shows the measured intrusion speeds plotted as a function of the theoretically predicted speed, $U_{2\mathrm{L}}$, given by equation (3.4). Experiments were distinguished according to Δ and ϵ, as indicated by the legend. The dashed line, $U = U_{2\mathrm{L}}$, shows that the speeds predicted for rectilinear intrusions were higher than the measured speeds for all of the experiments. Applying linear regression revealed that $U = (0.72 \pm 0.04)U_{2\mathrm{L}}$. The standard error in slope may be deceptively small as a consequence of requiring the fit line to pass through zero so the root mean squared error (RMSE) is also reported. The root mean square error is given by RMSE $= \sqrt{(y-U)^2/n} = \pm 0.54$ where U is the experimentally determined value and y is the value obtained through linear regression.

An example of a continuously stratified experiment is shown in Figure 3.5. The partial-depth mixed region in the lock collapsed after the cylinder was extracted moving along the level of neutral buoyancy at a depth of $z_C \simeq H_m/2$ below the surface of the fluid. The intrusion head thinned as it propagated out radially, moving at near-constant speed for approximately $3R_c$ before rapidly stopping.

Figure 3.6 shows the measured intrusion speeds plotted against the theoretical intrusion speed, U_{NP}, given by equation (3.6). The dashed line, $U = U_{\mathrm{NP}}$, shows that rectilinear theory consistently over-predicted the speeds. The slope of a best-fit line passing through the origin gives $U = (0.69 \pm 0.04)U_{\mathrm{NP}}$ (RMSE: ± 0.18). This value is consistent with the slope found for axisymmetric intrusions in non-rotating environments, (Holdsworth *et al.*, 2010) but is significantly smaller than the value $U \simeq 1.04U_{\mathrm{NP}}$ measured for rectilinear intrusions

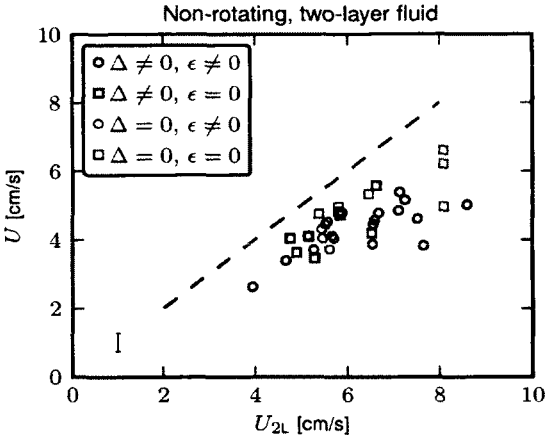

Figure 3.4: The measured speeds U plotted against the theoretical speeds U_{2L} predicted by equation (3.4). Experiments were categorized according to values of ϵ and Δ as indicated by the legend. The line $U = U_{2L}$ is plotted and shows that on average the observed speed of the intrusion was less than the speed predicted by rectilinear theory. A characteristic vertical error bar is shown in the lower left corner of the plot.

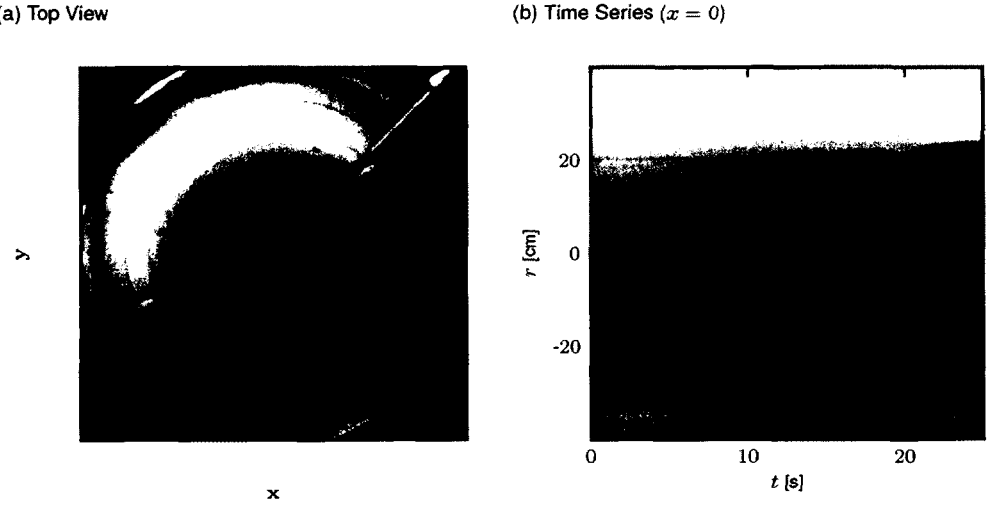

Figure 3.5: Intrusion in uniformly stratified fluid shown from (a) the top view taken when $t \simeq 4\,\mathrm{s}$ and (b) as a time series constructed across the diameter in the y-direction. The partial-depth lock-release experiment had $H_m = 8\,\mathrm{cm}$, $N = 1.6\,\mathrm{s}^{-1}$ and $R_c = 5.3\,\mathrm{cm}$.

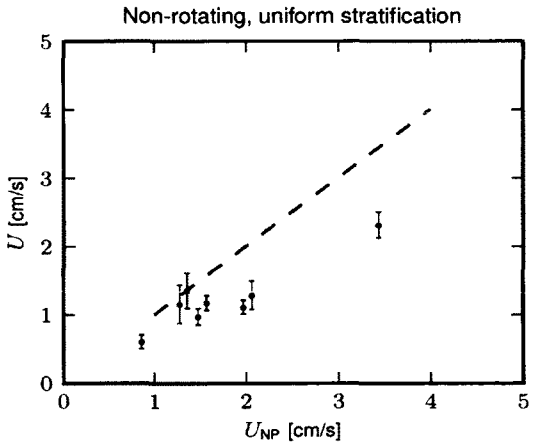

Figure 3.6: The measured speeds U are plotted against the theoretical speeds given by equation (3.6). Rectilinear theory overpredicts the speed of the outgoing intrusion which is shown by the plotted line $U = U_{\text{NP}}$.

(Sutherland *et al.*, 2007) generated by the collapse of a mixed region in stratified ambient.

The distance over which the intrusion decelerated to a halt was relatively short and a self-similar regime was not evident. Typically, $R_{\max}$ was between $1.5R_c$ and $4R_c$. Even for full-depth lock-release experiments in uniformly stratified fluid ($H_m = H$) the intrusion did not impact the side walls of the tank. Some lateral oscillations were exhibited by the patch and were attributed to interactions of the intrusions with internal waves excited ahead of the intrusion reflecting off the tank side walls as well as by internal waves generated by the return flow into the lock. However, the stopping distance was attributed to the return flow into the lock launching interfacial waves that caught up to the intrusion head. These dynamics were observed in a rectilinear geometry by Munroe *et al.* (2009).

Figure 3.7 shows that the stopping distances were within error of the estimate, R^*, predicted through extension of Munroe *et al.* (2009) who considered the time for a mode-1 wave launched by the return flow into the lock to catch up to the radial front of the intrusion. The wave was assumed to travel at speed $c = NH_m/\pi$ and traversed a distance $R_{\max} + 2R_c$ before reaching the front.

Because the geometry of the experiments did not allow us to capture vertical cross-sections of the flow evolution, we implemented a fully non-linear

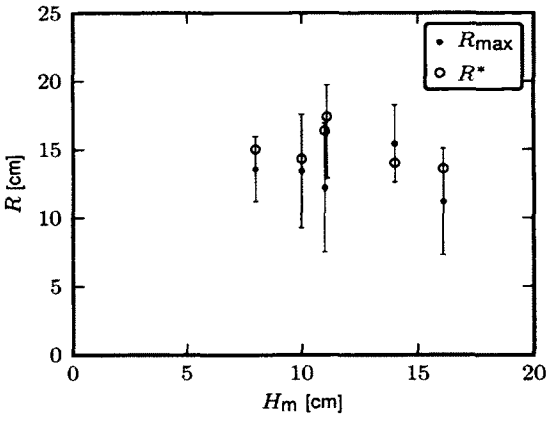

Figure 3.7: The distance from the edge of the cylindrical lock, R, plotted against the height of the mixed region, H_m. The measured stopping distance of the intrusion, $R_{\max}$, compared with the distance at which a mode-1 internal wave catches up with the front of the intrusion, R^*.

numerical simulation to examine the internal wave catching up with the front of the intrusion. The code, described by McMillan & Sutherland (2010) (Appendix B) solves the Navier-Stokes equations in cylindrical coordinates by approximating spatial derivatives with second order finite difference and time stepping with the leapfrog method. At the free-slip boundaries the no normal flow condition is imposed.

Figure 3.8 shows six snapshots taken over two buoyancy periods of a simulation that was initialized with the same parameters as the experiment shown in Figure 3.5. At $t = 1.6$s the black arrows highlight the motion of the return flow which sets the amplitude of the internal wave at the depth of the intrusion. In the subsequent images the black arrows indicate the motion of the internal wave launched by the return flow and which catches up to and stops the advance of the intrusion head. The time at which the wave arrives at the front of the intrusion appears to coincide with the intrusion reaching its maximum radius of propagation.

3.3.2 The Effects of Rotation

The qualitative nature of the collapse was noticeably different in the rotating experiments. For all experiments with significant rotation, after the initial "slumping phase," which occurred relatively quickly, the intrusion propagated

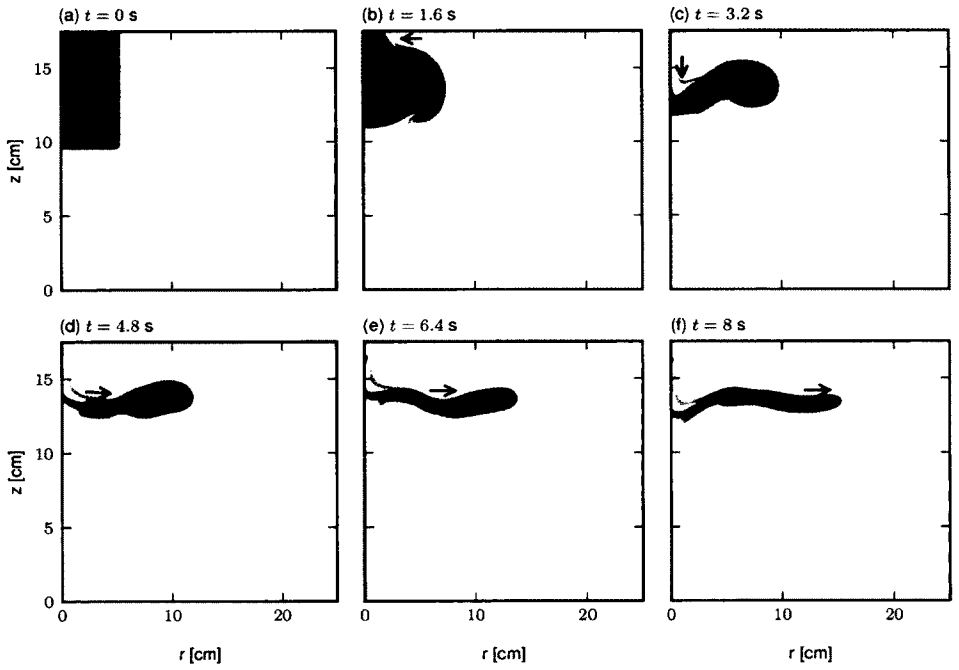

Figure 3.8: Cross-section of a passive tracer field constructed from a numerical model of the experiments in Figure 3.5. The grayscale represents the concentration and black arrows highlight the formation and subsequent motion of the interfacial wave.

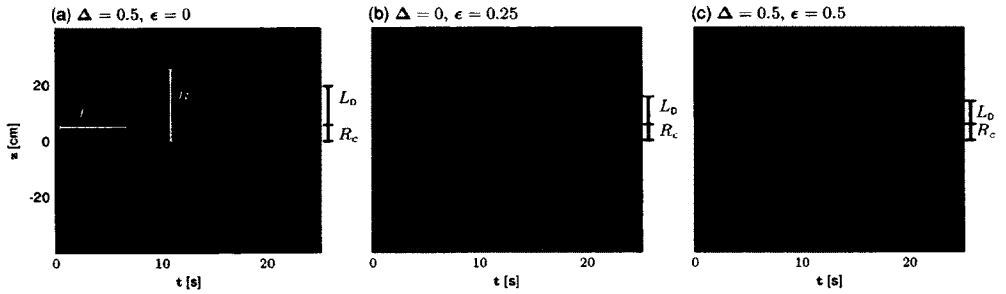

Figure 3.9: Time series taken from rotating experiments in a two-layer fluid with $\Omega = 0.2\,\mathrm{s}^{-1}$, $H = 10\,\mathrm{cm}$, $R_c = 6\,\mathrm{cm}$ and (a) $H_L = 2.5\,\mathrm{cm}$, $\rho_L = 1.0254\,\mathrm{g/cm}^3$, $\rho_C = 1.0186\,\mathrm{g/cm}^3$ (b) $H_L = 5\,\mathrm{cm}$, $\rho_L = 1.0254\,\mathrm{g/cm}^3$, $\rho_C = 1.0186\,\mathrm{g/cm}^3$, (c) $H_L = 2.5\,\mathrm{cm}$, $\rho_L = 1.0254\,\mathrm{g/cm}^3$, $\rho_C = 1.0050\,\mathrm{g/cm}^3$. In (a) the oscillatory period, T_p, measured as the time between the first and second outward pulse and the maximum radius of propagation, R_{max} are shown.

out at near-constant speed, rapidly decelerated and, unlike non-rotating cases, reversed directions.

Time series taken from typical two-layer rotating experiments are shown in Figure 3.9. The experimental parameters were chosen to be similar to those of the non-rotating experiments in Figure 3.3. For each plot, the Rossby deformation radius L_D and the radius of the cylinder R_c is indicated on the right hand side.

Figures 3.9(a) and 3.9(b) show experiments where either $\epsilon = 0$ or $\Delta = 0$. Unlike the non-rotating equivalents shown in Figure 3.3, the rotating intrusion did not impact the side wall of the tank. Instead, the direction of flow reversed abruptly. In the cases for which ϵ and Δ were both non-zero (Figure 3.9(c)) a longer period of deceleration was apparent from the time-series.

The two-layer experiments explored moderate values of the Rossby number ($\mathrm{Ro} \gtrsim 1$) so that the intrusion propagated outward at near-constant speed for a measurable distance before being affected significantly by rotation. Accordingly, rotation was not expected to influence the initial speed of the intrusion.

The measured speeds are plotted against $U_{2\mathrm{L}}$ in Figure 3.10. The dashed line, $U = U_{2\mathrm{L}}$, shows that rectilinear theory over-predicts the speed of the intrusions. A best-fit line passing through the origin gives $U = (0.68 \pm 0.03) U_{2\mathrm{L}}$ (RMSE: ± 0.33), comparable to that measured for non-rotating cases.

The distance, R_{max}, over which the intrusion propagated before the deceleration began and the flow changed direction is illustrated by white vertical bars in Figure 3.9(a); it is the radial distance traversed by the intrusion from

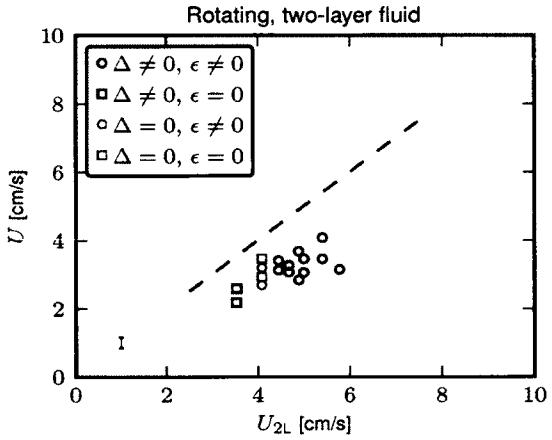

Figure 3.10: For the two-layer rotating experiments, the measured speeds U are plotted against the theoretical speeds U_{2L} given by equation (3.4). Experiments were separated according to values of ϵ and Δ as shown in the legend. The line $U = U_{2L}$ is plotted and shows that for all cases the observed speeds were less than the predicted speeds. A characteristic vertical errorbar is shown in the lower left corner of the plot.

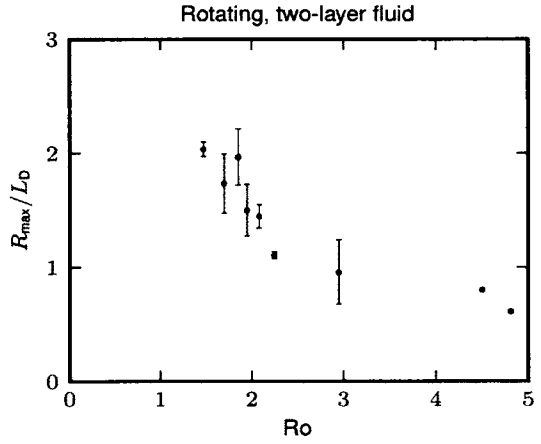

Figure 3.11: For the two-layer rotating experiments, the maximum distance propagated by the intrusion, R_{max}, (illustrated in figure 3.9) is normalized by the Rossby deformation radius, L_D given by equation (1.4) and plotted against the Rossby number given in equation (3.7).

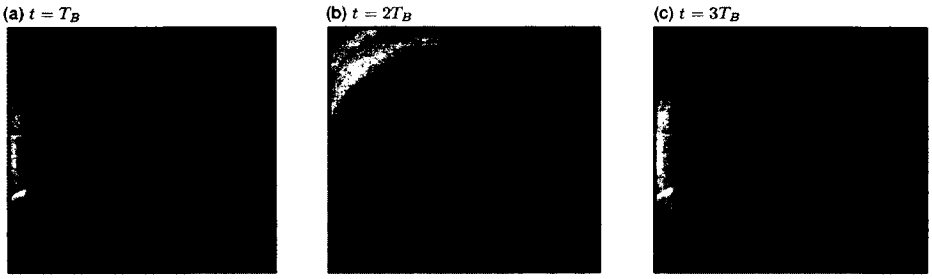

Figure 3.12: The top view of a rotating full-depth lock-release experiment in uniformly stratified fluid after (a) one, (b) two, and (c) three buoyancy periods. In this experiment $H = 17.5\,\mathrm{cm}$, $\Omega = 0.3\,\mathrm{s}^{-1}$, $N = 2.27\,\mathrm{s}^{-1}$

the inner edge of the cylindrical lock.

Figure 3.11 shows a non-dimensional plot of $R_{\max}/L_D$ against Ro. For $\mathrm{Ro} \gtrsim 2$, $R_{\max} \leq L_D$. However, for $\mathrm{Ro} < 2$ we found that $1 \leq R_{\max}/L_D \leq 2$. This is a smaller ratio than that observed for gravity currents propagating beneath uniform ambient (Hallworth *et al.*, 2001)

Visually tracking the concentration of dye in Figure 3.9 revealed regular pulsations of the intruding fluid. The dye initially concentrated in the lock moved outward after the release of the lock becoming less concentrated before reaching $R_{\max}$. Then the dye appeared to collect near the centre of the tank once more and the second outward pulsation began.

The front of this second pulsation moved outward toward $R_{\max}$ at near-constant speed, often overshooting $R_{\max}$ by a short distance. The pulsations continued as the patch adjusted to the steady state. But the dye lines gradually blurred and became more difficult to track.

The intrusion behaved in a qualitatively similar manner to a gravity current. The lens-shaped bulk of fluid expanded and contracted as it released outwardly propagating pulses. By averaging over the time between successive pulses Hallworth *et al.* (2001) found $\omega = 1.05f$.

The time from the beginning of the experiment to the first outward pulse T_p is illustrated in Figure 3.9(a). In experiments for which T_p could be measured the corresponding frequency $\omega_p = 2\pi/T_p$ was found to increase as the rotation rate of the fluid increased so that $\omega_p = 2.8f$, significantly higher than that observed for bottom propagating currents.

In the uniformly stratified experiments, the adjusting patch formed a lens-shaped structure that alternatively expanded and contracted vertically and

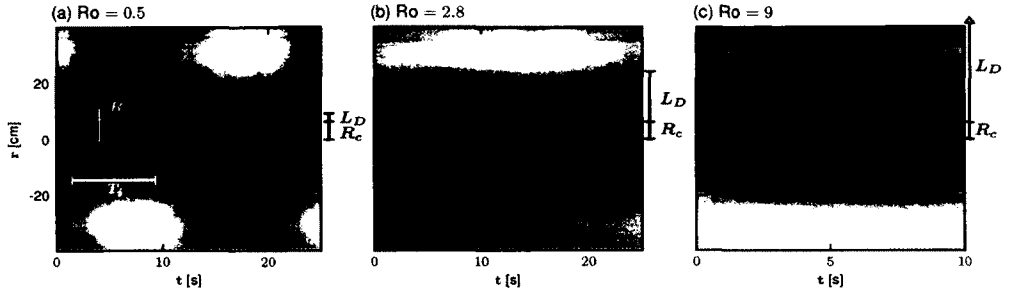

Figure 3.13: Time series taken from rotating experiments in continuously stratified fluid for increasing magnitudes of the Rossby number $\mathrm{Ro} = L_D/R_c$ with $N \simeq 1.5\,\mathrm{s}^{-1}$, $R_c \simeq 5\,\mathrm{cm}$ (a) $H_m = 7.5\,\mathrm{cm}$, $\Omega = 0.3\,\mathrm{s}^{-1}$ (b) $H_m = 12.7\,\mathrm{cm}$, $\Omega = 0.1\,\mathrm{s}^{-1}$ and (c) $H_m = 14.9\,\mathrm{cm}$, $\Omega = 0.03\,\mathrm{s}^{-1}$. The oscillatory period T_i is illustrated in (a) and is measured as the time between the beginning of first and second expansion.

horizontally. The top views shown in Figure 3.12 were taken from a full-depth lock-release experiment. In Figure 3.12(a) one buoyancy period had passed and the intrusion front advanced in spokes. After two buoyancy periods (Figure 3.12(b)) the finger-like tendrils at the leading edge wrapped around the patch as it contracted anticyclonically to form an outer spiral structure. After three buoyancy periods (Figure 3.12(c)) the lens had expanded again and over longer times was observed to oscillate laterally as the lens rotated anticyclonically.

Particles that were placed on the surface of the lock-fluid at the start of the experiment revealed, as expected, that the ambient above the collapsed mixed layer rotated cyclonically.

Figure 3.13 shows radial time series for three experiments with increasing values of the Rossby number. The intrusions propagated out radially at near-constant speed for about one buoyancy period. Compared with the non-rotating experiments (*e.g.* see Figure 3.5) the initial near-constant speed phase lasted for a shorter time and the intrusion traversed a shorter radial distance.

Figure 3.14 shows the measured speeds plotted against the theoretical rectilinear speeds as defined in equation (3.6). The dashed line, $U = U_{\mathrm{NP}}$, shows that the theory over-predicted the speeds. Consistent with the non-rotating case, $U = (0.68 \pm 0.04)U_{\mathrm{NP}}$ (RMSE ± 0.16). Dominated by inertial forces, rotation did not effect the intrusion speed during the initial collapse phase.

In the absence of rotation we saw that the advance of an asymmetric intrusion stopped as a consequence of interactions with internal waves. Rotation additionally influenced the stopping distance for small Rossby numbers

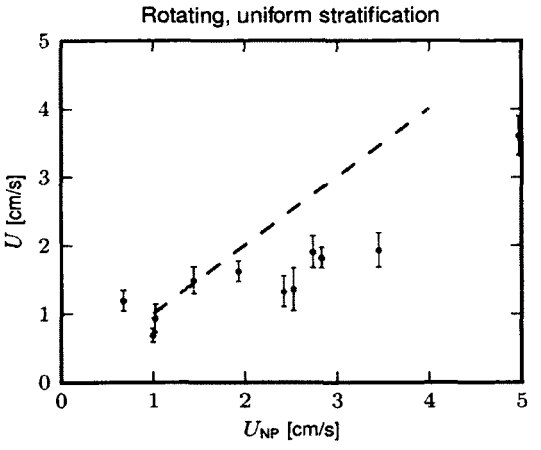

Figure 3.14: For the rotating uniformly stratified experiments the measured speeds U are plotted against the speeds predicted by equation (3.6). The line $U = U_{\text{NP}}$ is plotted and shows that for all cases the measured speed was less than the predicted speed.

(Ro < 1); in some cases, stopping at distances less than one lock-radius.

The time series shown in Figure 3.13 compares the stopping distance, $R_{\max}$, to the Rossby deformation radius, L_D. The radius of the cylinder, R_c, is indicated on the right hand side. For Ro $= 0.5$ (Figure 3.13(a)) a relatively short period of near-constant speed was observed. When Ro $= 2.8$ (Figure 3.13(b)) the near-constant speed phase lasted longer. The time series clearly shows the oscillatory motion of the patch as it geostrophically adjusts. Increasing the Rossby number even further to Ro $= 9$ (Figure 3.13(c)) resulted in an intrusion that behaved more similarly to the non-rotating case. The deformation radius extended beyond the radius of the tank and so the intrusion stopped moving well before the Coriolis effect could impact its motion.

For the range of Rossby numbers tested in our experiments $R_{\max}$ was between $0.7R_c$ and $3R_c$. The relationship between $R_{\max}/L_D$ and Ro is shown in Figure 3.15. For Ro $\lesssim 1$, $R_{\max}/L_D \in (1, 3)$. The intrusions overshot the equilibrium position as it geostrophically adjusted. In agreement with Stuart *et al.* (2011) the graph shows that the maximum radius of propagation scaled with the Rossby deformation radius for small Rossby numbers (Ro > 1). For values of Ro $\gtrsim 2$ the predicted deformation radius was much larger than the recorded stopping distance since $L_D \to \infty$ as $f \to 0$.

The counter-rotation of the intrusion can limit $R_{\max}$ (Ungarish & Huppert,

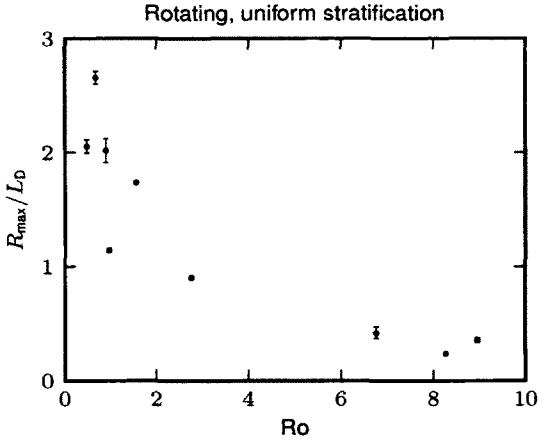

Figure 3.15: For the continuously stratified rotating experiments, the maximum distance traversed by the intrusion, $R_{\max}$, (illustrated in figure 3.13) is normalized by the Rossby deformation radius, given by equation (1.4), and plotted against the Rossby number, defined by equation (3.7).

2004), but the associated theory for an axisymmetric intrusion (Ungarish, 2009) which does not account for the influence of internal waves, over-predicted the stopping distance by a significant factor even for experiments with large Rossby numbers. The stopping distances were more accurately predicted by considering direct interactions of the intrusion with internal waves (Munroe *et al.*, 2009).

The top views in Figure 3.12 and the time series in Figure 3.13 clearly demonstrate the oscillatory behaviour of the patch. These oscillations create a wave-like pattern in the time series. The time to the first trough, T_i, (shown in Figure 3.13(a)) decreased as the frequency of rotation increased.

The experiment shown in Figure 3.13(b) has a comparable Rossby number to the two-layer experiments shown in Figure 3.9. In the two-layer experiments the patch pulsated in a series of outward bursts, while in the uniformly stratified experiments the oscillations were relatively smooth and the second dilation of the patch was much shorter.

3.4 Discussion and Conclusions

The initial speeds of intrusions generated by the collapse of a uniform density patch in stratified fluid were found to be 65-70% of those predicted by recti-

linear theory. In both two-layer and uniformly stratified fluids rotation had no significant influence on the speed of the intrusions during the initial stage of collapse for both types of stratifications.

In no experiments did we observe the characteristic features of the self-similar regime predicted for and observed in bottom propagating gravity current experiments. In the non-rotating two-layer experiments the intrusion propagated at constant speed beyond $7R_c$ if $\epsilon = 0$. For experiments with $\epsilon \neq 0$, as a result of breaking vertical symmetry a mode-1 interfacial wave was efficiently excited by the return flow into the lock. This caught up with the propagating intrusion, stalling or even halting its advance. In all the uniformly stratified experiments the intrusion, which propagated more slowly than both mode-1 and mode-2 internal waves, stopped abruptly without reaching the tank wall. In vertically symmetric cases the intrusion halted by losing energy to the mode-2 wave that moved ahead of it. In asymmetric cases, just as in the two-layer cases, the return flow dominantly excited a mode-1 wave that was responsible for its relatively short stopping distance.

Rotation further limited the maximum propagation distance of the intrusions. Stopping distances were shorter for the rotating experiments as compared to the non-rotating cases for small Rossby numbers (Ro < 1). The stopping distance of the intrusion was a maximum of three times the Rossby deformation radius which is smaller than that observed for bottom propagating gravity currents (Hallworth *et al.*, 2001). For larger Rossby numbers the deformation radius extended beyond the radius of the tank and the stopping distance of the intrusion was influenced by interactions with the generated internal waves.

In the two-layer rotating experiments the patch periodically exhibited outward pulsations. Whereas, in the continuously stratified case the adjusting lens oscillated more smoothly about an equilibrium radius. The frequency of the oscillation of the patch increased as the rotation rate increased, but the frequency was difficult to measure accurately.

Due to restrictions of the experimental setup, this study focused upon intrusions released from locks with aspect ratios $R_c/H_m \lesssim 1$. In simulations not reported upon here it was found that the intrusion speed increased with R_c/H_m, asymptoting for $R_c/H_m \gtrsim 2$ to constant values consistent with those observed in rectilinear geometries. It is anticipated that gravity currents and intrusions emanating from locks of sufficiently large radius should initially have the speed of rectilinear intrusions; the small curvature of such locks should not

influence the evolution of the slumping fluid as it approaches steady state. It is surprising that intrusions emanating from locks with aspect ratios of order unity should propagate at constant speed for distances longer than $7R_c$. The generation of internal waves and subsequent interactions must play a role in establishing the steady state speed. However existing theories are not readily adapted to capture these dynamics: Benjamin's theory assumes steady state from the outset and so ignores wave generation and transience associated with the collapse of a cylindrical patch of fluid; shallow water theory ignores effects associated with the generation and evolution of large amplitude, non-hydrostatic waves. Clearly more work remains to be done in theory and experiment.

Chapter 4

The Axisymmetric Collapse of a Mixed Patch and Internal Wave Generation in Uniformly Stratified Rotating Fluid

4.1 Introduction

In this chapter, the axisymmetric experiments presented in Chapter 3 investigating mixed region collapse are reconsidered, but with the fluid in solid body rotation. Numerical simulations are also performed. Like the non-rotating case, the collapse excited downward propagating internal waves that have the potential for mixing in the abyss. We are particularly interested in estimating the energy transport due to these waves. So the conical wavefield was analyzed with synthetic Schlieren to determine the frequency, radial wavenumber, and the maximum vertical displacement due to the waves.

After verifying that the numerical model could reproduce the experimental data, we performed a series of simulations that extended the parameter range to those more relevant to the ocean. Specifically, we examined how the aspect ratio of the lock changed the dynamics of collapse and its affect on the energy transport by internal waves. Independently, for a fixed lock aspect ratio, we explored the dependence of the collapse on the Rossby number.

Our investigation of downward propagating internal waves in uniformly stratified rotating fluid leads to several formulae that describe the relationship between the initial conditions and the properties of the waves. These formulae are then used to make an order-of-magnitude estimate of the power input from a moving hurricane to the internal wave field through the collapse of the mixed

region it generates.

The experimental setup, numerical model and analysis techniques are described in section 4.2. The results for both the experiments and the numerical model are presented in section 4.3. Finally, we extend our results to oceanic scales and conclude in section 4.4.

4.2 Set-up and Analyses

4.2.1 Experimental Setup and Analysis Methods

Experiments were performed on a Geophysical Fluids Rotating Table (Australian Scientific Instruments). We used a square tank (measuring $L = 50\,\mathrm{cm}$ on each side) for best results from the synthetic Schlieren analysis technique. The experimental setup is shown in Figure 4.1. A Schlieren image screen of black and white horizontal lines was attached to the back of the tank and illuminated by a fluorescent-light-sheet secured directly behind it.

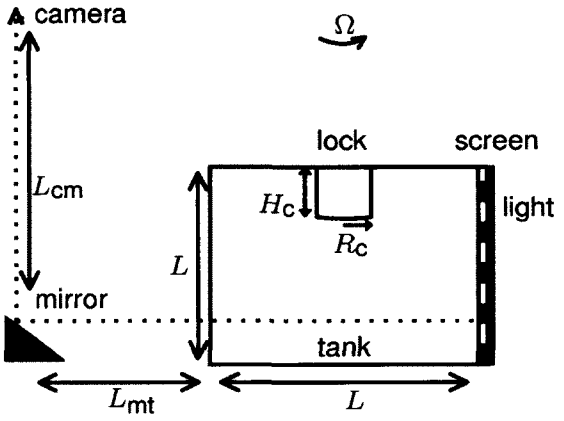

Figure 4.1: Schematic diagram of the experimental apparatus situated on a rotating table. A mirror was a distance of L_{mt} from the tank and L_{cm} below the camera. A cylindrical lock of radius R_c was inserted to a partial-depth H_c in the square tank ($L = 50\,\mathrm{cm}$).

The method of synthetic Schlieren was described in Chapter 2. It is the same method used by Holdsworth *et al.* (2010) to derive the change in the squared buoyancy frequency due to the waves $\Delta N^2(r, z, t) = -(g/\rho_0)\partial_z \rho$ and

its time derivative, N_t^2. The details of this method were described in section 2.2 and are illustrated by Figure 2.3.

Three experiments were performed using the same experimental apparatus shown in Figure (4.1) but with the image screen replaced by a random pattern of dots. These experiments verified that the wave characteristics determined by synthetic Schlieren were not biased by using an image screen of horizontal lines.

The videos of distortions of random dot images were analyzed using open-source software for advanced imaging velocimetry called "uvmat". The software implemented a method called Correlation Image Velocimetry (CIV) that relies on direct cross-correlations between image pairs of pattern boxes to track particles . Like synthetic Schlieren with lines, CIV involves tracking apparent displacements of the image screen. However, CIV measures horizontal as well as vertical displacement. A series of image correlations were performed for each pair of frames to track the movement of the dots. Thus, intrusion front velocities were determined by finding particle displacements between images $\Delta t = 0.067\,\mathrm{s}$ apart. In practice, however, using the screen of dots resulted in a noisier N_t^2 field than the screen of horizontal lines which made measurements of the amplitude difficult. Therefore, with the exception of three experiments from which ω and k_r were determined, the rotating experiments presented here were analyzed with synthetic Schlieren using horizontal lines.

To ensure the Sony DCR-TRV6 CCD camera was far enough away that it received a nearly parallel distribution of light passing through the tank, it was mounted above and to one side of the tank pointing downward toward a mirror angled 45 degrees from the horizontal. The light travelled a total distance of $L_{cm} + L_{mt} = 165\,\mathrm{cm}$ from the near-side of the tank to the camera lens after reflecting off the mirror (see Figure 4.1).

The "Double-Bucket" technique (Oster, 1965) was used to fill the tank with linearly stratified fluid to a total depth of $H \simeq 40\,\mathrm{cm}$. Before filling the tank the water in the buckets was allowed to reach room-temperature to prevent any vertical temperature gradients from interfering with the experiment. Point measurements of the density were used to construct a vertical density profile of the ambient $\bar{\rho}$ from which the constant buoyancy frequency $N = \sqrt{(-g/\rho_0)(\partial_z \bar{\rho})}$ was found. For all the rotating experiments presented here, N ranged from $N = 1.57\,\mathrm{s}^{-1}$ to $1.77\,\mathrm{s}^{-1}$.

A hollow acrylic cylinder of radius $R_c = 5.3\,\mathrm{cm}$ was suspended above the centre of the tank and extended down from the surface of the fluid to a partial-

depth of H_c between 5.2 cm and 15 cm. The fluid within the cylindrical lock was then mixed with an oscillating mechanical stirrer until the density was uniform to a depth H_m, moderately smaller than H_c. We added a small amount of dye to the lock to visualize the intrusion, but it did not significantly affect the density of the lock-fluid. Density measurements of the lock-fluid, ρ_L, were recorded and used to verify the depth of neutral buoyancy below the surface, $H_m/2$.

Over a period typically lasting 12 hours or more the entire system was then allowed to "spin-up" so that the ambient and lock-fluid were co-rotating at a constant rate Ω in the counter-clockwise direction. When the table began rotating turbulence was expected within the tank especially near the corners; if the magnitude of spin-up was too large then the stratification could become non-linear.

Several test experiments were performed in which the stratification was measured before and after spin-up to ensure that the linear stratification was not significantly altered by the spin-up process. Different coloured dye was added layer by layer while the tank was filling. Once filled, the water in the tank appeared as a column of evenly spaced horizontal dye-lines. When rotation was initiated isopycnal surfaces were disturbed and turbulent mixing began in the tank corners. From the top view, the dye was observed to spin into five distinct vortices: one larger vortex in the centre and four smaller ones in each of the corners. After 12 hours, the dye lines had blurred, but the individual dye-lines were still easy to distinguish. Point measurements of the density were taken at a range of vertical positions to determine N before and after the spin-up, confirming that the density stratification was negligibly affected by spin-up.

Rotations rates varied from $0.03\,\mathrm{s}^{-1}$ to $0.45\,\mathrm{s}^{-1}$. Accordingly, the Rossby numbers, defined by $\mathrm{Ro} = U/fR_c$ with $U = \frac{1}{8}NH_m$ being the predicted speed of a rectilinear intrusion (see fig. 3.6), ranged from $\mathrm{Ro} = 0.3$ to $\mathrm{Ro} = 5.6$.

An experiment began after the fluid in the tank reached solid body rotation. The cylindrical lock was rapidly extracted vertically releasing the lock-fluid into the ambient. The camera recorded a side view of the experiment and its impact on the ambient.

An example of a rotating experiment is shown in Figure 4.2 at times $2T_b$ and $3T_b$ after the cylinder was extracted, where $T_b = 2\pi/N$ is the buoyancy period. The Schlieren image screen of black and white lines is visible in the background of each image and visual markers (small black dots) placed at the

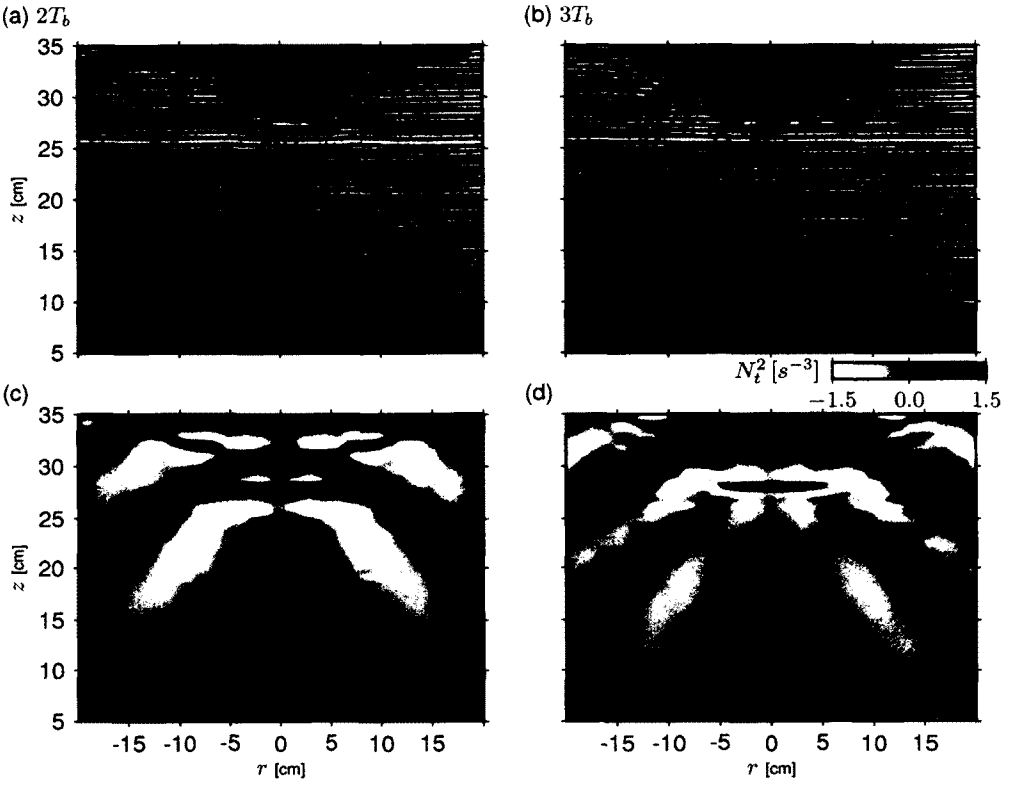

Figure 4.2: Side view of the tank after (a) $2T_b$ and (b) $3T_b$. Below each image the N_t^2 field the corresponding N_t^2 field is shown ((c), and (d)). The experimental parameters are $N = 1.77\,\mathrm{s}^{-1}$, $H = 40.6\,\mathrm{cm}$, $H_m = 14\,\mathrm{cm}$, $f = 0.502\,\mathrm{s}^{-1}$. Note: the surface is situated 5.6 cm above the top of the frames shown.

near and far side of the tank were used to set the world coordinates at the mid-point of the tank. The column of mixed fluid collapsed vertically forming an intrusion at the depth where it was neutrally buoyant, approximately $H_m/2$ below the surface. Like the non-rotating experiments, immediately after the experiment began the lock-fluid thinned as it spread radially (Figure 4.2 (a)). But, instead of halting due to interactions with internal waves, the intrusion reversed directions wrapping anti-cyclonically into a lens-shaped vortex (Holdsworth *et al.*, 2012*a*). As the patch contracted radially it was observed to thicken (Figure 4.2 (b)). This process repeated periodically until equilibrium was reached.

Taking the time derivative of the ΔN^2 field has the advantage of filtering slowly evolving perturbations excited during the initial collapse and enhancing

changes due to internal waves which occur over relatively fast time-scales. Figure 4.2 shows an example of the N_t^2 field computed from successive frames $\Delta t = 0.03$s apart after (c) $2T_b$ and (d) $3T_b$. Since the experiments were assumed to be azimuthally symmetric, the N_t^2 field was found for $r \geq 0$ and reflected about $z = 0$ to obtain the full field as shown in the figure.

Reynolds numbers for the intrusion, defined by $\mathrm{Re} = NH_m^2/\nu$, ranged from 3.3×10^3 to 4.4×10^4. Instead using a wave-based time-scale of $T = \omega^{-1}$ and a characteristic length scale of $L = k_r^{-1}$ the Reynolds number for the internal waves ranged from 1.2×10^2 to 6.3×10^2. For Re this large, viscosity did not play a significant role in the evolution of the flow over the relatively short time scales during which the waves were analyzed.

4.2.2 Theory and Analysis

In most of our analyses of the internal waves, we examined radial time series of the N_t^2 field, which was measured directly by synthetic Schlieren. This field is related to all other quantities of interest through the polarization relations for axisymmetric internal waves listed in Table 4.1 that were derived from the Navier-stokes equations given by (4.7).

In particular, the downward propagating internal waves were measured and analyzed from the N_t^2 field at a fixed vertical level z just below the mixed region. From a radial time series, N_t^2 is Fourier-Bessel decomposed according to

$$N_t^2(r,t) = \sum_{n=0}^{N} \sum_{m=0}^{M} A_{N_t^2}(k_n, \omega_m) J_0(k_n r) e^{-i\omega_m t}. \tag{4.1}$$

in which it is understood that the actual field is real part of the right-hand side expression. The radial wavenumber $k_n = \alpha_n/R$ is given in terms of the zeroes α_n of $J_0(r)$ and the tank half-width $R = L/2$. The corresponding frequency is $\omega_m = (2\pi/T)m$ where T is the duration of the time series. For each $k_r = k_n$ and $\omega = \omega_m$, the vertical wavenumber, k_z, can be deduced from the dispersion relation

$$\begin{aligned} \omega^2 =& N^2 \frac{k_r^2}{k_r^2 + k_z^2} + f^2 \frac{k_z^2}{k_r^2 + k_z^2} \\ =& N^2 \cos^2\theta + f^2 \sin^2\theta, \end{aligned} \tag{4.2}$$

where the angle θ of constant-phase lines to the vertical is given in terms of

Structure	Relation to A_ξ
$\xi = \frac{1}{2}A_\xi J_0(k_r r)e^{i(k_z z-\omega t)} + cc$	
$\psi = \frac{1}{2}A_\psi J_1(k_r r)e^{i(k_z z-\omega t)} + cc$	$A_\psi = -i\frac{\omega}{k_r}A_\xi$
$N_t^2 = \frac{1}{2}A_{N_t^2} J_0(k_r r)e^{i(k_z z-\omega t)} + cc$	$A_{N_t^2} = -k_z\omega N^2 A_\xi$
$w = \frac{1}{2}A_w J_0(k_r r)e^{i(k_z z-\omega t)} + cc$	$A_w = -i\omega A_\xi$
$v = \frac{1}{2}A_v J_1(k_r r)e^{i(k_z z-\omega t)} + cc$	$A_v = -f\frac{k_z}{k_r}A_\xi$
$p = \frac{1}{2}A_p J_0(k_r r)e^{i(k_z z-\omega t)} + cc$	$A_p = i\rho_0\frac{\omega^2 k_z}{k_r^2}A_\xi$

Table 4.1: Polarization relations for the vertical displacement (ξ), streamfunction (ψ), time change in the perturbed squared buoyancy field (N_t^2), vertical velocity (w), radial velocity (u_r), and pressure fields (p). The vertical wavenumber is given by $k_z = k_r\sqrt{\frac{N^2-\omega^2}{\omega^2-f^2}}$. Here cc denotes the complex conjugate.

ω, N, and f by

$$\theta = \frac{1}{2}\cos^{-1}\left(\frac{2\omega^2-(N^2+f^2)}{N^2-f^2}\right). \tag{4.3}$$

As the collapse of the mixed region began, columnar undulations formed directly beneath the lock-fluid. In the absence of rotation, potential energy was rapidly converted to kinetic energy and the columnar motion decayed quickly. However, in solid body rotation the columnar motion persisted as the mixed region repeatedly expanded and contracted while undergoing geostrophic adjustment.

Figure 4.3 (b) shows the normalized radial times series extracted from the N_t^2 field for the experiment shown in Figure 4.2. For comparison, a normalized radial time series taken from a non-rotating experiment with similar initial conditions is shown with the same color-scale in Figure 4.3 (a). Ignoring the discrepancies duc to image resolution, there are obvious qualitative difference between the figures. In both cases, the highest amplitudes occurred near $r = 0$. Because the phase lines are nearly horizontal directly beneath the collapsing

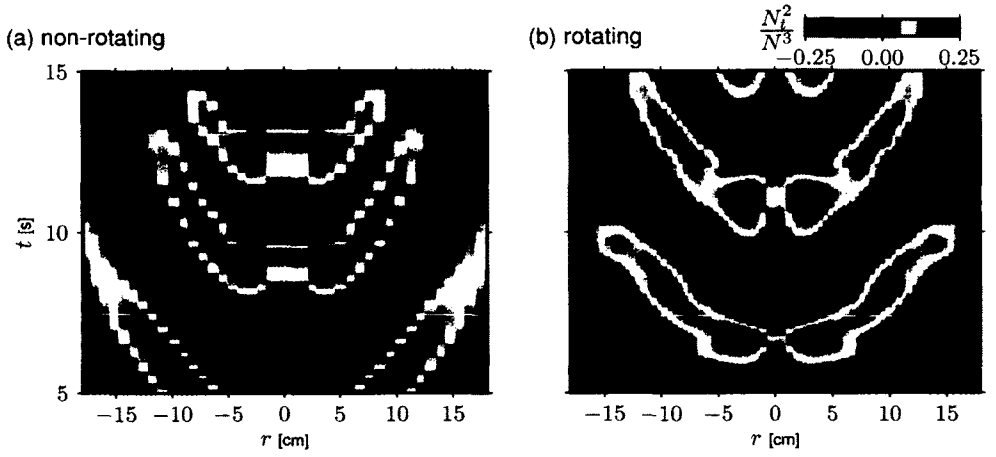

Figure 4.3: Radial times series of the N_t^2 field normalized by N^3 for an experiment from the non-rotating study Holdsworth *et al.* (2010) with (a) $N = 1.53\,\mathrm{s}^{-1}$, $H = 45\,\mathrm{cm}$, $H_m = 14\,\mathrm{cm}$, and (b) rotating experiment with similar parameters $N = 1.77\,\mathrm{s}^{-1}$, $H = 40.6\,\mathrm{cm}$, $H_m = 14\,\mathrm{cm}$, $f = 0.502\,\mathrm{s}^{-1}$.

patch, the region directly beneath the former location of the cylindrical lock was excluded from our analysis of the wave properties.

Wave characteristics were determined by averaging results measured from the radial time series over three heights at $z_0 - \Delta z$, z_0, and $z_0 + \Delta z$ where z_0 is taken between 5 and 15 cm below the mixed region and $\Delta z = 0.18\,\mathrm{cm}$. At each of the heights the N_t^2 field was truncated from T_1 (when the internal waves were just starting to pass through that height), over an integer number of buoyancy periods to $T_2 = T_1 + n_* T_b$. For the experiments, the extraction of the cylinder caused the entire experimental apparatus to vibrate for a few seconds after the release of the cylinder. To avoid measuring these vibrations we chose $T_1 = 2T_b$. After about 30 s, the internal waves began reflecting off the side walls leaving a narrow window of time in which to measure the waves. For this reason, we chose $n_* = 2$.

Wave frequencies were determined from radial and vertical time series using the same technique used by Holdsworth *et al.* (2010); a detailed description is presented in Chapter 2. At a fixed r, the Fourier transform was applied to the N_t^2 field and a parabola was fit to the power of three frequencies about the peak. The location of the maximum of the resulting parabola was taken to be the central frequency, ω_*. Averaging central frequencies determined from all radial and vertical time series resulted in a single characteristic frequency, $\overline{\omega}_*$.

The standard deviation provided an estimate of the error.

Radial wavenumbers are defined by $k_r = 2\pi/\lambda_r$, where λ_r is the radial wavelength. As described in Appendix C, radial wavelengths were estimated by applying the continuous wavelet transform to radial time series of the N_t^2 field

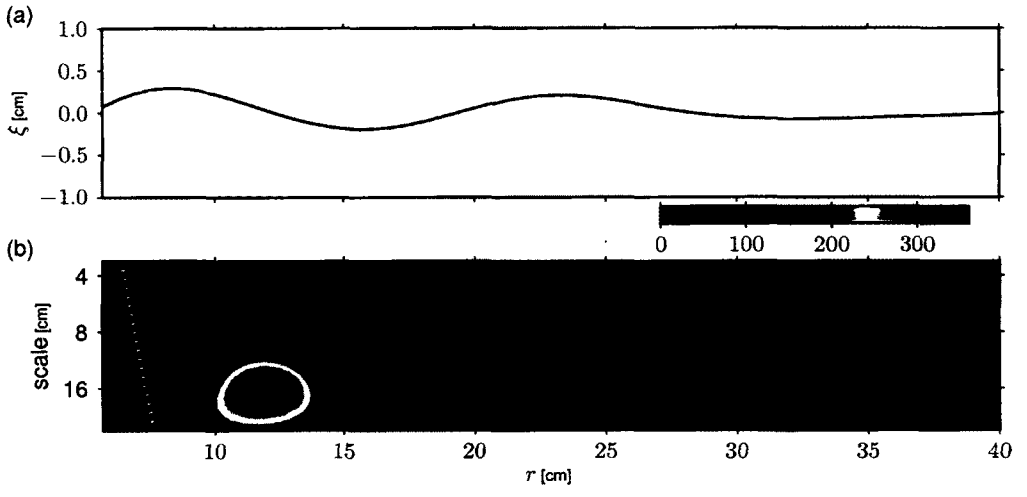

Figure 4.4: (a) The amplitude of a radial slice of ξ at $z_* = H - H_m - 5\,\text{cm}$ and $t_* = T_b$ for a simulation with the same parameters as the experiment shown in Figure 4.2. The solid line was taken directly from the N_t^2 field $\simeq 5\,\text{cm}$ below the mixed region. (b) The corresponding wavelet power spectrum computed using the DOG 3 wavelet. The dotted white line represents the cone of influence and the left side of the r-axis is $\simeq R_c$. Values of the Power spectrum are indicated by the colour bar on an arbitrary scale.

Figure 4.4(a) shows a radial slice of N_t^2 for the same experiment shown in Figure 4.3 (b) (excluding $r \leq R_c$). The data was normalized by subtracting the mean and dividing by the standard deviation before applying the wavelet transform. Figure 4.4(b) shows the corresponding wavelet power spectrum as a function of r and the Fourier scale. The colour contours represent the magnitude of the power spectrum.

Oscillations of the signal generate wavelet coefficients of large magnitude. In the wavelet power spectrum, the largest coefficients are generated at Fourier scales peaking at a characteristic λ_r. Therefore, the characteristic radial wavelength was determined by finding the Fourier scale with the highest magnitude coefficients. For the example in Figure 4.4(b), the highest magnitude coefficients were generated at a scale where $\lambda_r \simeq 17\,\text{cm}$ which implies $k_* \simeq 0.37\,\text{cm}^{-1}$.

To improve accuracy in the calculation of k_* the radial series was padded with zeros before transforming. The drawback of this process is that it introduces discontinuities at the edge of the spectrum. The perimeter of the affected region is drawn as a white dotted line in 4.4(b) and within the contours of this perimeter, known as the cone of influence, edge effects are considered negligible. Note that only a small portion of the parabolic contour known as the the cone of influence is visible here and that it is the region to the right of the dashed line which is not influence by edge effects.

Radial time series were extracted at a series of times t_* taken every $T_b/8$ over n_*T_b. To obtain a single characteristic value of the radial wavenumber for each experiment $\overline{k}_*$, we averaged over all of these times and three heights.

The vertical displacement field, ξ, was derived from the N_t^2 field using the relationship between A_ξ and $A_{N_t^2}$ given by the polarization relations in Table 4.1. At a fixed vertical level

$$\xi(r,t) = \sum_{n=0}^{N}\sum_{m=0}^{M} \frac{-A_{N_t^2}(k_n,\omega_m)}{k_n N^2\sqrt{N^2-\omega_m^2}} J_0(k_n r)e^{-i\omega_m t}. \tag{4.4}$$

When the mixed region collapsed at the centre of the tank it generated waves that decreased in amplitude as they propagated down and away from the centre. Consequently, the maximum vertical displacement occurred near, but not necessarily at $r = 0$. In solid body rotation, large amplitude columnar motions directly beneath the lock-fluid obscured the pattern of waves. So the maximum displacement could not be measured directly.

Assuming the structure of the wave was modelled well by a Bessel function, $J(r) = AJ_0(k_r(r+r'))$, the maximum amplitude, A, was found by extrapolating from the best fit of $J(r)$ to a radial slice of $\xi(r)$ taken at a fixed z and t for $r \geq R_c$. The characteristic radial wavenumber $\overline{k}_*$ was used to form an initial approximation of the fit. Then, the signal was phase-shifted by r' and dilated by A until the approximation was within RMS error of 0.001 of the signal. Figure 4.5(a) shows an example of how the measured amplitude varies with radius. The solid line corresponds to the slice taken directly from the data for $r \geq R_c$ and the dashed line shows the corresponding fit Bessel function. The maximum value of $J(r)$ was found for each t_* and was averaged to obtain the characteristic value A_*. Finally, characteristic vertical displacement amplitudes, $|\overline{\xi}|_*$, were found for each experiment by averaging results from radial time series at different times.

The vertical flux of energy, $\mathcal{F}_E(z) = \int_0^{2\pi}\int_0^R wp\, r dr\, d\theta$, due to the internal

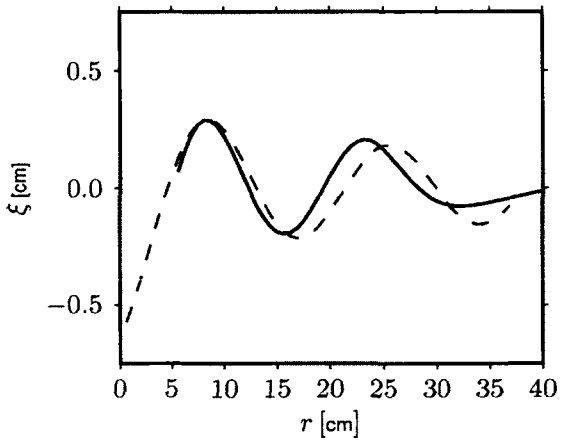

Figure 4.5: The amplitude of the vertical displacement field, ξ as a function of radius for a simulation with $N = 1.77\,\mathrm{s}^{-1}$, $H = 500\,\mathrm{cm}$, $H_m = 14\,\mathrm{cm}$, $f = 0.502\,\mathrm{s}^{-1}$. The solid line represents the radial series extracted from the data at $z = H - H_m - 5\,\mathrm{cm}$. The dashed line is the Bessel-fit of the data used to determine the maximum amplitude.

waves crossing a fixed horizontal level is transient during the process of collapse and re-stratification. So the flux of internal waves through a fixed level was measured and integrated over an integer number of wave periods $n_* T_w$, where $T_w = 2\pi/\overline{\omega}_*$, to obtain the energy as

$$\begin{aligned} E &= \int_{T_1}^{T_2} \mathcal{F}_E \, dt \qquad (4.5) \\ &= \frac{\pi}{8} \frac{R^2}{N^4} \rho_0 \sum_{n=0}^{N} \sum_{m=0}^{M} \frac{\omega_m^2 A_{N_t^2}^2(k_n, \omega_m) J_1(\alpha_n)^2 \, (T_2 - T_1)}{k_n^3 \sqrt{|N^2 - \omega_m^2|}}. \end{aligned}$$

In the analysis of the experiments, $T_1 = 2T_b$ and $T_2 = T_1 + 2T_w$. But, in general, $T_1 = n_1 T_b$ and $T_2 = T_1 + n_* T_w$ where n_1 and n_* are integers.

The wave period was used to truncate the N_t^2 field, but the calculation involved summing over all frequencies and wavenumbers of the Fourier-Bessel spectrum. Because of the transient nature of the waves, the integrated flux decreased with increasing depth below the mixed region. A conservative estimate of the energy flux was therefore taken to be the average value of $\mathcal{F}_E(z)$ over a 2 cm range.

For analysis purposes, the energy was normalized by the available potential energy as defined by equation (2.4), in which $\bar{\rho}_i$ and $\bar{\rho}_f$ are the initial and final density profiles, respectively. The initial density profile was taken to be linear

$\overline{\rho} = \rho_0(1 - \frac{N^2}{g}z)$. The final density profile was taken after the fluid in the cylindrical lock had been mixed and turbulence in the lock had dissipated:

$$\rho(z,r) = \begin{cases} \rho_L & |z| \geq H_m,\ |r| \leq R_c \\ \overline{\rho} & \text{otherwise.} \end{cases} \tag{4.6}$$

The calculation results in the same equation for the available potential energy given by equation (2.5).

4.2.3 Governing Equations and Numerical Model

The Navier-Stokes equations for small-amplitude, axisymmetric waves in a Boussinesq, incompressible and inviscid fluid on the f-plane are given in cylindrical coordinates by

$$\begin{aligned} \frac{\partial u}{\partial t} + u\frac{\partial u}{\partial r} + w\frac{\partial u}{\partial z} - \frac{v^2}{r} - fv &= -\frac{1}{\rho_0}\frac{\partial p}{\partial r} + \nu\left[\nabla^2 u - \frac{u}{r^2}\right] \\ \frac{\partial v}{\partial t} + u\frac{\partial v}{\partial r} + w\frac{\partial v}{\partial z} + \frac{uv}{r} + fu &= -\nu\left[\nabla^2 v + \frac{v}{r^2}\right] \\ \frac{\partial w}{\partial t} + u\frac{\partial w}{\partial r} + w\frac{\partial w}{\partial z} &= \frac{1}{\rho_0}\left[\frac{\partial p}{\partial z} - \rho g\right] + \nu\nabla^2 w \\ \frac{\partial \rho}{\partial t} + u\frac{\partial \rho}{\partial r} + w\frac{\partial \rho}{\partial z} + w\frac{\partial \overline{\rho}}{\partial z} &= \kappa\nabla^2\rho \\ \nabla\cdot\mathbf{u} = \frac{1}{r}\frac{\partial [ru]}{\partial r} + \frac{\partial w}{\partial z} &= 0 \end{aligned} \tag{4.7}$$

where $\mathbf{u} = (u_r, u_\theta, u_z) = (u, v, w)$, g is the gravitational acceleration, ρ_0 is the characteristic density, ν is the kinematic viscosity, κ is the diffusivity and $f = 2\Omega$ with Ω the background rotation. They describe the evolution of the flow and were used here to analyze and model the collapse.

The numerical model that solves these equations is the same as that used in previous studies of intrusive gravity currents (McMillan & Sutherland, 2010; Holdsworth *et al.*, 2012*a*), but here rotation is included. A more complete description of the model is given in Appendix B. Explicitly, the code replaces the momentum by the equation for azimuthal vorticity, $\zeta = \partial_z u - \partial_r w$:

$$\frac{\partial \zeta}{\partial t} = -ur\frac{\partial \zeta/r}{\partial r} - w\frac{\partial \zeta}{\partial z} - \nu\left[\nabla^2\zeta - \frac{\zeta}{r^2}\right] + \frac{1}{r}\frac{\partial [v^2 + fvr]}{\partial z}. \tag{4.8}$$

From the continuity equation for an incompressible fluid, one can define the streamfunction ψ so that $\mathbf{u} = \nabla \times (\psi\hat{\theta})$. Explicitly, the components of velocity are given by $u = -\partial_z\psi$ and $w = \frac{1}{r}\partial_r(r\psi)$. Thus, the streamfunction is

related implicitly to the azimuthal vorticity by

$$\nabla^2\psi - \frac{\psi}{r^2} = -\zeta. \tag{4.9}$$

The streamfunction is found from the azimuthal vorticity by inverting equation (4.9) in Fourier-Bessel space and then transforming back to real-space.

Equation (4.8) with the v-momentum and internal energy equation in (4.7) are used to advance ζ, v, ρ in time. The physical parameters are all taken to be constant with $g = 981\,\mathrm{cm/s^2}$, $\rho_0 = 1\,g/\mathrm{cm^3}$, and $\nu = 0.01\mathrm{cm^2/s}$. For salt water, the appropriate value of κ is around $10^{-5}\,\mathrm{cm^2/s}$. But, for numerical stability and efficiency, κ was taken to be $= 0.01\,\mathrm{cm^2/s}$. This value is small enough that it did not influence the relevant dynamics. The model was initialized using the perturbation density field given by equation (4.6) for a specified N, H_m and f.

The system of equations shown in equations (4.8) and (4.9) was discretized using a second-order finite-difference scheme in space with free-slip boundaries. The leap-frog scheme was used to advect the equations in time with an Euler back-step every 20 time steps. For visualization purposes, a passive tracer field was also advected in time. Unless otherwise specified, a square $500\,\mathrm{cm} \times 500\,\mathrm{cm}$ domain in (r, z) space was used with a time step of $\Delta t = 0.005\,\mathrm{s}$, $\Delta z = 0.48\,\mathrm{cm}$, $\Delta r = 0.31\,\mathrm{cm}$.

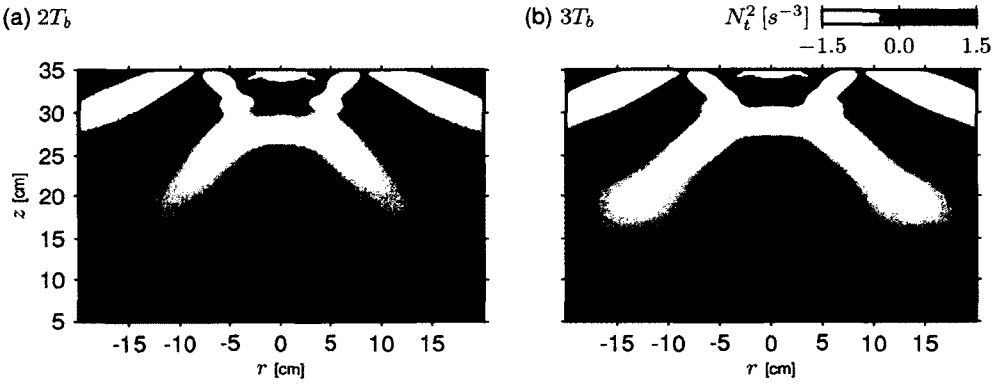

Figure 4.6: The N_t^2 field taken from direct numerical simulations at (a) $t = 2T_b$ and (b) $t = 3T_b$. This simulation was initialized with the same parameters as the experiment shown in Figure 4.2 and has the same grayscale.

For the experiment shown in Figure 4.2, the signal of internal waves was particularly strong compared to the background noise making it an optimal choice for qualitative comparisons with the numerical model. Figure 4.6 shows

the N_t^2 from the simulation after $2T_b$ and $3T_b$. In both cases, internal waves were generated beneath the collapsing region immediately after the extraction of the lock. These exhibit phase lines approximately fixed at a narrow range of angles to the vertical. Both Figures 4.2 and 4.6 have the same grayscale showing that the experimental and simulated wave amplitudes are also in approximate agreement. More rigorous quantitative comparisons between the experimental data and the numerical simulations will be made after a discussion of experimental results below.

4.3 Results

The simulations allowed for a larger range of initial conditions than were possible in the laboratory. Specifically, in Chapter 2 we found that the vertical displacement of the waves increased with the increasing depth of the mixed region, but only a small range of N was possible in the 50 cm tall tank. In Chapter 3 the dimensions of the experimental apparatus only allowed for aspect ratios $R_c/H_m \lesssim 1$. The numerical model showed that the intrusion speed approached the rectilinear wave speed for $R_c/H_m \gg 1$, but the consequences on internal wave generation are not well understood.

To improve our understanding of the effect of varying N and R_c/H_m on the generation of internal waves in the underlying fluid, we present a series of simulations with no rotation before examining the effects of non-zero f.

4.3.1 Effect of Lock Aspect Ratio on Non-rotating Intrusions

The ocean basins extend horizontally for thousands of kilometres, but the average depth is less than 5 km. This, and the influences of stratification and rotation result in geophysical oceanic phenomena typically having horizontal scales that are much larger than the vertical scales. In particular, for mixed regions resulting from tropical cyclones, $R_c \gg H_m$. But, in our laboratory experiments $0.3 < R_c/H_m < 1.2$. In this section, the effect of increasing lock aspect ratio on the generation of internal waves is explored using a series of simulations of non-rotating intrusions.

Figure 4.7 shows the simulated N_t^2 field for increasing values of the aspect ratio and a fixed buoyancy frequency of $N = 1.5\,\mathrm{s}^{-1}$ and $f = 0\,\mathrm{s}^{-1}$. Each image is a composite of the passive tracer field, displayed using a red colourmap

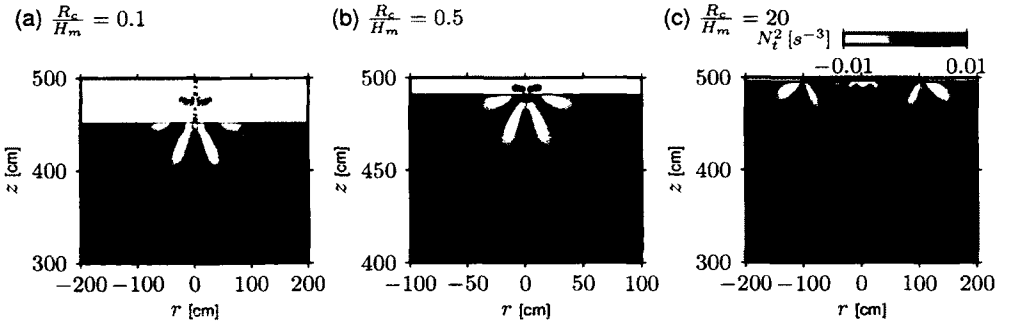

Figure 4.7: Composite images of the N_t^2 field for $z < H - H_m$ with blue colourmap indicated and the passive tracer field for $z \geq H - H_m$ in red extracted at $t = T_b$ for increasing values of the aspect ratio of the lock: (a) $R_c = 5\,\text{cm}$, $H_m = 50\,\text{cm}$, (b) $R_c = 5\,\text{cm}$, $H_m = 5\,\text{cm}$, (c) $R_c = 100\,\text{cm}$, $H_m = 5\,\text{cm}$ where $N = 1.5\,\text{s}^{-1}$, $f = 0\,\text{s}^{-1}$.

over the depth of the mixed region, and N_t^2 field below, displayed with a blue colourmap. The cross-section was extracted at $t = T_b$ to capture the generation of the waves immediately following the initial collapse.

When $R_c/H_m = 0.5$ the collapsing mixed region excited waves that propagated down and away from the mixed region. This is the differentiating case because the vertical scale of the collapse $H_m/2$ is equivalent to the radial length-scale. In other words, the half-depth of the patch is equal to the half-width.

When $R_c/H_m = 0.1$, after one buoyancy period internal waves propagated out from beneath the centre of the mixed region. Increasing the vertical extent of patch relative to its horizontal extent resulted in higher amplitude waves.

When $R_c/H_m = 20$ the effect of collapse upon wave generation was significantly different. Immediately after the release of the lock-fluid, internal waves formed just beneath the location where the edge of the cylindrical lock was located. Fanning out symmetrically about that point, waves propagated downward radially inward and outward. The fluid beneath the centre of the mixed region remained stationary until these waves (and the return flow into the lock) propagated to the centre of the tank. Having much lower relative H_m, the vertical extent of the collapse was much smaller than in the larger H_m cases, resulting in relatively low amplitude waves.

In Figure 4.8 the normalized characteristic frequency is plotted against the characteristic radial wavenumber for a series of simulations. A narrow range of frequencies were observed in the non-rotating experiments ((Holdsworth

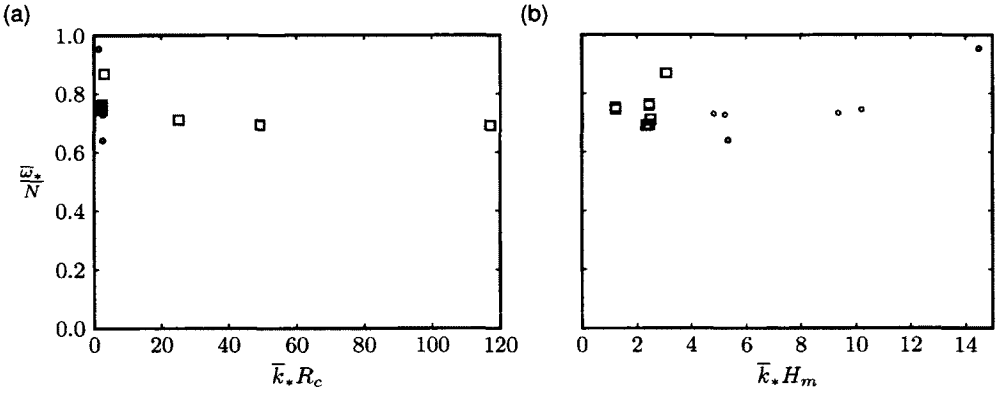

Figure 4.8: Normalized plots of wave frequency versus radial wavenumber for non-rotating simulations. In (a) $\overline{k}_*$ is normalized by R_c and in (b) $\overline{k}_*$ is normalized by H_m. The dots represent the simulations with $R_c/H_m \leq 1$ and the squares represent simulations with $R_c/H_m > 1$. The simulations shown in black have fixed $N = 1.5\,\mathrm{s}^{-1}$ with R_c/H_m between 0.1 to 50. The points shown in blue have fixed $R_c = 10\,\mathrm{cm}$, and N was varied such that for both $N = 0.75\,\mathrm{s}^{-1}$ and $N = 3\,\mathrm{s}^{-1}$, R_c/H_m ranged from 0.25 to 2 ($\Delta t = 0.5\,\mathrm{s}$, $\Delta z = 0.25\,\mathrm{cm}$, $\Delta r = 0.125\,\mathrm{cm}$).

et al., 2010) presented in Chapter 2). But, there we explored a relatively narrow range of buoyancy frequencies between $1.2\,\mathrm{s}^{-1}$ to $1.6\,\mathrm{s}^{-1}$. In addition to simulations with fixed $N = 1.5\,\mathrm{s}^{-1}$ (shown in black), the figure shows simulations in which $N = 0.75\,\mathrm{s}^{-1}$ and $N = 3\,\mathrm{s}^{-1}$ (shown in blue). The frequencies $\overline{\omega}_*$ ranged from $0.64N$ to $0.95N$ with an average value of $0.75N$.

Because R_c and the characteristic inverse radial wavenumber, $\overline{k}_*^{-1}$, are both radial length-scales, it is natural to expect R_c to set $\overline{k}_*$. However, the results of the spectral analysis shown in Figure 4.8 demonstrate that, for $R_c > H_m$ (displayed as squares), $\overline{k}_*$ scales more readily with H_m than it does with R_c; $\overline{k}_* H_m$ ranged from 1.2 to 3.1 and $\overline{k}_* R_c$ ranged from 1.5 to 117.

Figure 4.9 (a) shows that $\overline{k}_* R_c$ decreases to from 3 to 1.5 as the aspect ratio decreases from 1 to 0.1. The average value $\overline{k}_* R_c \simeq 2.3$ is in agreement with the non-rotating experiments presented in Chapter 2 where $\overline{k}_* R_c \simeq 2$. For large aspect ratios, an approximately linear fit to $\overline{k}_* R_c$ vs R_c/H_m is shown as a dashed line in Figure 4.9 (b) and is given by $\overline{k}_* H_m = [2.46 \pm 0.03]$. The dispersion relation in equation (4.2) explains how the radial wavelength is set by the vertical wavelength of the waves. If $f = 0\,\mathrm{s}^{-1}$, the radial wavenumber is given by $k_r = (k_z)[N^2/\omega^2 - 1]^{1/2}$. Because we find $\omega \simeq 0.75N$, then $k_r = 0.88k_z$, with k_z being set by H_m. This implies $k_z H_m \simeq 2.8$.

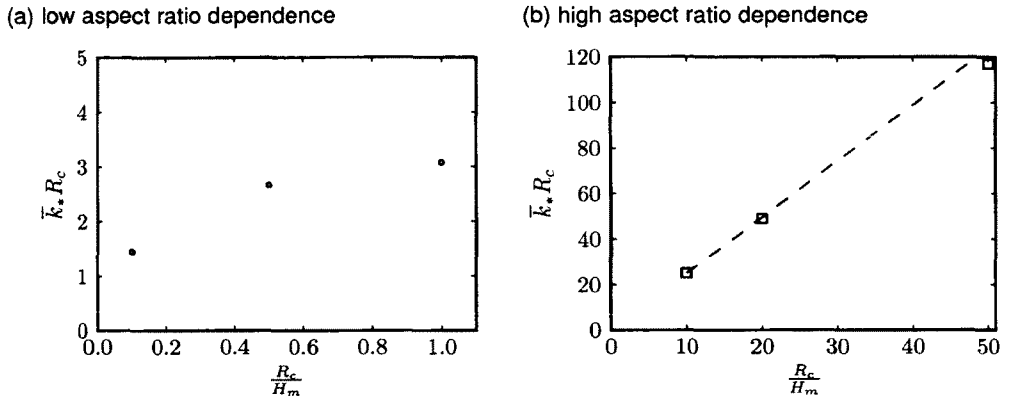

Figure 4.9: The dependence of the radial wavenumber on the height of the mixed region for non-rotating simulations with $N = 1.5\,\mathrm{s}^{-1}$. Simulations with (a) $R_c/H_m \leq 1$ and (b) $R_c/H_m > 1$ are shown separately. The best-fit line is shown for $R_c/H_m \geq 10\,\mathrm{cm}$ as a grey dashed line.

Figure 4.10 (b) shows that, for $R_c > H_m$, $|\bar{\xi}_*|$ increases only moderately with R_c. This is illustrated by the dotted line given by $|\bar{\xi}|_* = 0.001 R_c$. The slope is small enough that the amplitude is well approximated by $|\bar{\xi}_*| \simeq 0.12 H_m$ for $R_c/H_m > 1$.

When $R_c \gg H_m$, the influence of R_c becomes relatively unimportant. Internal waves are generated at the edge of the collapsing mixed region. And, H_m determines the characteristics of the vertically propagating waves.

Figure 4.11 shows the vertical displacement amplitude normalized by the radius of the cylinder and plotted as a function of R_c/H_m for increasing N and fixed $R_c = 10\,\mathrm{cm}$. Amplitudes, measured T_b after the release of the lock, increased with increasing H_m.

The flux of energy passing through $z = H - H_m - 10\,\mathrm{cm}$ was computed using equation (4.5) integrated from $T_1 = T_b$ to $T_2 = T_b + 2T_w$. This is shown in Figure 4.12 as a fraction of the available potential energy of the mixed patch given by equation (2.5). The maximum amount of energy was transported by the waves when the depth over which the collapse took place was equal to the radius of the patch (i.e. $R_c/H_m = 0.5$).

Relatively less energy was emitted for increasing and decreasing aspect ratios with as little as 0.04% released when $R_c/H_m = 50$. In part this is because waves are generated initially near $r = R_c$ so the available potential energy near the centre of the lock does not contribute to wave generation. These dynamics can be understood more clearly by examining the energy

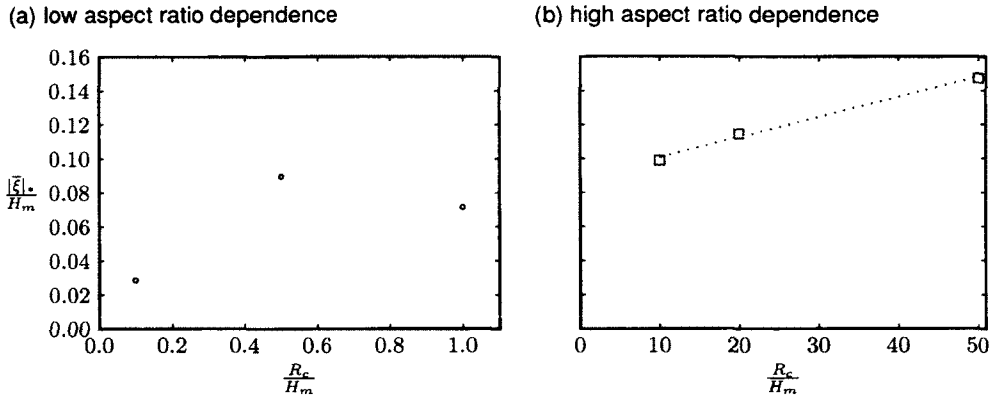

Figure 4.10: Maximum vertical displacement amplitudes plotted against the half-depth of the mixed region for the same simulations shown in Figure 4.9. Simulations with (a) $R_c/H_m \leq 1$ and (b) $R_c/H_m > 1$ are shown separately. The best-fit line is shown for $R_c/H_m \geq 10$ as a gray dotted line

equation given by equation (4.5). If $R_c/H_m \gg 1$, then H_m sets both $|\xi|$ and k_r. Because smaller H_m implies larger k_r relatively less energy is released. Conversely if $R_c/H_m < 1$, k_r increases as R_c decreases. So the energy extracted by the waves is significantly lower for smaller aspect ratios.

4.3.2 Effect of Rotation

In solid body rotation, the physical collapse of the mixed region was qualitatively different than in the non-rotating cases. From a top view, the mixed region was observed to propagate radially for a short distance before the patch contracted while rotating anti-cyclonically, and began laterally oscillating about its equilibrium radius. The side view revealed that the intrusion developed into a lens-shaped structure following curved isopycnal surfaces.

Rotation limited the outward propagation of the current so that for Ro $\ll 1$ very little deviation from solid body rotation was possible and there was no outward radial motion beyond R_c.

Figure 4.13 shows a composite image of the passive tracer field and the radial velocity field. The collapsing patch is shown as a black contour outlined by a thin white line. After only $t = 3T_b$, the difference between the rotating and non-rotating case is already apparent. In the non-rotating case (a) the intrusion thinned as it spread radially until it stopped due to interactions with internal waves (Holdsworth *et al.*, 2012*a*). In (b) rotation dominated and most of the lock-fluid amassed near the centre expanding and contracting as

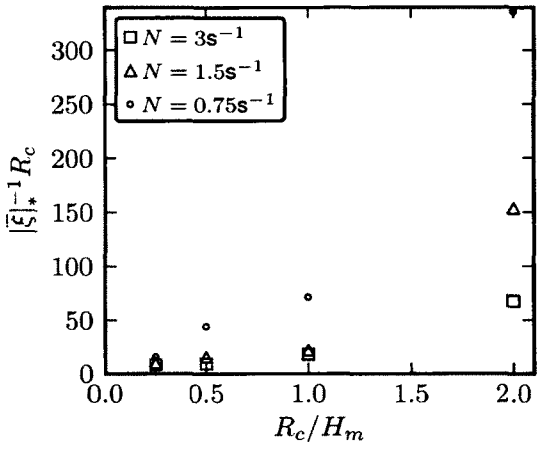

Figure 4.11: Vertical displacement as a function of R_c/H_m for N shown in the legend. Simulation parameters were $R_c = 10\,\text{cm}$ $f = 0\,\text{s}^{-1}$, $\Delta t = 0.5\,\text{s}$, $\Delta z = 0.25\,\text{cm}$, $\Delta r = 0.125\,\text{cm}$.

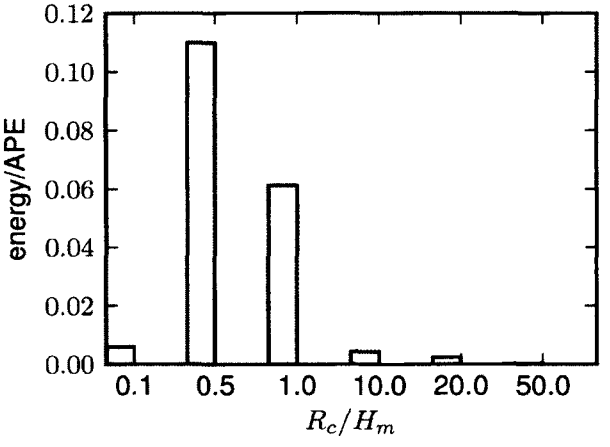

Figure 4.12: The energy flux at a height 5 cm beneath the mixed region given as a fraction of available potential energy transported away by downward propagating internal waves starting $1T_b$ after the lock was released and integrated over $2T_w$. These simulations have the same parameters as Figure 4.9

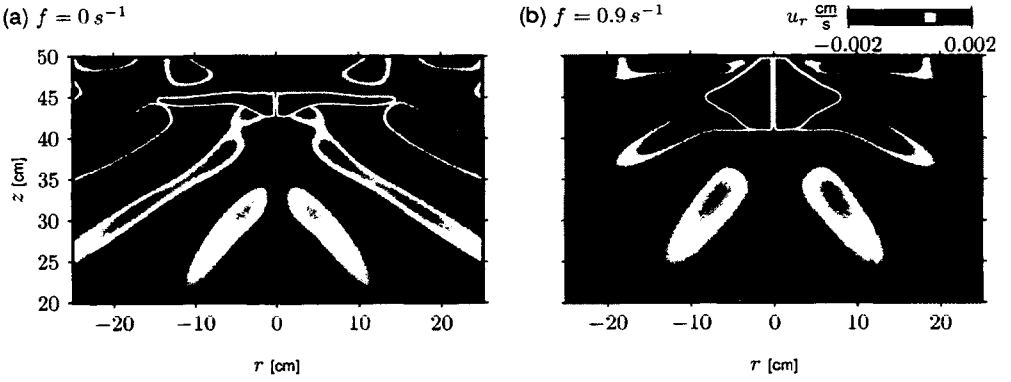

Figure 4.13: The shape of the intrusion at $t = 3T_b$ in (a) non-rotating frame and (b) rotating frame for the same initial conditions given by $N = 1.6\,\mathrm{s}^{-1}$, $H_m = 10\,\mathrm{cm}$, $R_c = 5\,\mathrm{cm}$, $\Delta t = 0.25\,\mathrm{s}$, $\Delta z = \Delta r = 0.098\,\mathrm{cm}$. The composite image shows the radial velocity field (colour contours) with the passive tracer field showing the shape of the intrusion as a black contour outlined by a thin white line.

it adjusted towards a geostrophically balanced state. This oscillatory motion had a resonant impact on the radial velocity of the ambient as it responded to the adjusting patch. Comparing the two velocity fields, it is evident that rotation restricted the radial transfer of energy.

Figure 4.14 (a) plots the wave frequency $\overline{\omega}_*$ normalized by the buoyancy frequency against the radial wavenumber $\overline{k}_*$ normalized by the radius of the cylinder. Characteristic values were measured between $2T_b$ and $2T_b + 2T_w$ and lie within a narrow range so that $0.67 \leq \overline{\omega}_*/N \leq 0.99$ and $2.7 \leq \overline{k}_* R_c \leq 5.2$.

But, compared with the non-rotating experiments (Holdsworth *et al.*, 2010) presented in Chapter 2, the rotating experiments exhibited a wider range of frequencies. This is most likely a direct result of the inertial oscillation of the lock-fluid which additionally excited internal waves at frequencies in the near-inertial range.

Vertical displacement amplitudes $|\overline{\xi}|_*$ were measured between $2T_b$ and $2.5T_b$ and are plotted in Figure 4.14 (b) against $H_m/2$. It is clear from the figure that the vertical displacement due to the waves increased with increasing H_m. But, given the variability in the data it is unclear whether $|\overline{\xi}|_*$ varies linearly with H_m .

Figure 4.15 shows the fraction of available potential energy input to the internal waves over $2T_w$. The fraction of available potential energy released varied from 0.5% to 13% with 3% released on average. To some extent, this

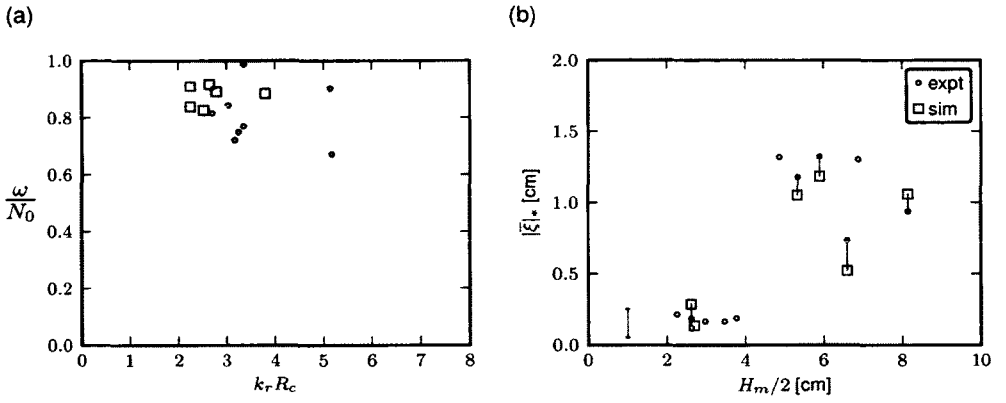

Figure 4.14: In (a) the characteristic frequency normalized by the buoyancy frequency is plotted against the characteristic radial wavenumber normalized by the height of the mixed region for the rotating experiments (circles) and corresponding simulations (squares). Error bars are indicated. For the same data (b) the maximum vertical displacement amplitudes are plotted against the half-depth of the mixed region. The associated simulations and experiments are connected by a grey line. A typical vertical errorbar is shown in the lower left corner. For the simulations $\Delta t = 0.00125\,\mathrm{s}$, $\Delta z = 0.09\,\mathrm{cm}$, $\Delta r = 0.047\,\mathrm{cm}$.

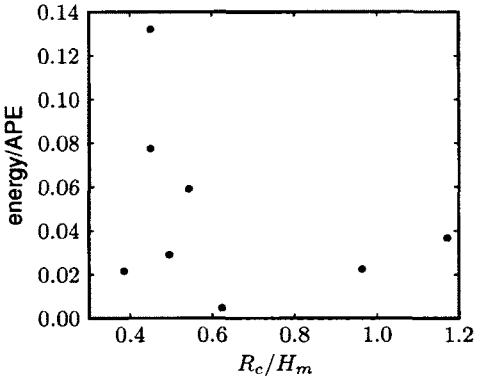

Figure 4.15: The energy flux through $z_0 = H - H_m - 5$ cm starting $1T_b$ after the lock was released and integrated over $2T_w$ for each of the rotating experiments.

plot agrees with the results presented in Figure 4.12 because the energy peaks for $R_c/H_m = 0.5$, but there is a substantial amount of variability in the data which may be a result of the rotation of the fluid.

Frequencies and radial wavenumbers measured from simulations initialized with the corresponding experimental parameters are plotted in Figure 4.14 (a). Like the experimental data, the non-dimensional frequencies and wavenumbers lie within a narrow range; $0.83 \leq \overline{\omega}_*/N \leq 0.92$ and $2.2 \leq \overline{k}_* R_c \leq 3.8$.

The amplitudes are plotted with the experimental data in Figure 4.14 (b). Each square denotes a simulated result which is connected with the experiment to which it corresponds by a grey line. Since the vertical distance over which the fluid collapsed was $H_m/2$, this depth was expected to set the initial vertical displacement amplitude of the internal waves. Initial vertical displacements $|\overline{\xi}|_*$ were measured approximately 5 cm below H_m. Figure 4.14 (b) shows that amplitudes increase with increasing H_m. But, since N varies, the exact relationship is not readily apparent from the data.

Considering the transient nature of the waves and the error associated with the experiments, the quantitative agreement between the numerical model and the experimental data is within the measurement error. This provides further evidence that the axisymmetric code reproduces the wave dynamics observed in the experiments.

In the following simulations we explore the influence of the Rossby number with fixed $R_c/H_m = 2$. The range of Rossby numbers that could be investigated for a given lock aspect ratio R_c/H_m was constrained by the fact that internal waves only exist for $f < \omega < N$ (equation (4.2)). The Rossby numbers range from $\mathrm{Ro} = 0.09$ to $\mathrm{Ro} = 1000$.

For simulations in the extreme case where $f \simeq N$ (i.e. $N = 1.5\,\mathrm{s}^{-1}$ and $f = 1.49\,\mathrm{s}^{-1}$), the patch expanded and contracted as the system returned to equilibrium. But, any undulations of the underlying fluid were damped. Consequently, no internal waves were released. For smaller values of f, internal waves were released immediately following the collapse of the mixed region, even for $\mathrm{Ro} \ll 1$ when the intrusion did not propagate an appreciable distance beyond one lock radii.

Figure 4.16 shows a snapshot of the N_t^2 field at $t \simeq 21T_b$ for (a) the non-rotating case and decreasing Rossby numbers (Figure 4.16 (b),(c),(d)). In the absence of rotation, the wavepacket excited during the initial collapse propagated to the edge of the domain and any further wave generation was of relatively low amplitude. Yet when $\mathrm{Ro} = 0.09$ (Figure 4.16 (d)) relatively high

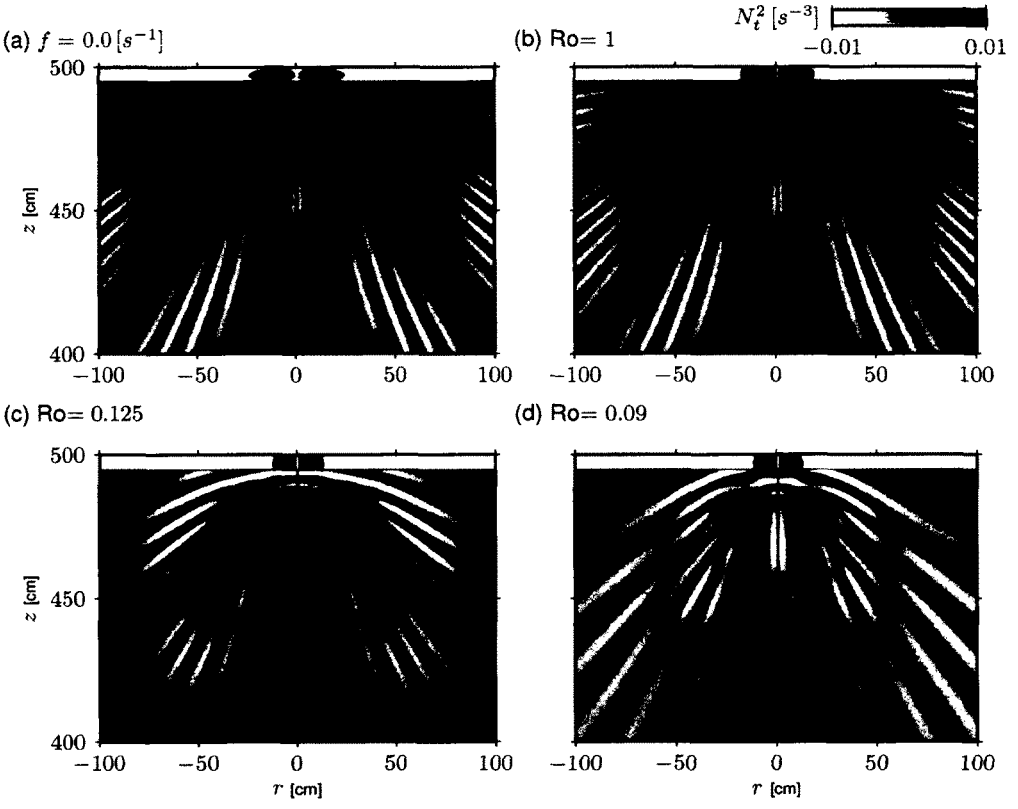

Figure 4.16: Composite images of the N_t^2 field for $z < H - H_m$ shown with a blue colourmap and the passive tracer field for $z \geq H - H_m$ shown in red at $t = 21T_b(90\,\mathrm{s})$ for (a) the non-rotating case and decreasing Rossby numbers ((b)–(d)). All of the figures have the same colorscale indicated in the upper right. The simulation parameters were $N = 1.5\,\mathrm{s}^{-1}$, $H_m = 5\,\mathrm{cm}$, $R_c = 10\,\mathrm{cm}$ and f was varied.

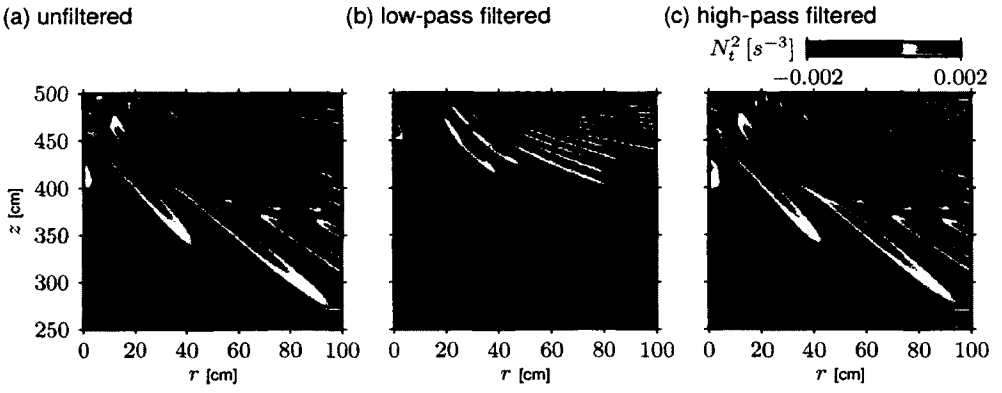

Figure 4.17: The N_t^2 field for a simulation with Ro = 0.125 and the same parameters as the experiment shown in Figure 4.16. At $t = 6T_b$ (a) the unfiltered field, (b) the low band-pass Fourier filtered field and (c) the high band-pass component are shown.

amplitude waves were still being excited. Rotation acts to confine the radial propagation of the internal waves to a conical region just below the lock-fluid and, the radius of the cone at a fixed vertical level just below the mixed region depends on L_D.

For all of the Rossby numbers examined here, the initial collapse released downward propagating internal waves. After about two buoyancy periods, although the exact time varied depending on the Rossby number, a second wavepacket was generated. This wavepacket was distinguished from the first because the angle made by phase lines to the vertical was noticeably larger than that of the wave generated initially.

We separated the signal into two wavepackets using a Fourier band-pass filter with a frequency cutoff of $\omega = f + 0.5(N - f)$. Even when $f = 0\,\mathrm{s}^{-1}$, the secondary wavepacket was generated and separated according to $\overline{\omega}_* \leq N/2$. An example of the wavepacket separation for Ro = 0.125 is shown in Figure 4.17. The same colorscale was used in all three images to demonstrate that the high band-pass component is of relatively large amplitude. Over time, both wavepackets move down and away from the mixed region, but the direction of propagation of the low-pass component is relatively horizontal.

Measured over the first three buoyancy periods, the characteristic frequencies $\overline{\omega}_*$ are represented by θ using equation (4.3) in Figure 4.18 (a). The dispersion relation given by equation (4.2) entails that $\omega = N$ at $\theta = 0$ and $\omega = f$ if $\theta = \pi/2$. The plot of $\sin\theta$ vs. $\cos\theta$ shows a separation between the

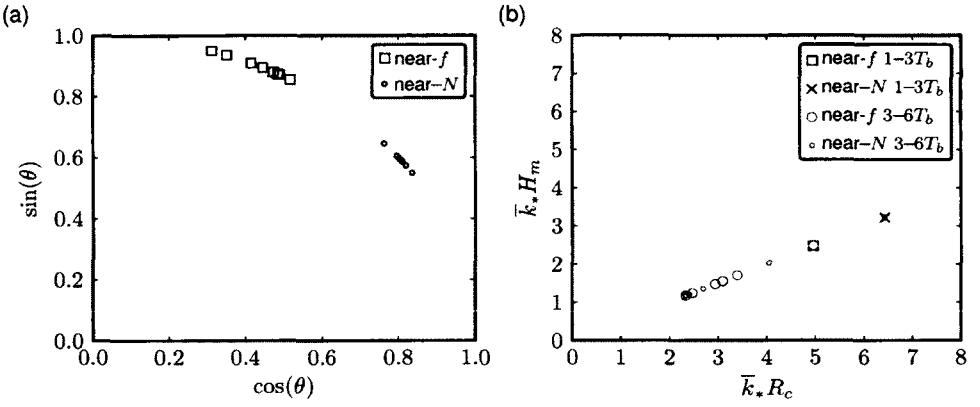

Figure 4.18: (a) Simulated early-time frequencies associated with the high and low band-pass wavepackets are given in terms of θ as defined by equation (4.3) and (b) the corresponding radial wavenumbers. Here, $N = 1.5\,\mathrm{s}^{-1}$, $H_m = 5\,\mathrm{cm}$, $R_c = 10\,\mathrm{cm}$.

characteristic frequency associated with each of the wavepackets. Equation (4.3) can be rearranged to make the relationship more intuitive as follows

$$\omega^2 = f^2 + N^2(1 - \sin^2\theta). \tag{4.10}$$

So $\theta \simeq \pi/2$ for frequencies near–f and waves propagate horizontally. And, for frequencies near–N, $\theta \gtrsim 0$ and waves propagate relatively vertically.

Figure 4.18 (b) shows that the radial wavenumber decreases in time for all Rossby numbers. Initially (between T_b and $3T_b$), the characteristic wavenumbers for the near–N wave and the near-inertial wave were $\overline{k}_* = 0.64\,\mathrm{cm}^{-1}$ and $\overline{k}_* = 0.49\,\mathrm{cm}^{-1}$, respectively, for all Rossby numbers. The plot shows that between $3T_b$ and $6T_b$ the wavenumber decreased for high and low frequency wavepackets.

Figure 4.19 shows that the near-N waves had small relative amplitude for small Rossby numbers, but this was nearly constant for larger Ro. The near–inertial wave amplitude peaked around Ro = 0.1.

Figure 4.20 shows the total fraction of available potential energy transported downward by the waves over time. The energy transport was computed by integrating the vertical energy flux over $21T_b$. For the near-inertial wave, we found that for large Ro nearly 100% of the total energy was transported over the first $6T_w$, while only about 65% of the total energy was transported in the low Ro cases. In the case of the near–N waves, between 65% and 80% of the total energy transport by the wavepacket occurred in the first $3T_w$

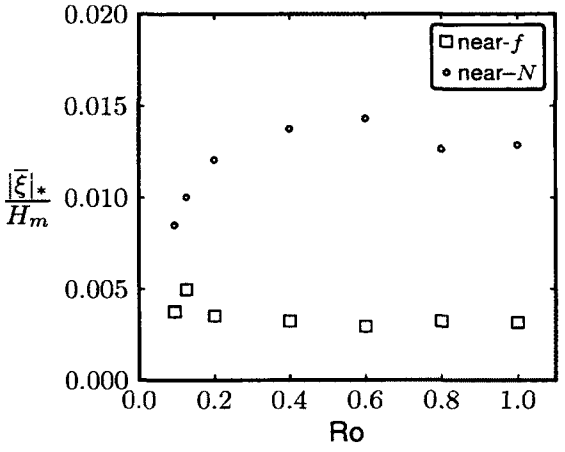

Figure 4.19: Normalized vertical displacement amplitudes determined from simulations are plotted as a function of the Rossby number measured after $t = T_b$. These are the same simulations plotted in Figure 4.18.

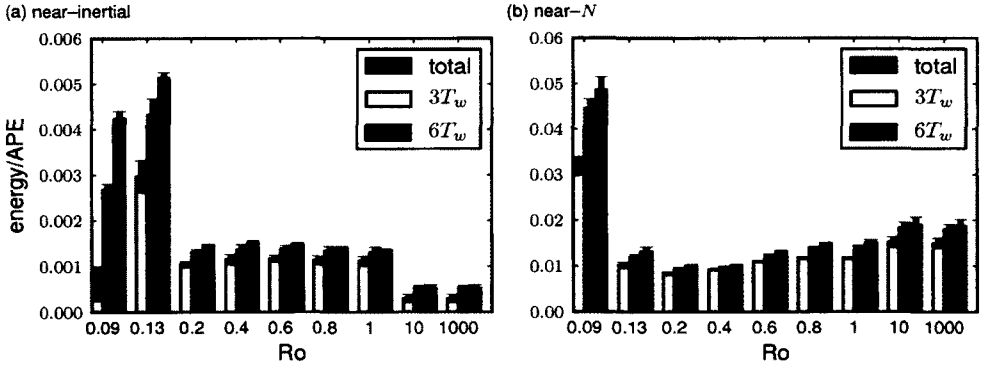

Figure 4.20: Bar graphs showing the total energy released after $t = 3T_w$, $6T_w$ and $21T_b$(90 s) for (a) the near-inertial waves and (b) the near–N waves. These are the same simulations plotted in Figure 4.18.

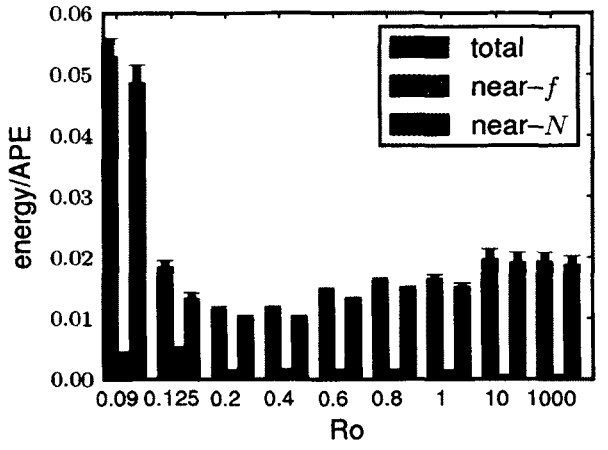

Figure 4.21: Distribution of energy between the near-inertial wavepacket and the near–N wave in the first $21T_b$. These values represent the sum of the energy associated with both wavepackets shown in Figure 4.20.

with over 90% transported after $6T_w$ for all Rossby numbers. Overall, wave generation was most substantial in the first $3T_w$ - $6T_w$. But, greater energy transports are possible in the case of low Rossby numbers because rotation sustains oscillations of the patch, thereby sustaining wave generation.

For the near–N wavepacket, the total fraction of available potential energy released was higher for smaller Ro where rotation enhanced the oscillations of the patch. However, the near-inertial waves transported the greatest amount of energy when Ro $\simeq$ 0.13. This is in contrast to the non-rotating experiments in which the columnar motions caused by the initial adjustment dissipated relatively quickly.

The analysis of both the amplitude and the energy indicates that the near–inertial component of the internal wave peaked for Ro $\simeq$ 0.13. This finding is supported by Stuart *et al.* (2011) who found that the most effective conversion of potential energy to kinetic energy occurred in this case. As they explained for this Rossby number ($R_c \simeq L_D$), the collapse most efficiently generated a single geostrophically balanced lens (Lelong & Sundermeyer, 2005).

A bar graph illustrating how the total energy transport over $21T_b$ was distributed amongst the wavepackets is shown in Figure 4.21. The near–N wavepacket transported more energy than the near–inertial wavepacket by an order-of-magnitude. While the maximal amount of energy transported by the near-inertial wave occurred around Ro = 0.1, the fraction of energy

transported by the near–N wave increased with increasing rotation.

These differences can be explained, in part, by appealing to our investigation of the aspect ratio of the lock. Without rotation, the mixed region underwent a gravitational adjustment and spread as it moved out radially, effectively increasing its aspect ratio R_c/H_m. But, rotation limited the radial propagation of the intrusion. So the lock-fluid maintained a relatively small aspect ratio ($R_c/H_m > 1$) as the patch continued to oscillate, thereby releasing more energy than in the large Rossby number cases.

Increasing the rate of rotation and so decreasing the Rossby number below $\mathrm{Ro} = 0.125$ shifted the entire frequency spectrum towards N and caused the waves to propagate nearly vertically.

That the near–N wave released more energy for low Rossby numbers despite a decrease in wave amplitude further supports the claim that the sustained undulations of the patch, which cause wave generation to continue over relatively long periods, is responsible for the observed increase in energy transport.

4.4 Discussion and Conclusions

Using a combination of laboratory experiments and numerical simulations we examined the collapse of a mixed region in uniformly stratified ambient as a mechanism for the generation of downward propagating internal waves. The experiments were performed in solid body rotation and compared with the related non-rotating study (Holdsworth *et al.*, 2010). They also allowed us to validate a numerical model which we used to extend the parameter range from those explored by the experiments.

The geometry of the lock played a significant role in determining the qualitative nature of the collapse. For large aspect ratios typical of ocean phenomena, we found that the height of the mixed region set the vertical displacement amplitude and radial wavenumber so that they are approximated by $|\overline{\xi}|_* \simeq 0.1 H_m$ and $\overline{k}_* = 2.46 \pm 0.03 H_m^{-1}$. When $\mathrm{Ro} < 1$, we found $\overline{k}_* R_c \simeq 2.3$. The greatest amount of energy was transported by the internal waves when $R_c = H_m/2$ and the vertical displacement of the waves was set by the combined influence of N and H_m.

Under the influence of rotation, the axisymmetric collapse of a mixed region in uniformly stratified fluid excited downward propagating internal waves for $f < N$, but the behaviour changed depending on the Rossby number. For

all Rossby numbers examined here, the collapse excited internal waves with two distinctive peaks in the frequency spectrum. The highest amplitude waves were generated with $\overline{\omega}_* \simeq 0.75N$ and a secondary peak occurred for ω near the inertial frequency. The lower the Rossby number, the closer f is to N which limits the range of frequencies for which internal waves can be generated. That the near–N component was enhanced with decreasing Rossby number, may be a result of this constraint.

The wavefield was separated into high-pass and low-pass components with a band-pass Fourier filter. The near-N wavepacket was found to transport substantially more energy downward and away from the mixed patch releasing an even larger fraction of energy for low Rossby numbers. For the near-inertial wave, the energy was most substantial when $\mathrm{Ro} \simeq 0.1$ which is not surprising since it is at this Rossby number that Coriolis and pressure gradient forces are close to balance.

For moderate to large Ro, wave generation was most substantial during the first (3–6) T_w. However, for low Ro, undulations of the fluid column beneath the lock-fluid were sustained. This caused wave generation to persist over longer time periods. So a larger fraction of the available potential energy of the patch was transported vertically by the waves.

These results can be extrapolated to ocean scales employing the same parameters used by Holdsworth *et al.* (2010). Hurricane Edouard (Emanuel, 2001) left a cold water wake with a temperature change of 3°C to a depth $H_m \simeq 50\,\mathrm{m}$. The along-track and cross-track lengths were 2000 km and 400 km, respectively. Buoyancy frequencies observed in the open ocean vary from about $0.0008\,\mathrm{s}^{-1}$(Pinkel & Anderson, 1997) to $0.009\,\mathrm{s}^{-1}$(Ladd & Thompson, 2000) so that the buoyancy period, T_b, ranges from 10 minutes to over 2 hours.

These parameters imply an aspect ratio of $R_c/H_m = 4000$ and very low Rossby numbers Ro between 2.82×10^{-3} and 2.5×10^{-5}. The computational cost of implementing a numerical simulation with such a large domain and rotation rate was too high for our direct numerical simulations, but we can make a crude prediction by extrapolating from the results we have.

For large aspect ratios, our results imply that internal wave frequencies would range from $6 \times 10^{-4}\,\mathrm{s}^{-1}$ to $7.2 \times 10^{-3}\,\mathrm{s}^{-1}$ and the amplitude would be $|\overline{\xi}|_* \simeq 5\,\mathrm{m}$. Hence, the radial wavelength of the internal waves would be $\lambda_r \simeq 1.3 \times 10^2\,\mathrm{m}$, set by the depth of the mixed patch.

In Figure 4.12, approximately 0.04% of the available potential energy was imparted to the internal waves when $R_c/H_m = 50$ and $f = 0\,\mathrm{s}^{-1}$ over $2T_b$. We

have shown that the energy transport was highest in the first few buoyancy periods so we assume that this value is about 80% of the total (over $\simeq 21T_b$), which gives 0.05%. Figure 4.21 shows that that 2% of the available potential energy was extracted when $R_c/H_m = 2$ for Ro = 1000, and about 5.2% was extracted when $R_c/H_m = 2$, for Ro = 0.09. Since the non-rotating case is virtually indistinguishable from the Ro = 1000 case when $R_c/H_m = 2$, we extrapolated from these results to find that the fraction of available potential energy transported away by downward propagating waves in the case when $R_c/H_m = 50$ and Ro = 0.09 was about 0.14%.

Liu *et al.* (2008) estimated that the passing hurricane increased the available potential energy of the mixed layer at a rate of 0.16 TW. So we suppose that 2×10^{17} J of available potential energy contributes to the collapse of the mixed region during the 18 day lifespan of the storm.

Assuming about 0.14% of the available potential energy of the patch is transported away by the downward propagating internal waves, we found that between 2 GW and 23 GW of power is input to the internal wavefield over $\simeq 21T_b$.

There are about 50 hurricanes per year (Emanuel, 2001). Averaging annually, we find that the power input from tropical cyclones to the internal wavefield from the collapse of the mixed region is on the order of 0.5 GW. This is an order-of-magnitude smaller than the estimate of Nilsson (1995) for the power transported away, horizontally, by near inertial waves propagating along the thermocline.

Since this approximation is based on the parameters associated with a mild tropical storm, this is thought to be an underestimate. More violent tropical storms have even smaller Rossby numbers and deeper mixed regions which means that they have the potential to transport more energy below the mixed region. In spite of this, this study has shown, in contrast to the extrapolation from the rotating results of Chapter 2, that the steady input of power to the internal wavefield from hurricanes through the collapse of the mixed region makes a relatively small contribution to diapycnal mixing in the ocean abyss when compared to the steady input of energy to the internal wavefield due to the forcing of the of the wind, 0.2 TW, tides, 1 TW or even from geothermal vents, 0.05 TW (Ferrari & Wunsch, 2010).

The axisymmetric model used here did not include the effects of turbulence, wind driven mixing and vorticity in the initial mixed patch, and it did not implement a realistic ocean stratification. Even so, the model provides an

order-of-magnitude estimate of the energy carried away by downward propagating internal waves resulting from the collapse of a mixed region in the ocean.

Chapter 5

Discussion and Conclusions

Prior to the work presented in this thesis, little was known about axisymmetric intrusions in stratified fluid and the internal waves they generate. We examined a series of experiments and simulations exploring the axisymmetric collapse of a mixed region in stratified and rotating fluid.

Previous work, described in Chapter 1 and summarized in Table 1.1, showed that symmetric intrusions in two-layer ambient propagated at near-constant speeds even as their head-heights decreased because a mode-2 interfacial wave, excited by the intrusion head, carried the intrusion forward (Sutherland & Nault, 2007; McMillan & Sutherland, 2010). The non-rotating experiments presented in Chapter 3 confirmed these results and, more importantly, they showed that in vertically asymmetric cases a mode-1 wave was excited by the return flow which caught up with the front of the intrusion, halting its advance.

For experiments performed with a uniformly stratified ambient the intrusion stopped abruptly without reaching the tank wall. As in the two-layer case, a symmetric collapse at mid-depth efficiently excited a mode-2 wave, while an asymmetric return flow from a collapse above or below mid-depth excited a mode-1 wave. However, since the intrusion moved more slowly than both mode-1 and mode-2 waves, its advance was halted by interactions with the waves.

The collapse of the partial-depth mixed patch on the ambient in uniformly stratified fluid generated internal waves that propagated downward and away from the patch. In a non-rotating fluid, the characteristic frequency of the conical wavepacket, was set by the buoyancy frequency ($\omega \simeq 0.75N$). However, the initial conditions which set the radial wavenumber and vertical displacement amplitude depended on the aspect ratio of the lock-fluid R_c/H_m.

For aspect ratios typical of ocean phenomena ($R_c \gg H_m$), H_m set the

radial wavenumber and the maximum vertical displacement due to the waves was set by the combined influence of N and H_m. Further study is needed to evaluate the relationship between the amplitude N and H_m.

The aspect ratio of the lock governed the qualitative nature of the collapse so that the largest fraction of the available potential energy was transported by the internal waves when $H_m/2 = R_c$. A relatively smaller fraction of energy was released for higher and lower aspect ratios.

Never before had the initial front speed of an axisymmetric intrusion propagating in stratified fluid been examined. In both two-layer and uniformly stratified ambient, intrusions emanating from locks of comparable depth and radius were found to be 30-35% slower than the predictions of rectilinear theory.

In the absence of rotation, the two most significant results of this thesis are that the speed and distance propagated by the intrusion is influenced by interactions with internal waves, and that the aspect ratio of the lock-fluid, R_c/H_m, can significantly impact the evolution of the collapse.

Rotation had no impact on the initial intrusion speed. However, for low Rossby numbers (Ro < 1), rotation limited the maximum distance propagated by the intrusion by deflecting the radial flow of the current azimuthally. The patch oscillated about its equilibrium radius as it approached a state of geostrophic balance. Hence, increasing the energy transportdue to vertically propagating internal waves.

In uniformly stratified fluid, the simulations presented in Chapter 4 demonstrated that the oscillatory motion of the adjusting patch sustained undulations of the underlying fluid. Through this mechanism, the conical region in which the waves propagated was limited by the rotation of the fluid; becoming smaller for lower Ro.

For all finite Rossby numbers, we found that the generated internal wavepacket could be separated into two distinct components: one had frequencies near-N and relatively higher amplitudes, the other had frequencies near-f. The fraction of available potential energy extracted by the near-f wave was greatest when Ro $\simeq 0.13$. Energy transport was most substantial in the first $3T_w$ to $6T_w$, the total duration of the adjustment was not determined here and warrants further study.

For the near-N wave, the fraction of energy transport was higher for lower Rossby numbers despite a decrease in the amplitude of the waves. Although the amplitudes were smaller than those measured for non-rotating cases, the

sustained motion of the patch caused a greater amount of energy to be released over the same time period.

In Chapters 2 and 4 we identified one of the pathways through which energy from the atmospheric wind field is transferred to the ocean internal wavefield (Figure 1.1). We extrapolated from our results to predict the annual power contribution to the internal wave field from the collapse of a mixed region left in the wake of a tropical cyclone. The power contribution was found to be small compared to the direct forcing of the wind and tides. Our idealized study neglected the influence of wind-driven circulations associated with the mixed patch, a realistic ocean stratification and turbulent mixing. These additional dynamics should be investigated before definitive conclusions are drawn about the energy transport due to the internal waves and the potential they have for mixing in the abyss.

Our results are more directly applicable to pervasive patches of localized turbulent mixing in the ocean interior that have aspect ratios between 10 and 1000 (Sundermeyer *et al.*, 2005). We have shown that these patches generate downward propagating waves that can transport energy to greater depth. The succession of wave breaking, creating a mixed patch and a mixed patch collapsing to excite waves constitutes a previously unexplored mechanism for energy to cascade from large to small scale.

Appendix A

Coordinates and Vector Identities

Polar Cylindrical Coordinates

$$\begin{aligned} x &= r\cos\theta & r &= \sqrt{x^2+y^2} \\ y &= r\sin\theta & \theta &= \tan^{-1}\left(\frac{y}{x}\right) \\ z &= z \end{aligned}$$

Gradient

For a scalar f

$$\nabla f = \left(\frac{\partial f}{\partial x}, \frac{\partial f}{\partial y}, \frac{\partial f}{\partial z}\right) = \left(\frac{\partial f}{\partial r}, \frac{1}{r}\frac{\partial f}{\partial \theta}, \frac{\partial f}{\partial z}\right).$$

For a vector $\mathbf{A}$

$$\nabla \cdot \mathbf{A} = \frac{\partial A_x}{\partial x} + \frac{\partial A_y}{\partial y} + \frac{\partial A_z}{\partial z} = \frac{1}{r}\frac{\partial r A_r}{\partial r} + \frac{1}{r}\frac{\partial A_\theta}{\partial \theta} + \frac{\partial A_z}{\partial z}.$$

Curl

$$\begin{aligned} \nabla \times \mathbf{A} &= \left[\left(\frac{\partial A_z}{\partial y} - \frac{\partial A_y}{\partial z}\right), \left(\frac{\partial A_x}{\partial z} - \frac{\partial A_z}{\partial x}\right), \left(\frac{\partial A_y}{\partial x} - \frac{\partial A_x}{\partial y}\right)\right] \\ &= \left[\left(\frac{1}{r}\frac{\partial A_z}{\partial \theta} - \frac{\partial A_\theta}{\partial z}\right), \left(\frac{\partial A_r}{\partial z} - \frac{\partial A_z}{\partial r}\right), \left(\frac{1}{r}\frac{\partial r A_\theta}{\partial r} - \frac{\partial A_r}{\partial \theta}\right)\right] \end{aligned}$$

Laplacian

$$\begin{aligned}\nabla^2 f = \Delta f &= \frac{\partial^2 f}{\partial x^2} + \frac{\partial^2 f}{\partial y^2} + \frac{\partial^2 f}{\partial z^2} \\ &= \frac{1}{r}\frac{\partial}{\partial r}\left(r\frac{\partial f}{\partial r}\right) + \frac{1}{r}\frac{\partial^2 f}{\partial \theta^2} + \frac{\partial^2 f}{\partial z^2}\end{aligned}$$

$$\begin{aligned}\nabla^2 \mathbf{A} &= [\Delta A_x, \Delta A_y, \Delta A_z] \\ &= \left[\Delta A_r - \frac{A_r}{r^2} - \frac{2}{r^2}\frac{\partial A_\theta}{\partial \theta}, \Delta A_\theta - \frac{A_\theta}{r^2} + \frac{2}{r^2}\frac{\partial A_r}{\partial \theta}, \Delta A_z\right]\end{aligned}$$

Appendix B

Axisymmetric Numerical Model

Governing Equations

The numerical model solves the Navier-Stokes equations for small-amplitude, axisymmetric waves in a Boussinesq, incompressible and inviscid fluid rotating with an angular acceleration of Ω. The equations are given in cylindrical coordinates by

$$\frac{\partial u}{\partial t} + u\frac{\partial u}{\partial r} + w\frac{\partial u}{\partial z} - \frac{v^2}{r} - fv = -\frac{1}{\rho_0}\frac{\partial p}{\partial r} + \nu\left[\nabla^2 u - \frac{u}{r^2}\right] \tag{B.1}$$

$$\frac{\partial v}{\partial t} + u\frac{\partial v}{\partial r} + w\frac{\partial v}{\partial z} + \frac{uv}{r} + fu = -\nu\left[\nabla^2 v + \frac{v}{r^2}\right] \tag{B.2}$$

$$\frac{\partial w}{\partial t} + u\frac{\partial w}{\partial r} + w\frac{\partial w}{\partial z} = \frac{1}{\rho_0}\left[\frac{\partial p}{\partial z} - \rho g\right] + \nu\nabla^2 w \tag{B.3}$$

$$\frac{\partial \rho}{\partial t} + u\frac{\partial \rho}{\partial r} + w\frac{\partial \rho}{\partial z} + w\frac{\partial \overline{\rho}}{\partial z} = \kappa\nabla^2\rho \tag{B.4}$$

$$\nabla\cdot\mathbf{u} = \frac{1}{r}\frac{\partial [ru]}{\partial r} + \frac{\partial w}{\partial z} = 0 \tag{B.5}$$

The code replaces the vertical and radial momentum by the equation for azimuthal vorticity, $\zeta = \partial_z u - \partial_r w$:

$$\frac{\partial \zeta}{\partial t} = -ur\frac{\partial \zeta/r}{\partial r} - w\frac{\partial \zeta}{\partial z} - \nu\left[\nabla^2\zeta - \frac{\zeta}{r^2}\right] + \frac{1}{r}\frac{\partial [v^2 + fvr]}{\partial z}. \tag{B.6}$$

From the continuity equation for an incompressible fluid, one can define the streamfunction ψ so that $\mathbf{u} = \nabla\times(\psi\hat{\theta})$. Explicitly, the components of velocity are given by

$$u = -\frac{\partial \psi}{\partial z} \tag{B.7}$$

$$w = \frac{1}{r}\frac{\partial (r\psi)}{\partial r}. \tag{B.8}$$

Model Parameters

u	radial velocity
v	azimuthal velocity
w	vertical velocity
$f = 2\Omega$	the Coriolis parameter
p	pressure
ρ	fluctuation density
ρ_0	reference density
$\overline{\rho}$	background density
g	gravitational acceleration
κ	diffusivity
ν	kinematic viscosity

Thus, the streamfunction is related implicitly to the azimuthal vorticity by

$$\nabla^2\psi - \frac{\psi}{r^2} = -\zeta. \tag{B.9}$$

The stremfunction and the vorticity are represented by a combination of the first order Bessel function in r and a sine function in z so that for field f ($= \psi$ or ζ) at a time t

$$f(r,z) = \sum_{i=0}^{I}\sum_{j=0}^{J} A_f(k_i,m_j)J_1(k_i r)\sin(mz). \tag{B.10}$$

The streamfunction is determined spectrally from the azimuthal vorticity by transforming ζ to Fourier-Bessel space. The Laplacian given by equation (B.9) in this space is inverted and the resulting field is transformed back to real-space. Velocities are computed directly using equations (B.7) and (B.8).

The spatial derivatives in equations (B.2), (B.4), (B.6) are approximated using second order finite differencing. They are stepped forward in time using the leap-frog scheme which is initialized using second order forward differencing. To prevent the growth of numerical error an Euler-backstep is implemented every 20 time steps in which the fields from the previous time steps are averaged. The free-slip boundaries satisfy $\mathbf{u}\cdot\mathbf{n} = 0$.

To visualize the movement of the fluid intrusion a passive tracer field was advected along with the other fields.

Model Implementation and Validation

Before simulating the experiments with the numerical model we first performed a series of simple tests for which the solution could be determined analytically.

Having done this we then validated the model with our experimental data. Using the same initial conditions from the laboratory experiments we initialized several high resolution runs ($\Delta t = 0.125\,\mathrm{s}$, $\Delta z = 0.09\,\mathrm{cm}$, $\Delta r = 0.05\,\mathrm{cm}$). Qualitatively, the model was able to capture the collapse and evolution of the intrusion.

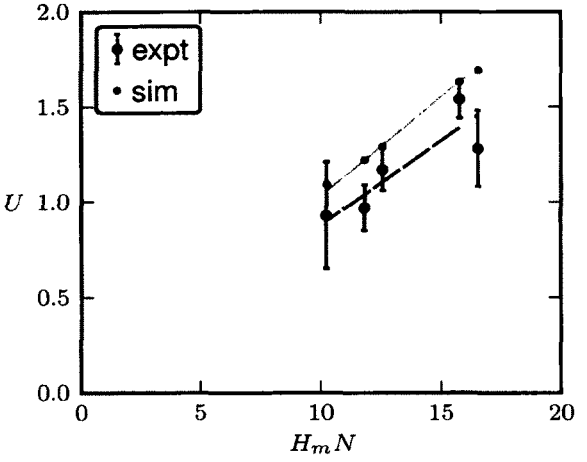

Figure B.1: Comparison of experimentally determined speeds with numerical simulations.

For a series of simulations the initial near-constant speed was calculated and compared with the experimental data. Figure B.1 shows that the simulations produce currents that have higher speeds than those observed from the experiments. While the discrepancy is small relative to the experimental error, the fact that the simulated speeds are consistently higher than those measured in the experiments indicates that there is a systematic error. The most likely explanation is that a $2D$ model cannot capture all of the dynamics present in the laboratory experiments. For example, the intrusion may be losing some energy to the generation of turbulence. Thus, the model captures the trends in the data, but overpredicts the speed.

In Chapter 4 we showed that the model simulated the generation of internal waves qualitatively. Figure 4.14 demonstrated that the quantitative features of these waves were well represented by the numerical simulations.

To extend spacial domain of the model we referred to the Courant-Friedrichs-Lewy (CFL) equation. The condition requires that the time step is kept small enough so that information has time to propagate through the spacial steps

and is given by

$$C_r = U\frac{\Delta t}{\Delta r} \tag{B.11}$$

Although there is a $2D$ representation of the CFL condition, usually it is enough to consider each spacial resolution separately as shown in equation B.11. In the simulations presented in this thesis the largest vertical motions occurred within the first few seconds. If the model did not become unstable immediately then the radial CFL condition was the determining factor. Typical values for stable configurations ranged from $20 \leq C_r \leq 70$. Similarly $C_z = U\frac{\Delta t}{\Delta z}$ ranged from $20 \leq C_z \leq 60$.

Appendix C

Wavelet Transforms

The wavelet transform of a signal $s(t)$ is given by

$$\tilde{s}(a,b) = \int_{-\infty}^{+\infty} s(t)\,\overline{\Upsilon}_{a,b}\,(t)\,dt \tag{C.1}$$

where

$$\overline{\Upsilon}_{a,b}(t) = \frac{1}{\sqrt{a}}\,\overline{\Upsilon}\left(\frac{t-b}{a}\right) \tag{C.2}$$

and $\overline{\Upsilon}(t)$ is the complex conjugate of the "mother wavelet" $\Upsilon(t)$. For scale a at time b the wavelet bases are dilations and translations of the mother wavelet. Wavelet coefficients $\tilde{s}(a,b)$ are determined using wavelet basis functions.

The choice of mother wavelet was guided both by the structure of the internal wave signal and by the application. Real-valued wavelets, such as the family of Gaussian derivatives, return only a single component making them well suited to isolating peaks in the power spectrum. The Gaussian family consists of the Gaussian function and its derivatives (DOG wavelets). As the number of the Gaussian derivatives increase the number of wavelet oscillations increases as well. Since the signal contains a small number of oscillations, we choose to use a lower order Gaussian wavelet. Gaussian wavelets of increasing order were tested and it was found that the DOG 3 wavelets determined the radial wavenumber most accurately.

The wavelet power spectrum, also known as the scalogram, is defined by

$$P(a,b) = |\tilde{s}(a,b)|^2\,. \tag{C.3}$$

To find the wavelet power spectrum we adapted the on-line wavelet toolbox provided by Torrence & Compo (1998) who provide a detailed description of

this process. The open-source toolbox is freely available and is well-tested (Linkenkaer-Hansen *et al.*, 2001; Moy *et al.*, 2002; Holdsworth *et al.*, 2012*b*).

The wavelet scale can be related analytically to what is typically referred to as the Fourier Period to determine Fourier modes. But, in this case, the transform is being applied to a length-scale and not a time-scale so we instead refer to it as the "Fourier scale".

Bibliography

AMEN, R. & MAXWORTHY, T. 1980 The gravitational collapse of a mixed region into a linearly stratified solution. *J. Fluid Mech.* **96**, 65–80.

ANSONG, J. & SUTHERLAND, B. R. 2009 Internal gravity waves generated by convective plumes. *J. Fluid Mech.* p. in press.

BENJAMIN, T. B. 1968 Gravity currents and related phenomena. *J. Fluid Mech.* **31**, 209–248.

BOLSTER, D., HANG, A. & LINDEN, P. F. 2008 The front speed of intrusions into a continuously stratified medium. *J. Fluid Mech.* **594**, 369–377.

BOOS, W. R., SCOTT, J. R. & EMANUEL, K. A. 2003 Transient diapycnal mixing and the meridional overturning circulation. *J. Phys. Oceanogr.* **34**, 334–341.

BRITTER, R. E. & SIMPSON, J. E. 1981 A note on the structure of the head of an intrusive gravity current. *J. Fluid Mech.* **112**, 459–466.

CHEONG, H., KUENEN, J. J. P. & LINDEN, P. F. 2006 The front speed of intrusive gravity currents. *J. Fluid Mech.* **552**, 1–11.

D'ASARO, E., BLACK, P., CENTURIONI, L., HARR, P., JAYNE, S., LIN, I. I., LEE, C., MORZEL, J., MRVALJEVIC, R., NIILER, P. P., RAINVILLE, L., SANFORD, T. & TANG, T. Y. 2011 Typhoon-Ocean Interaction in the Western North Pacific: Part 1. *Oceanography* **24** (4, SI), 24–31.

DOHAN, K. & SUTHERLAND, B. R. 2003 Internal waves generated from a turbulent mixed region. *Phys. Fluids* **15**, 488–498.

EMANUEL, K. 2001 Contribution of tropical cyclones to meridional heat transport by the oceans. *J. Geophys. Res.* **106**, 14,771–14,781.

FERRARI, R. & WUNSCH, C. 2009 Ocean Circulation Kinetic Energy: Reservoirs, Sources, and Sinks. *Annual Review of Fluid Mechanics* **41**, 253–282.

FERRARI, R. & WUNSCH, C. 2010 The distribution of eddy kinetic and potential energies in the global ocean. *Tellus Series A-dynamic Meteorology and Oceanography* **62** (2), 92–108.

FLYNN, M. R. & LINDEN, P. F. 2006 Intrusive gravity currents. *J. Fluid Mech.* **568**, 193–202.

FLYNN, M. R., ONU, K. & SUTHERLAND, B. R. 2003 Internal wave generation by a vertically oscillating sphere. *J. Fluid Mech.* **494**, 65–93.

FLYNN, M. R. & SUTHERLAND, B. R. 2004 Intrusive gravity currents and internal wave generation in stratified fluid. *J. Fluid Mech.* **514**, 355–383.

GRANT, H. L., MOILLIET, A. & VOGEL, W. M. 1968 Some Observations of Occurrence of Turbulence in and Above the Thermocline. *Journal of Fluid Mechanics* **34** (Part 3), 443–&.

GREGG, M. C. 1976 Finestructure and microstructure observations during the passage of a mild storm. *J. Phys. Oceanogr.* **6**, 528–555.

HALLWORTH, M. A., HUPPERT, H. E. & UNGARISH, M. 2001 Axisymmetric gravity currents in a rotating system: Experimental and numerical investigations. *J. Fluid Mech.* **447**, 1–29.

HOLDSWORTH, A. M., BARRETT, K. J. & SUTHERLAND, B. R. 2012*a* Axisymmetric intrusions in two-layer and uniformly stratified environments with and without rotation. *Phys. Fluids* **24**, 036603.

HOLDSWORTH, A. M., DECAMP, S. & SUTHERLAND, B. R. 2010 The axisymmetric collapse of a mixed patch and internal wave generation in uniformly stratified fluid. *Phys. Fluids* **22**, 106602.

HOLDSWORTH, A. M., KEVLAHAN, N. K.-R. & EARN, D. J. D. 2012*b* Multifractal signatures of infectious diseases. *Journal of The Royal Society Interface* **9** (74), 2167–2180.

HOLDSWORTH, A. M. & SUTHERLAND, B. R. (in preparation for submission to Phys. Fluids) The axisymmetric collapse of a mixed patch and internal wave generation in uniformly stratified fluid under the influence of rotation

.

HOLYER, J. Y. & HUPPERT, H. E. 1980 Gravity currents entering a two-layer fluid. *J. Fluid. Mech.* **100**, 739–767.

HUPPERT, H. E. & SIMPSON, J. E. 1980 The slumping of gravity currents. *J. Fluid Mech.* **99**, 785–799.

KEULEGAN, G. H. 1957 An experimental study of the motion of saline water from locks into fresh water channels. *Tech. Rep.* 5168. Nat. Bur. Stand. Rept.

LADD, C. & THOMPSON, L. A. 2000 Formation mechanisms for north pacific central and eastern subtropical mode waters. *J. Phys. Oceanogr.* **30**, 868–1.

LELONG, M.-P. & SUNDERMEYER, M. A. 2005 Geostrophic adjustment of an isolated diapycnal mixing event and its implications for small scale lateral dispersion. *Journal of Physical Oceanography* **35**, 2352.

LIN, I., LIU, W. T., WU, C.-C., WONG, G. T. F., HU, C., CHEN, Z., LIANG, W.-D., YANG, Y. & LIU, K.-K. 2003 New evidence for enhanced ocean primary production triggered by tropical cyclone. *Geophys. Rec. Lett.* **30** (13).

LINKENKAER-HANSEN, K., NIKOULINE, V., PALVA, J. & ILMONIEMI, R. 2001 Long-range temporal correlations and scaling behavior in human brain oscillations. *Journal of Neuroscience* **21** (4), 1370–1377.

LIU, L. L., WANG, W. & HUANG, R. X. 2008 The Mechanical Energy Input to the Ocean Induced by Tropical Cyclones. *Journal of Physical Oceanography* **38**, 1253–+.

LOWE, R. J., LINDEN, P. F. & ROTTMAN, J. W. 2002 A laboratory study of the velocity structure in an intrusive gravity current. *J. Fluid Mech.* **456**, 33–48.

MADERICH, V. S., VAN HEIJST, G. J. F. & BRANDT, A. 2001 Laboratory experiments on intrusive flows and internal waves in a pycnocline. *J. Fluid Mech.* **432**, 285–311.

MANINS, P. 1976 Intrusion into a stratified fluid. *J. Fluid Mech.* **74**, 547–560.

MAXWORTHY, T., LEILICH, J., SIMPSON, J. & MEIBURG, E. H. 2002 The propagation of a gravity current in a linearly stratified fluid. *J. Fluid Mech.* **453**, 371–394.

MAXWORTHY, T. & MONISMITH, S. 1988 Differential mixing in a stratified fluid. *J. Fluid Mech.* **189**, 571.

MCMILLAN, J. M. & SUTHERLAND, B. R. 2010 The lifecyle of axisymmetric internal solitary waves. *Nonlin. Proc. Geophys.* **17**, 443–453.

MOY, C. M., SELTZER, G. O., RODBELL, D. T. & ANDERSON, D. M. 2002 Variability of el nio/southern oscillation activity at millennial timescales during the holocene epoch. *Nature* **420** (6912), 162.

MUNK, W. H. & WUNSCH, C. 1998 Abyssal recipes II: Energetics of tidal and wind mixing. *Deep-Sea Res.* **45**, 1977–2010.

MUNROE, J. R., VOEGELI, C., SUTHERLAND, B. R., BIRMAN, V. & MEIBURG, E. H. 2009 Intrusive gravity currents from finite-length locks in a uniformly stratified fluid. *J. Fluid Mech.* **635**, 245–273.

NILSSON, J. 1995 Energy Flux from Traveling Hurricanes to the Oceanic Internal Wave Field. *Journal of Physical Oceanography* **25**, 558–573.

OAKEY, N. & GREENAN, B. 2004 Mixing in a coastal environment: 2. A view from microstructure measurements. *Journal of Geophysical Research-Oceans* **109** (C10).

OSTER, G. 1965 Density gradients. *Sci. Am.* **213**, 70.

PINKEL, R. & ANDERSON, S. 1997 Shear, strain, and Richardson number variations in the thermocline. Part I: Statistical description. *J. Phys. Oceanogr.* **27**, 264–281.

PRICE, J. F. 1981 Upper ocean response to a hurricane. *J. Phys. Oceanogr.* **1**, 153–175.

ROTTMAN, J. W. & SIMPSON, J. E. 1983 Gravity currents produced by instantaneous releases of a heavy fluid in a rectangular channel. *J. Fluid Mech.* **135**, 95–110.

SANDSTRÖM, J. 1908 Dynamische versuche mit meerwasser. *Ann. Hydrodynam. Marine Meteorol* **36**, 6–23.

SANDSTRÖM, J. 1916 Meteorologische studien schwedischen hochgebirge .

SCHMIDT, W. 1911 Zur mechanik der böen. *Z Meteorol* **28** (35), 62.

SILVA, I. P. D. D. & FERNANDO, H. J. S. 1998 Experiments on collapsing turbulent regions in stratified fluids. *J. Fluid Mech.* **358**, 29–60.

SIMPSON, J. E. 1972 Effects of lower boundary on the head of a gravity current. *J. Fluid Mech.* **53**, 759–768.

SIMPSON, J. E. & BRITTER, R. E. 1979 The dynamics of the head of a gravity current advancing over a horizontal surface. *J. Fluid Mech.* **94**, 477–495.

SRIVER, R. L. & HUBER, M. 2007 Observational evidence for an ocean heat pump induced by tropical cyclones. *Nature* **447**, 577–580.

STUART, G., SUNDERMEYER, M. & HEBERT, D. 2011 On the geostrophic adjustment of an isolated lens: Dependence on burger number and initial geometry*. *Journal of Physical Oceanography* **41** (4), 725–741.

SUNDERMEYER, M., LEDWELL, J., OAKEY, N. & GREENAN, B. 2005 Stirring by small-scale vortices caused by patchy mixing. *Journal of physical oceanography* **35** (7), 1245–1262.

SUTHERLAND, B. R. 2002 Interfacial gravity currents. I. Mixing and entrainment. *Phys. Fluids* **14**, 2244–2254.

SUTHERLAND, B. R., CHOW, A. N. F. & PITTMAN, T. P. 2007 The collapse of a mixed patch in stratified fluid. *Phys. Fluids* **19**, 116602–1–6, doi:10.1063/1.2814331.

SUTHERLAND, B. R., DALZIEL, S. B., HUGHES, G. O. & LINDEN, P. F. 1999 Visualisation and measurement of internal waves by "synthetic schlieren". Part 1: Vertically oscillating cylinder. *J. Fluid Mech.* **390**, 93–126.

SUTHERLAND, B. R., FLYNN, M. R. & DOHAN, K. 2004*a* Internal wave excitation from a collapsing mixed region. *Deep-Sea Res. II* **51**, 2889–2904.

SUTHERLAND, B. R., KYBA, P. J. & FLYNN, M. R. 2004*b* Interfacial gravity currents in two-layer fluids. *J. Fluid Mech.* **514**, 327–353.

SUTHERLAND, B. R. & NAULT, J. T. 2007 Intrusive gravity currents propagating along thin and thick interfaces. *J. Fluid Mech.* **586**, 109–118, doi:10.1017/S0022112007007288.

TAN, A. W., NOBES, D. S., FLECK, B. A. & FLYNN, M. R. 2011 Gravity currents in two-layer stratified media. *Environmental Fluid Mechanics* **11** (2), 203–223.

TORRENCE, C. & COMPO, G. 1998 A practical guide to wavelet analysis. *Bulletin of the American Meteorological Society* **79** (1), 61–78.

UNGARISH, M. 2006 On gravity currents in a linearly stratified ambient: A generalization of Benjamin's steady-state propagation results. *J. Fluid Mech.* **548**, 49–68.

UNGARISH, M. 2009 *An Introduction to Gravity Currents and Intrusions*. Chapman and Hall/CRC press, Boca Raton London New York.

UNGARISH, M. & HUPPERT, H. E. 1998 The effects of rotation on axisymmetric gravity currents. *J. Fluid Mech.* **362**, 17–51.

UNGARISH, M. & HUPPERT, H. E. 2004 On gravity currents propagating at the base of a stratified ambient: Effects of geometrical constraints and rotation. *J. Fluid Mech.* **521**, 69–104.

UNGARISH, M. & ZEMACH, T. 2003 On axisymmetric rotating gravity currents: Two-layer shallow-water and numerical solutions. *J. Fluid Mech.* **481**, 37–66.

WOODS, J. D. & WILEY, R. L. 1972 Billow Turbulence and Ocean Microstructure. *Deep-sea Research* **19** (2), 87–&.

WU, J. 1969 Mixed region collapse with internal wave generation in a density stratified medium. *J. Fluid Mech.* **35**, 531–544.

WUNSCH, C. & FERRARI, R. 2004 Vertical mixing, energy, and the general circulation of the oceans. *Annu. Rev. Fluid Mech.* **36**, 281–314.